

The Pennsylvania State University

The Graduate School

Department of Engineering Science and Mechanics

**MECHANICAL RESPONSE OF OUT-OF-AUTOCLAVE COMPLEX FIBER  
ARCHITECTURE COMPOSITES FOR MARINE STRUCTURES**

A Thesis in

Engineering Science and Mechanics

by

Rudy Haluza

Submitted in Partial Fulfillment  
of the Requirements  
for the Degree of

Master of Science

August 2017

The thesis of Rudy Haluza was reviewed and approved\* by the following:

Kevin L. Koudela  
Research Associate, Head of ARL Composites Materials Division  
Thesis Advisor

Charles E. Bakis  
Distinguished Professor of Engineering Science & Mechanics  
Thesis Co-Advisor

Clifford J. Lissenden  
Professor of Engineering Science & Mechanics

Judith A. Todd  
Department Head and P.B. Breneman Chair of Engineering Science & Mechanics  
Professor of Engineering Science & Mechanics

\*Signatures are on file in the Graduate School

## ABSTRACT

Hydrokinetic turbines have shown promise as a novel method for harvesting power from natural waterways. The customizability of these turbines allows for smaller turbine systems compared to large, geographically demanding hydroelectric plants. However, maintenance costs stemming from relatively short service lives of existing glass/epoxy turbine blades impede the growth of hydrokinetic power. In prototype blades, fatigue loading in salt water caused relatively rapid degradation and subsequent high maintenance costs. Thus, fatigue-resistant blades designed for multi-decade service life would lower the net cost of hydrokinetic turbine usage and increase the feasibility, and therefore growth, of hydrokinetic turbine usage. Furthermore, material systems chosen for hydrokinetic blade use must be studied in order to understand their behavior in long-term under-sea conditions.

This study researched the tensile-mechanical response of a quasi-isotropic woven and stitched laminate under quasi-static and fatigue loading at a stress ratio ( $R$ ) of 0.1 and a frequency of 10 Hz. Some fatigue samples were fatigued until failure, while others underwent residual modulus and strength measurements. Both woven and stitched laminates were found to survive ten million cycles with a maximum stress of +13.75 ksi, but fail prior to ten-million cycles with a maximum stress of +18 ksi. In room-temperature ambient conditions, the polyester-stitched composite proved to have superior fatigue life only in long-life ( $>10^5$  cycles) fatigue tests. Damaged, but not failed samples showed similar trends in that stitched samples would have more damage at lower cycle counts, but less damage at higher cycle counts compared to woven samples. However, there was more statistical scatter within the stitched specimens compared to woven specimens. Samples that were conditioned and tested while submerged in water had 30% reduction in tensile strength compared to the non-conditioned samples tested in ambient

conditions. The partially saturated samples also showed damage accumulation and failure occurring nearly a decade earlier than the non-conditioned samples.

Through optical macroscopic and microscopic investigation, intralaminar cracks and delaminations were found to occur in damaged woven samples, while stitched samples showed higher densities of unconnected intralaminar cracks before failure. Delaminations were found in near-failure stitch-bonded samples, especially in those tested at higher maximum fatigue stresses. More intralaminar cracks were found within stitched specimens compared to woven specimens that had similar reductions in elastic modulus, although, stitched specimens showed greater strength retention compared to the woven specimens. Future research could utilize these macroscopic and microscopic crack densities to develop models to better predict turbine blade damage at given loading levels and cycles.

## TABLE OF CONTENTS

List of Figures .....	vi
List of Tables .....	viii
Acknowledgements .....	ix
Chapter 1 Literature I: Hydrokinetic Turbine Technologies and Analysis .....	1
Hydrokinetic Energy and Background .....	1
Structural Hydrokinetic Blade Design .....	4
Manufacturing Methods .....	5
Previous Methods of Analysis .....	6
Chapter 2 Literature II: Effects of Marine Environments on Polymer Composite Structures .....	9
Brief Introduction of Polymer Matrix Composites .....	9
Water Absorption and Elevated Temperature Conditioning Effects .....	12
Wet & Elevated Temperature (WET) Conditioning Degradation Mechanisms .....	14
Chapter 3 Literature III: Textile Composite Damage Mechanics .....	24
Overview of Textile Composites .....	24
Review of Tape Laminate Composite Fatigue Damage & Failure .....	26
Overview of Textile Composite Damage & Failure .....	27
Quasi-Static Tension .....	28
Quasi-Static Compression .....	30
Tension-Tension Fatigue .....	32
Compression-Compression Fatigue .....	33
Thermoplastic Stitches .....	34
Chapter 4 Research Opportunities and Objectives .....	37
Research Opportunity .....	37
Research Objectives and Tasks .....	38
Chapter 5 Experimental Procedures .....	40
Specimen Manufacturing .....	40
Woven Roving WRE581T/ST94 Panels .....	40
Stitch-Bonded QE1203/ST94 Panels .....	43
Dogbone Specimen Machining .....	45
WET Conditioning .....	45
Fiber Volume and Void Volume Measurements .....	50
ASTM 2584-11 Burnoff .....	50
Microscopy Void Volume Approximation .....	53
Quasi-Static Testing & Modeling .....	53

Baseline Axial Laminate Tensile Modulus & Strength Testing.....	53
Baseline Sun/Li Model and Ply Discount Model.....	54
Pre-fatigue Modulus.....	57
Tension-Tension (T-T) Fatigue Testing.....	59
RTA T-T Fatigue Testing.....	61
WET T-T Fatigue Testing.....	64
Post-Fatigue Residual Modulus .....	67
Post-Fatigue Residual Strength .....	67
Sectioning, Polishing, and Microscopy.....	68
Sectioning.....	68
Polishing.....	69
Microscopy.....	71
Digital Scanning.....	75
Chapter 6 Experimental Results.....	78
Void Fraction .....	78
Microscopy.....	78
ASTM 2584-11 Burnoff.....	81
Baseline Modulus & Strength Measurements.....	82
Quasi-Static Predictions.....	82
Sun-Li Model Prediction of Quasi-Isotropic Properties.....	82
Panel Comparisons & Stress Strain Curves .....	85
Water Uptake Measurements .....	88
S-N Curve .....	90
RTA S-N Curve.....	90
WET & RTA S-N Curve.....	92
Modulus Reduction & Residual Strength .....	94
RTA.....	94
WET .....	102
Initial Displacement Amplitude Increase.....	105
RTA.....	105
Forensic Microscopy Analysis.....	108
RTA.....	108
Sample Scans .....	126
RTA.....	126
WET .....	139
Chapter 7 Conclusions & Future Work.....	147
Appendix A Halpin-Tsai and Sun-Li Model MATLAB Code .....	149
Appendix B Ply Discount Strength Prediction MATLAB Code .....	153
Appendix C Non-Technical Abstract.....	160

## LIST OF FIGURES

Figure 1-1. ARL rendition of a MHK Turbine rotor used for computational fluid dynamic analyses (Koudela, 2017). <i>Permission granted by ARL</i> .....	2
Figure 1-2. Patent involving a wind turbine blade manufacturing apparatus with guide pins to reduce unwanted displacement (Olsen et al., 2007) .....	5
Figure 2-1. Illustration of unidirectional composite laminate stacking sequence .....	10
Figure 2-2. Illustration of crossply composite laminate stacking sequence.....	10
Figure 2-3. Illustration of quasi-isotropic composite laminate stacking sequence .....	11
Figure 2-4. General shape of elastic modulus loss throughout an $R=0.1$ tension-tension fatigue test using finite element models of quasi-isotropic glass/epoxy laminates (based on Kennedy, 2013).....	15
Figure 2-5: Plot of tensile strength vs. conditioning time in Arabian Gulf seawater of a unidirectional glass/epoxy composite (based on Mourad et al., 2010) .....	19
Figure 2-6: Plot of tensile elastic modulus vs. conditioning time of glass/epoxy composite (based on Mourad et al., 2010).....	20
Figure 3-1. Illustrated cross section of a woven fiber-reinforced laminate showing movement of weft fibers during loading (Vectorply, 2016). <i>Permission granted by Vectorply</i> .....	25
Figure 3-2: Illustration of a multi-axial tricot-stitched laminate including a mat (Vectorply 2016). <i>Permission granted by Vectorply</i> .....	26
Figure 3-3: Diagram illustrating toughening mechanisms within thermoplastic-toughened epoxies (based on Meister, 2000).....	35
Figure 5-1. Four $[0^\circ/90^\circ]$ and four $[\pm 45^\circ]$ plies of WRE581T/ST94 twill weave prepreg awaiting hand layup .....	41
Figure 5-2. Woven and stitched laminates under vacuum bag before insertion into oven .....	42
Figure 5-3. Diagram of oven curing cycle for WRE581T/ST94 and QE1203/ST94 panels ...	42
Figure 5-4. Photograph of woven (left) and stitched (right) laminate pre-cured surfaces .....	44
Figure 5-5. Drawing of modified ASTM D638 Type III dogbone specimen used in testing program, dimensions in inches (ASTM, 2017).....	45
Figure 5-6. Bar chart depicting concentrations of compounds in ASTM D114 artificial seawater (ASTM, 2003) .....	47

Figure 5-7. WET specimens during air-dry period prior to weight measurement .....	47
Figure 5-8. Dogbone specimen weight measurement procedure including binder clips .....	48
Figure 5-9. Burnoff heating procedure including times and temperatures of holds .....	51
Figure 5-10. Remnants of burnoff procedure with woven sample (middle) and stitched samples (left & right) .....	52
Figure 5-11. Hydraulic grip, specimen block, extensometer, and specimen during pre-fatigue modulus testing .....	59
Figure 5-12. RTA T-T fatigue setup with hydraulic grips, extensometer, specimen, and cooling fans .....	62
Figure 5-13. Acrylic bucket WET testing setup with raised upper crosshead and unattached hose clamp .....	65
Figure 5-14. WET T-T fatigue setup with two compression fit O-rings to provide watertight seal .....	65
Figure 5-15. Full WET testing setup during fatigue loading including immersed specimen (viewed on edge), grips closed, hose clamp tightened, and cooling fans running .....	66
Figure 5-16. Longitudinal and transverse sectioning of virgin sample for microscopy .....	69
Figure 5-17. Four longitudinal sections mapped out prior to cutting .....	69
Figure 5-18. Longitudinal sections cut into four pieces.....	69
Figure 5-19. Polishing puck mold with extra composite piece for support .....	70
Figure 5-20. Diagram with labeled modifications to microscope for automated imaging .....	72
Figure 5-21. Initial microscopy cross section of specimen edge with unwanted brightness gradient.....	72
Figure 5-22. Microscopy cross section with new procedure for mitigating brightness gradient.....	73
Figure 5-23. Zoomed-in view of upper-left corner of Figure 5-22 .....	74
Figure 5-24. Example of scanned image with magnified image displaying macro cracks .....	76
Figure 6-1. Typical voids in the WRE581T/ST94 woven laminate including voids in the fiber direction and assorted matrix voids .....	78
Figure 6-2. Typical voids in the QE1203/ST94 stitched laminate including oblong voids, matrix voids between plies, and voids near stitches (top left).....	79

Figure 6-3. Example of one of the thirty-six 50x micrographs used for void fraction analysis.....	80
Figure 6-4. Comparison of quasi-static baseline results and Sun-Li model for stitch-bonded QE1203/ST94 quadaxial laminate with experimental results (dashed lines) shown as mean $\pm$ 1 std. dev.....	83
Figure 6-5. Comparison of quasi-static baseline results and Sun-Li model for woven roving WRE581T/ST94 [0°/90°] laminate with experimental results shown as mean $\pm$ 1 std. dev. ....	84
Figure 6-6. Stress-strain curves for three RTA baseline samples from each of the three panels manufactured for this study .....	86
Figure 6-7. Stress-strain curves between 0 and 2,660 $\mu\epsilon$ for three RTA baseline samples from each of the three panels manufactured for this study .....	86
Figure 6-8. Stress-strain curves for three RTA baseline and three WET conditioned baseline samples from the second stitched panel used for WET testing.....	87
Figure 6-9. Stress-strain curves for three RTA baseline and three WET conditioned baseline samples from the first stitched panel used for RTA testing .....	87
Figure 6-10. Stress-strain curves for three RTA baseline and three WET conditioned baseline samples from the woven panel used for RTA testing .....	88
Figure 6-11. Water uptake measurements for two conditioned stitched dogbone samples over two weeks (336 hours) .....	89
Figure 6-12. Water uptake models from Shen & Springer (1976) and Crank & Park (1999) plotted to predict saturation using weight uptake data points from two stitched samples with $D=2.8 \text{ mm}^2/\text{s}$ (Jones, 2003).....	89
Figure 6-13. RTA S-N curve including QE1203/ST94 (Stitched), WRE581T/ST94 (Woven), and PAC data at maximum fatigue stresses of 28.75, 24, and 18 ksi (PAC data from Koudela, 2016) .....	91
Figure 6-14. RTA S-N curve for stitched, woven, and PAC material systems including quasi-static strength data and trendlines with equations shown in matching colors (PAC data from Koudela, 2016) .....	92
Figure 6-15. WET and RTA S-N curve including QE1203/ST94(Stitched), WRE581T/ST94 (Woven), and PAC data at maximum fatigue stresses of 28.75, 24, and 18 ksi (PAC data from Koudela, 2016) .....	93
Figure 6-16. S-N curve for the two stitched panels including quasi-static strength data in both RTA and WET conditions and color-coded trendlines .....	94

Figure 6-17. Quantification of damage through plotting number of cycles vs. modulus reduction for RTA woven and stitched samples tested at 13.75 ksi maximum (includes linear trendlines).....	95
Figure 6-18. Quantification of damage through plotting number of cycles vs. change in tensile strength for RTA woven and stitched samples tested at 13.75 ksi maximum (includes linear trendlines).....	96
Figure 6-19. Quantification of damage through plotting modulus reduction vs. change in tensile strength for RTA woven and stitched samples tested at 13.75 ksi maximum (includes linear trendlines).....	97
Figure 6-20. Quantification of damage through plotting number of cycles vs. modulus reduction for RTA woven and stitched samples tested at 18 ksi maximum (includes linear trendlines) .....	98
Figure 6-21. Comparison of damage accumulation within 13.75 ksi maximum and 18 ksi maximum woven and stitched RTA specimens through plot of number of cycles vs. modulus reduction.....	99
Figure 6-22. Quantification of damage through plotting modulus reduction vs. change in tensile strength for RTA woven and stitched samples tested at 18 ksi maximum (includes linear trendlines).....	100
Figure 6-23. Quantification of damage through plotting modulus reduction vs. change in tensile strength for RTA woven and stitched samples tested at 18 ksi maximum (includes linear trendlines).....	100
Figure 6-24. Comparison of damage accumulation within 13.75 ksi maximum and 18 ksi maximum woven and stitched RTA specimens through plot of number of cycles vs. change in tensile strength.....	101
Figure 6-25. Comparison of damage accumulation within 13.75 ksi maximum and 18 ksi maximum woven and stitched RTA specimens through plot of elastic modulus reduction vs. change in tensile strength .....	102
Figure 6-26. Quantification of damage through plotting number of cycles vs. modulus reduction for RTA and WET samples tested at 13.75 ksi maximum (includes linear trendlines).....	103
Figure 6-27. Quantification of damage through plotting number of cycles vs. modulus reduction for RTA and WET samples tested at 18 ksi maximum (includes linear trendlines).....	103
Figure 6-28. Quantification of damage through plotting number of cycles vs. modulus reduction for RTA and WET samples tested at 13.75 and 18 ksi maximum (includes linear trendlines) .....	104

Figure 6-29. Quantification of damage through plotting number of cycles vs. change in tensile strength for RTA and WET samples tested at 13.75 and 18 ksi maximum.....	104
Figure 6-30. Residual Strength change over time for all WET stitched samples; far left baseline strengths apply to both data sets .....	105
Figure 6-31. Initial increase in extensometer-measured displacement amplitude for RTA woven and stitched data at 13.75 ksi maximum fatigue load.....	106
Figure 6-32. Initial increase in extensometer-measured displacement amplitude for RTA woven and stitched data at 18 ksi maximum fatigue load.....	107
Figure 6-33. Comparison of increase in extensometer-measured displacement amplitude for RTA woven (blue) and stitched data (red) at 13.75 (dashed) and 18 ksi maximum fatigue stresses (solid).....	108
Figure 6-34. Damage to a virgin woven sample's composite edge caused by polishing.....	109
Figure 6-35. Interior void or extended flaw without axial fiber damage inside a 10% modulus reduction 13.75 ksi maximum woven sample .....	109
Figure 6-36. Interior void or extended flaw and axial fiber damage within 16% modulus reduction 13.75 ksi maximum woven sample .....	110
Figure 6-37. Intralaminar cracks (circled) within a woven laminate loaded to 18 ksi maximum fatigue stress with 10% reduction in elastic modulus .....	111
Figure 6-38. One of numerous edge cracks distributed within an 18 ksi maximum, 16% modulus reduction woven sample .....	112
Figure 6-39. Longitudinal cut of 18 ksi maximum failed woven sample taken several inches away from the critical crack.....	113
Figure 6-40. Critical flaw in failed 18 ksi maximum woven sample surrounded by intralaminar cracks and delaminations.....	113
Figure 6-41. Relatively high density of intralaminar cracks found in non-critical flaw of 22 ksi maximum woven failed samples .....	114
Figure 6-42. Evidence of long interlaminar cracks within non-critical flaw of 22 ksi maximum woven failed samples.....	114
Figure 6-43. Virgin stitched RTA sample highlighting stitches found in micrograph without cracks .....	115
Figure 6-44. Stitched RTA sample loaded at 13.75 ksi maximum to 10% modulus reduction featuring an intralaminar crack in a 90° ply .....	117

Figure 6-45. Multi-laminar crack involving the specimen edge and internal stitches in 13.75 ksi maximum 16% modulus reduction stitched sample .....	118
Figure 6-46. Intralaminar crack bridging interlaminar cracks between 90° and 45° plies in stitched sample loaded at 13.75 ksi maximum to 16 % modulus reduction .....	118
Figure 6-47. Stitched RTA sample loaded at 18 ksi maximum to 10% modulus reduction featuring intralaminar cracks in a 45 and 90° ply .....	120
Figure 6-48. Long crack found in resin-rich area around stitches within an 18 ksi maximum stitched sample at 10% modulus reduction.....	121
Figure 6-49. Copious wide intralaminar cracks within stitched 18 ksi maximum 16% modulus reduction specimen.....	122
Figure 6-50. Numerous intralaminar cracks within 16 plies of a failed 18 ksi maximum stitched sample (non-critical cross-section) .....	123
Figure 6-51. Long interlaminar cracks affected by stitches within 18 ksi maximum stitched sample (non-critical cross section) .....	124
Figure 6-52. Critical flaw within 18 ksi maximum failed sample complete with delaminations of nearly every ply and numerous interlaminar cracks .....	125
Figure 6-53. Few intralaminar cracks with predominantly interlaminar failure in failed 24 ksi maximum stitched sample .....	126
Figure 6-54. Scan of woven virgin sample showing a baseline for comparison with damaged samples. ....	127
Figure 6-55. Scan of 13.75 ksi maximum woven sample at nearly 10% modulus reduction ..	128
Figure 6-56. Scan of 13.75 ksi maximum woven sample at nearly 13% modulus reduction ..	129
Figure 6-57. Scan of 13.75 ksi maximum woven sample at nearly 16% modulus reduction ..	129
Figure 6-58. Scan of 18 ksi maximum woven sample at nearly 13% modulus reduction .....	130
Figure 6-59. Scan of critical crack of woven sample failed at 28.75 ksi maximum fatigue stress.....	131
Figure 6-60. Scan of critical crack of woven sample failed at 24 ksi maximum fatigue stress.....	132
Figure 6-61. Scan of critical crack of woven sample failed at 18 ksi maximum fatigue stress.....	132
Figure 6-62. Virgin stitched sample for comparison to damaged samples .....	133

Figure 6-63. Scan of 13.75 ksi maximum stitched sample at nearly 10% modulus reduction.....	134
Figure 6-64. Scan of 13.75 ksi maximum stitched sample at nearly 13% modulus reduction.....	134
Figure 6-65. Scan of 13.75 ksi maximum stitched sample at nearly 16% modulus reduction.....	135
Figure 6-66. Scan of 18 ksi maximum stitched sample at nearly 13% modulus reduction .....	136
Figure 6-67. Scan of critical crack of stitched sample failed at 28.75 ksi maximum fatigue stress.....	137
Figure 6-68. Scan of critical crack of stitched sample failed at 24 ksi maximum fatigue stress.....	138
Figure 6-69. Scan of critical crack of stitched sample failed at 18 ksi maximum fatigue stress.....	139
Figure 6-70. Scan of WET conditioned, but unloaded stitched sample without polysulfide edge seals .....	140
Figure 6-71. Scan of WET stitched sample tested to 10% modulus reduction at 13.75 ksi maximum .....	141
Figure 6-72. Scan of WET stitched sample tested to 13% modulus reduction at 13.75 ksi maximum .....	141
Figure 6-73. Scan of WET stitched sample tested to 16% modulus reduction at 13.75 ksi maximum .....	142
Figure 6-74. Scan of WET stitched sample tested to 10% modulus reduction at 18 ksi maximum .....	142
Figure 6-75. Scan of WET stitched sample tested to 16% modulus reduction at 13.75 ksi maximum .....	143
Figure 6-76. Scan of critical crack of WET stitched sample failed at 28.75 ksi maximum fatigue stress.....	144
Figure 6-77. Scan of critical crack of WET stitched sample failed at 24 ksi maximum fatigue stress.....	145
Figure 6-78. Scan of critical crack of WET stitched sample failed at 18 ksi maximum fatigue stress.....	146

## LIST OF TABLES

Table 5-1. Summary of laminate manufacturing and textile properties.....	44
Table 5-2. Input composite properties for Halpin-Tsai/Sun-Li models using properties for E-glass and known ST94 resin elastic modulus .....	55
Table 5-3. Textbook values for ply strengths used in Tsai-Wu portion of the ply discount strength model (Daniel & Ishai, 2006).....	57
Table 5-4. RTA & WET test plan (note: WET testing was not performed on Woven samples) .....	61
Table 5-5. Polishing procedure parameters including grits, rotational speeds, pressures, and cycle times.....	71
Table 5-6. Microscope digital imaging parameters .....	73
Table 6-1. Microscopy-determined void fraction results utilizing Gaussian and Weibull statistics.....	80
Table 6-2. Burnoff void fraction results for RTA Stitched & Woven and WET Stitched samples.....	81
Table 6-3. Baseline modulus and strength quasi-static testing results reported in MPa and ksi (Juska, 2016) (Strauch, 2016).....	82
Table 6-4 Results from ply-discount strength predictions using Tsai-Wu failure criterion with total applied stresses listed for each ply failure .....	85

## ACKNOWLEDGEMENTS

I would like to acknowledge The Pennsylvania State University Applied Research Laboratory (ARL) for providing me with the ARL Walker Graduate Assistantship, making my graduate studies possible. Furthermore, the United States Department of Energy should be recognized for provided funding through DOE Grant DE-EE0007176. I also would like to thank the faculty and staff of the Department of Engineering Science and Mechanics for academic and moral support during my transition from undergraduate to graduate student.

Additionally, several individuals significantly contributed to the success of this research project. Foremost, I would like to recognize my academic co-advisers, Dr. Kevin Koudela and Dr. Charles Bakis, for their patience and mentorship throughout the past year. Dr. Bakis also provided the MATLAB code for calculating the 3D elastic properties of the composite laminates originally written by Dr. Ying Shan. I also want to thank Eric Strauch, Dr. Thomas Juska, Christopher Rachau, Stephen Struble, Clark Moose, Rance Maruszewski, Russell Armstrong, and Deborah Corl from the ARL Composite's Material Division for their support with fatigue testing, microscopy, panel manufacturing, polishing, scanning, safety training, specimen cutting, and project coordination, respectively. Additionally, I would like to thank Aniruddh Vashisth and Jeffrey Kim for their technical and academic assistance throughout the testing and writing process. I would also like to thank Dr. Clifford Lissenden and Dr. Judith Todd for their time in reviewing this thesis.

Finally, I would like to thank my family and friends for their unconditional support of my academic adventure. I would especially like to thank my girlfriend, Laurena Clemente, for her continuous encouragement and editorial assistance. All of your support does not go unnoticed.

## **Chapter 1**

### **Literature I: Hydrokinetic Turbine Technologies and Analysis**

#### **Hydrokinetic Energy and Background**

Hydropower is far from a new technology and encompasses many forms of power generation. Many cities around the world depend on conventional, gravity-driven hydroelectric energy generation. However, hydroelectric plants require large dams and accompanying reservoirs built at different altitudes, thus, the costs of designing, building, and maintaining hydroelectric plants discourage many areas from using hydroelectric power. Hydrokinetic turbines, which harness the power of natural tidal or weather-induced water currents, have gained popularity as the new global trend towards sustainable energy has developed.

Through hydrokinetic turbines, cities can harvest energy from its waterways without the need for a massive construction project. Hydrokinetic systems are also more customizable since energy production can be tailored to a city's energy requirements by varying the size and quantity of turbines. Hydrokinetic turbines are similar to wind turbines, except water currents turn the blades instead of air currents. Figure 1-1 displays the general shape of a hydrokinetic turbine. Specifically, Figure 1-1 shows a computational fluid model of a horizontal-axis hydrokinetic turbine designed by Verdant Power, Inc. and modelled by The Pennsylvania State University Applied Research Lab (ARL).

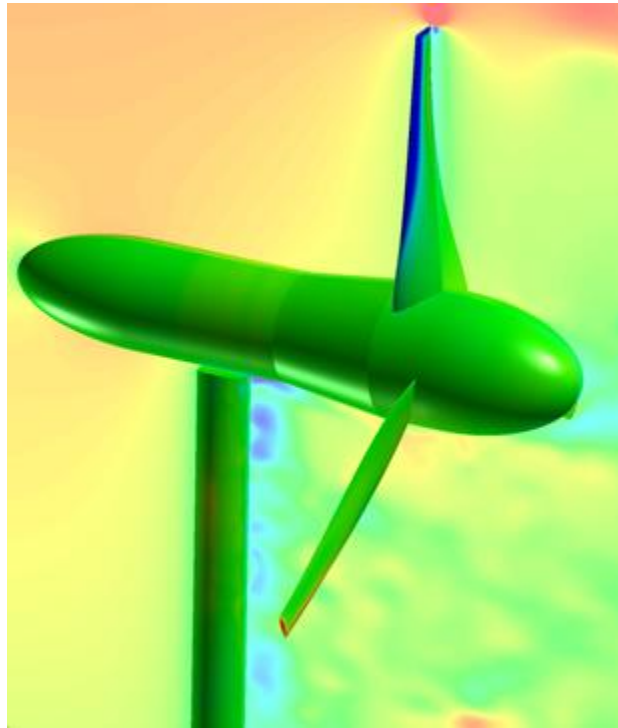


Figure 1-1. ARL rendition of a MHK Turbine rotor used for computational fluid dynamic analyses (Koudela, 2017). *Permission granted by ARL.*

Verdant Power, Inc. is one of many companies who have already developed a fully-operational hydrokinetic turbine system. After an analysis of potential sites for marine hydrokinetic turbine use in the US, the East River in New York was chosen as one of four locations with a high flow rate waterway. The East River is cited to have an average flow rate of 1.0 m/s, offering a potential 3.61 million MWh/yr. The East River is technically not a river, but a narrow tidal estuary that connects the Long Island Sound to the New York Bay, flowing less than four knots in either direction depending on ocean currents at its source and mouth. Verdant Power, Inc. has already installed hydrokinetic turbines into the East River and connected an array of six stations to the grid, which produced 50 MWh during a six-month trial period (Laird et al., 2013).

Still, hydroelectric power stations can produce substantially more energy than small-scale hydrokinetic projects. In comparison, large hydroelectric plants, such as the Hoover Dam, can

produce over four million MWh per year (United States, 2006). Even an average on-shore wind turbine can produce over 4,700 MWh annually (Wind Energy, 2016). Thus, hydrokinetic projects are targeted for areas where dams and wind turbines are not viable, such as rivers near metropolitan areas. These areas would benefit from the nearby harvestable waterway because power transmission losses would be low since power generation occurs in close proximity to areas of high electrical power usage. Furthermore, the cost of production for hydrokinetic power generation decreases as more turbines are produced. This same trend was found as wind turbines became more popular (Bedard et al., 2007).

Each Verdant-designed hydrokinetic turbine utilizes three unducted blades with a five-meter overall spin diameter. The turbine sits atop a pylon supported foundation and has a nacelle pivot to account for the bi-directional flow in the East River. The blades of the hydrokinetic system have become the focal point of structural/materials research because they have been cited as a major source of damage or even failure. Therefore, creating designs that would improve each blade's service life would result in reduced maintenance costs for hydrokinetic power generation. Research into potential solutions intended to extend service life have included improving the composite structure that comprises the blade. However, complexity arises due to the natural cyclic, multiaxial loading that the blade encounters during use (Laird et al., 2013).

These complexities make understanding the fatigue behavior of the composite blade's constituent material within the blade's service environment paramount. Ensuing chapters will explain composite behavior in marine environments as well as well-studied damage and failure mechanisms of fiber-reinforced polymers with complex fiber architectures often used to reduce cost and simplify manufacturing. This study will provide cyclic-load testing and forensic failure analysis results to characterize fatigue behavior of a pre-determined composite material system chosen for use in future hydrokinetic blades.

## **Structural Hydrokinetic Blade Design**

Traditional hydrokinetic turbine blades consist of a pressure and suction side connected by shear webs. Oftentimes, these components consist of a composite sandwich structure. The blade geometry is dictated by several environmental factors including maximum rotational velocity, water depth/density, and maximum operational stresses/strains. Additionally, the blade must adequately mate with the root hub attachment (Sale et al., 2013). Some blades are hollow while others are filled with structural foam. A few designs even aim to make the blade neutrally buoyant in order to minimize buoyancy loads and thus the stress amplitude of cyclic loading (Bir et al., 2011).

Grogan et al. (2013) noted that quasi-isotropic layups are used in hydrokinetic turbine blades in order to account for the multi-axial stress state imposed by the blades' rotational movement. To determine if a certain composite design would suffice, a program called PreComp, developed by The National Wind Technology Center for processing composite blade technologies, was slightly modified and used to calculate strains in the hydro-kinetic blade during operation. Using this software, the authors determined that the quasi-isotropic layup would work best. They also found that a carbon-fiber reinforced polymer (CFRP) outperformed a glass-fiber reinforced polymer (GFRP) in terms of failure strain, although, the cost associated with CFRP may not be worth its structural advantage over GFRP. However, the authors speculate that GFRP fiber-matrix bond may be reduced by the saline environment more than CFRP.

Several blade designs incorporated structural health monitoring (SHM) as well. Chandrashekhara (2012) created a wireless SHM system by imbedding fiber-optic strain gauges within the blade. The design utilized an internal sound-based transmitter and external receiver to relay strain data from the embedded strain gauge to a more-powerful above-ground wireless transmitter. The structural health data relayed fatigue data to hint at when and where repair

patches are needed. Additionally, the health system could classify and quantify damage from the surrounding environment including fish impacts, earthquakes, and flooding (high water levels).

### Manufacturing Methods

There is little literature on the manufacturing of hydrokinetic blades, but copious information on the production of wind turbine blades exists. One method of manufacturing composite blades is a two-part mold apparatus. When the apparatus is closed, an adhesive bonds the two pre-cured blade halves into one solid blade. The invention displayed in Figure 1-2 is designed to bond two blade halves quickly and accurately, relying on guide rods (items 10 and 12) to ensure the halves mate properly during the molding process. This movement stems from the geometry of long, bulky wind turbine blades. Additionally, the hinge mechanism (item 7) is noteworthy as it eases the manufacturing process (Olsen et al., 2007).

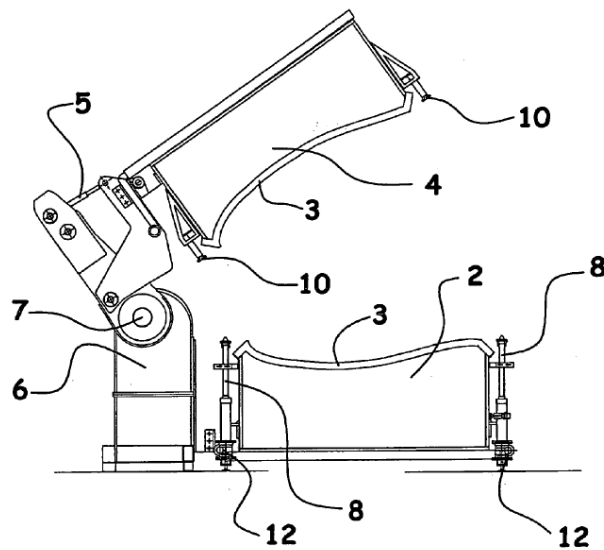


Figure 1-2. Patent involving a wind turbine blade manufacturing apparatus with guide pins to reduce unwanted displacement (Olsen et al., 2007)

Habali et al. (2000) laid out a method of manufacturing a wind turbine blade and testing the blade for performance characteristics. Prior to constructing a composite blade, a full-scale wooden blade was crafted so that the geometry of the blade could be approved and so a mold could be produced. This five-meter long wooden blade was split into 12 sections that were eventually bonded together using epoxy. Fiber glass was then laid up around the wooden model to create a two-part mold for composite blades. The two blade halves were then manufactured using the molds and were bonded at the two edges of the airfoil with a central spar for support. A steel flange was installed at the root to connect the blade to the turbine. The mating flange consisted of two halves that were joined around the root and bonded using adhesive and tack welding. The 120-kg blade was then tested on a fixture for efficiency studies.

### **Previous Methods of Analysis**

Many research teams have already developed useful ways to determine the stress or strain state within a composite hydrokinetic blade. Sale et al. (2013) used a method of incorporating statistical variance of mechanical properties in a simulation to determine the probability of different failure modes. In this study, the elastic and shear moduli as well as the Poisson's ratio and density of the composite were varied using a distribution with the known value of the composite set as the mean and a coefficient of variation of 0.1. An open-source blade-evaluation tool, named Co-Blade, was used to model the composite blade, evaluate maximum deflections and stress states within the blade, and optimize the design through a constraint-conscious weight minimization feature. The structural evaluation features in Co-Blade relied on a combination of classical lamination theory, Euler-Bernoulli theory, and shear flow theory. Using the same applied loads, 2,000 random combinations of material properties were chosen and modeled. The models showed that the most common failure mode is a compressive failure in the spar caps.

Other notable failure modes include tensile failure in the blade shell, buckling on the leading and trailing edges, and buckling in the blade tip.

Fatigue analyses have also been conducted. Grogan et al. (2013) mentions a brief fatigue study whose initial predictions showed a reduction in failure strain of 50% after a 20-year span equating to 10M cycles. However, the software used for blade property calculations, PreComp, is known for overdesigning blades with safety factors related to potential composite deterioration caused by seawater.

In fact, the specific marine environment in which the composite blades operate have a major impact on the design of the blades. As discussed by Chen and Lam (2015), tidal current turbines are often damaged by the marine environment in which they harness their energy. Five abiotic sources of marine-based damage include extreme weather, seabed scour, fatigue failure, corrosion/erosion, and marine fouling. Seabed scour refers to both eroded seabed particulates interacting with the blade as well as the process of moving water removing seabed around the foundation of an anchored, static structure. Due to the randomness of ocean currents, fatigue life is difficult to calculate since loading cycles are not always consistent. During storms, water turbulence can cause extreme loads; a 12% increase in turbulence intensity can yield a stress level six times higher than with no turbulence. In addition to mechanical failures, particulate impacts and marine life presence will also take their toll on long-service composite blades.

## References

- Bedard, R., Previsic, M., Hagerman, G., Polagye, B., Musial, W., Klure, J., Von Jouanne, A., Mathur, U., Collar, C., Hopper, C., & Amsden, S. (2007, September). North American ocean energy status—March 2007. In *7th European Wave and Tidal Energy Conference (EWTEC)*, Lisboa, Portugal: Instituto de Engenharia Mecanica. (pp. 11-13).
- Bir, G. S., Lawson, M. J., & Li, Y. (2011, January). Structural design of a horizontal-axis tidal current turbine composite blade. In *ASME 2011 30th International Conference on Ocean, Offshore and Arctic Engineering* (pp. 797-808). New York, NY: American Society of Mechanical Engineers.
- Chandrashekhara, J. R. K. (2012). Remote Monitoring of the Structural Health of Hydrokinetic Composite Turbine Blades (No. 1). DOE EERE – Wind & Water Power Program. Missouri University of Science & Technology. Rolla, MO. Award number DE-EE0004569.
- Chen, L., & Lam, W. H. (2015). A review of survivability and remedial actions of tidal current turbines. *Renewable and Sustainable Energy Reviews*, 43, 891-900.
- Grogan, D. M., Leen, S. B., Kennedy, C. R., & Brádaigh, C. Ó. (2013). Design of composite tidal turbine blades. *Renewable energy*, 57, 151-162.
- Habali, S. M., & Saleh, I. A. (2000). Local design, testing and manufacturing of small mixed airfoil wind turbine blades of glass fiber reinforced plastics: Part II: Manufacturing of the blade and rotor. *Energy conversion and management*, 41(3), 281-298.
- Laird, D. L., Johnson, E. L., Ochs, M. E., & Boren, B. (2013). Technological cost-reduction pathways for axial-flow turbines in the marine hydrokinetic environment (Rep. No. SAND2013-7203). Sandia National Laboratory, Department of Energy. Albuquerque, NM.
- Olsen, S. M., Jensen, F. R., Klindt, P., & Liebmann, A. (2007). *U.S. Patent No. 7,223,091*. Washington, DC: U.S. Patent and Trademark Office.
- Koudela, K. (2017, July). Personal correspondence. University Park, PA: The Pennsylvania State University Applied Research Laboratory.
- Sale, D., Aliseda, A., Motley, M., & Li, Y. (2013, April). Structural optimization of composite blades for wind and hydrokinetic turbines. In *1st Marine Energy Technology Symposium*. Washington D.C.: National Hydropower Association.
- United States. Bureau of Reclamation. Lower Colorado Region. (2006). Hoover Dam. Boulder City, Nev.: U.S. Dept. of the Interior, Bureau of Reclamation, Lower Colorado Region. Boulder City, NV.
- Wind Energy Statistics and Targets. The European Wind Energy Association. [http://www.ewea.org/uploads/pics/EWEA\\_Wind\\_energy\\_factsheet.png](http://www.ewea.org/uploads/pics/EWEA_Wind_energy_factsheet.png). Web. 16 Nov. 2016.

## **Chapter 2**

### **Literature II: Effects of Marine Environments on Polymer Composite Structures**

#### **Brief Introduction of Polymer Matrix Composites**

Following a few millennia of using natural materials and metals to form load-bearing structures, the rise of artificial polymers in the late 19th century provided the potential to develop novel, light-weight structures. Throughout the 20th century, natural and artificial (glass/graphite/aramid) fibers were suspended in polymers to provide added strength and stiffness to the mix, giving these new polymer matrix composites (PMCs) structural integrity comparable to their metal alloy counterparts, but at a fraction of the weight. However, the reinforcement is only provided in the direction that the thin fibers extend. Thus, composites are also highly customizable since composite properties can be altered by manipulating the direction of the fibers.

The simplest form of PMCs are unidirectional tape laminates that consist of a vertical stack of individual plies. A ply refers to one layer of the PMC composite where fibers are typically aligned in one direction. If the composite is a unidirectional laminate, all of the plies are aligned in the same direction. This gives the composite superior strength and stiffness in that direction, but reduces properties in other directions. An illustration of how a unidirectional tape laminate composite stacks up is shown in Figure 2-1. The fiber direction is depicted using the thin interior lines within the plies. The thickness of each of the four plies in the laminate is exaggerated in the illustration for simplicity of viewing.

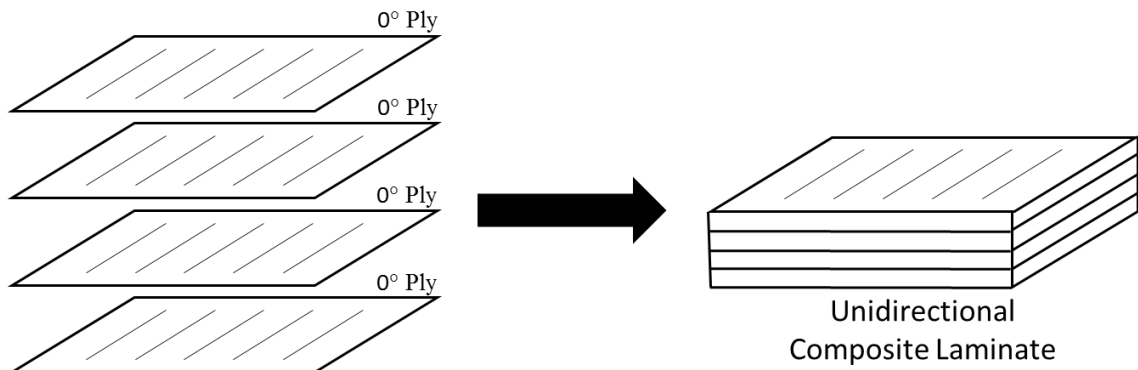


Figure 2-1. Illustration of unidirectional composite laminate stacking sequence

To counteract the weakness that comes transverse (perpendicular) to the aligned fibers, some laminates are stacked such that some plies are aligned in one direction while others are aligned transverse. The simplest of these laminates are called crossply laminates. A typical crossply laminate stacking sequence is illustrated in Figure 2-2. This laminate is also symmetric, meaning the plies are stacked in reverse order after reaching the middle of the laminate, called the mid-plane.

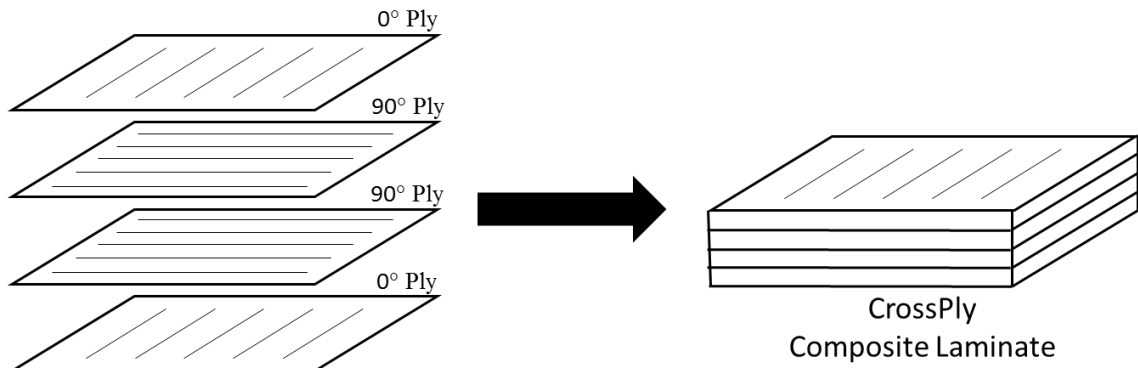


Figure 2-2. Illustration of crossply composite laminate stacking sequence

Still, the crossply laminate is weak in the directions offset  $45^\circ$  from any of the fibers. Thus, quasi-isotropic layups are used when properties should be nearly equivalent in all directions. In most cases, elastic modulus remains nearly constant in all direction while strength

still varies when measured at offset angles. Nevertheless, quasi-isotropic laminates are often implemented when structures undergo complex loading such as multiaxial stress states. An example of a quasi-isotropic layup is displayed in Figure 2-3. It is important to note that the plies are balanced, which denotes that there is an equal distribution of fibers (specifically, fiber areal weight) in the offset angled plies. In the case of the laminate in Figure 2-3, this means there are an equal number of  $+45^\circ$  and  $-45^\circ$  plies and that there are pairs of  $0^\circ$  and  $90^\circ$  plies. A balanced laminate will not distort due to residual stresses caused by heating and cooling during manufacturing.

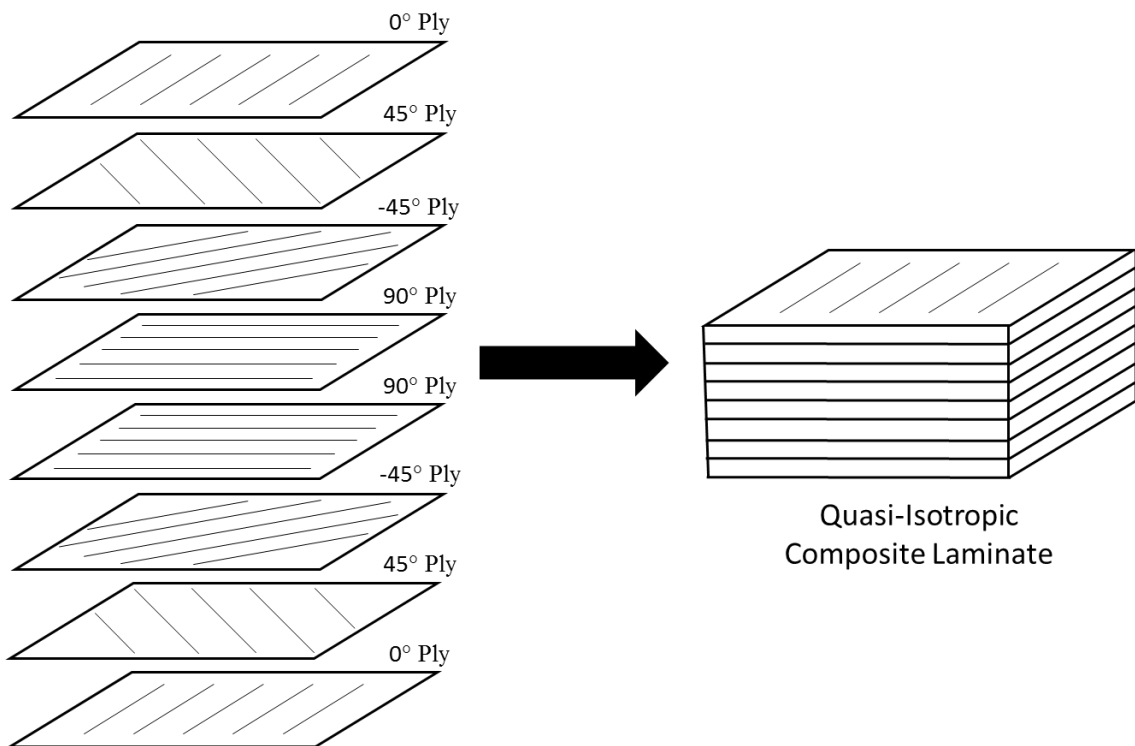


Figure 2-3. Illustration of quasi-isotropic composite laminate stacking sequence

PMCs also demonstrate resistance to corrosion in marine environments. While metals tend to degrade under oxidation, polymers tend to absorb moisture and incorporate the absorbed water in its internal structure (Mourad et al., 2010). This makes PMCs valuable in structures that

perform in marine environments since PMCs have the potential for longer service lives compared to other materials.

### **Water Absorption and Elevated Temperature Conditioning Effects**

When immersed in water, glass epoxy composites tend to absorb water through diffusion. The rate of diffusion in polymers has been characterized by several diffusion-based analyses. Crank and Park (1999) provided a concise Fickian model to predict water absorption in polymer resins. This is displayed in Equation 1 where  $M_t$  represents percentage weight gain at time,  $t$ ,  $M_\infty$  is the percentage weight gain at saturation,  $D$  is the diffusion coefficient in  $\text{mm}^2/\text{s}$ , and  $d$  is the specimen thickness in mm.

$$\frac{M_t}{M_\infty} = \left(\frac{4}{\sqrt{\pi}}\right) \left(\frac{Dt}{d^2}\right)^{\frac{1}{2}} \quad (1)$$

Shen and Springer (1976) offer an alternative polymer moisture absorption model, displayed in Equation 2, which can be applied in conditions where the specimen has a relatively low thickness to surface area ratio.

$$M_t = M_\infty \left(1 - e^{-7.3\left(\frac{Dt}{d^2}\right)^{0.75}}\right) \quad (2)$$

Conditioning environments affect composite mechanical property degradation. Abdel-Magid et al. (2005) investigated glass/epoxy composites submerged in distilled water at different temperatures under a constant tensile load equal to a fifth of the material's ultimate tensile strength. Although the specific type of laminate is undisclosed by the authors, it can be inferred that a  $0^\circ$  unidirectional laminate was used based on the description of modulus predictions through rule of mixtures. Samples were both submerged and loaded at room temperature or at  $65^\circ\text{C}$  from 500 to 3,000 hours. Those conditioned at room temperature for 500 hours incurred a

5% increase in strength and an 11% decrease in elastic modulus compared to control samples.

The initial increase in strength can be attributed to plasticization/softening of the matrix, which permits alignment fibers to wiggle into alignment with the load. Matrix plasticization results from epoxy absorbing water from the surrounding environment, thus increasing the volume of the composite. Plasticization also accounts for an increase in tensile failure strain. However, there is a critical point in absorbed water where hydrostatic pressure at crack tips promote crack propagation and brittle failure dominates. In this region, after 3,000 hours, room temperature samples suffered a 35% reduction in tensile strength, 9% reduction in elastic modulus, and a 32% reduction in failure strain. The elevated temperature specimens conditioned at 65°C for 1,000 hours encountered a 28% reduction in tensile strength and a 28% reduction in elastic modulus. The high magnitude of elastic modulus reduction compared to the tensile strength reduction of elevated temperature specimens alludes to the effect of accelerated aging on glass/epoxy composites. The authors believe that the elevated temperature allowed the water to attack the silane couplings at the fiber-matrix interface and also expand initially minor interlaminar cracks.

Davies et al. (2001) tested glass/epoxy composites conditioned in both saline seawater and distilled water. Prior to testing, specimens were conditioned for a year and a half at 20°C and 50°C in seawater and 50°C in distilled water. The authors point out that a 10°C increase in conditioning temperature increases the rate of diffusion two-fold. The conditioning containers were plastic to discourage corrosion. Samples were not mechanically tested submerged in water, but were tested immediately after they were removed from the bath to minimize drying. Weight gain was tracked during the conditioning phase of testing and distilled water induced water absorption faster than seawater at the same temperature. Tensile tests were performed on neat resins and results showed no statistically significant change in tensile modulus of the epoxy after aging. However, when samples were dried after aging, a noticeable increase in elastic modulus was measured while tensile strength decreased nearly 40%. In this investigation, composite

specimens were laid up as  $\pm 45^\circ$  plies and tested in shear. For both shear modulus and shear strength, the specimens aged in distilled water saw a slightly higher reduction in mechanical properties compared to those aged in seawater. All specimens saw between 20-25% reductions in shear modulus and shear strength after conditioning at 50°C for 18 months.

### **Wet & Elevated Temperature (WET) Conditioning Degradation Mechanisms**

Abdel-Magid et al. (2005) touched upon the importance of the fiber-matrix bond and pre-existing cracks as key targets of absorbed water during the degradation of glass/epoxy composites. However, other authors provided a more in-depth analysis of water conditioning damage mechanisms. Kennedy (2013) provided an extensive overview of fatigue in GFRP composites in marine environments. The author stated that water can add nearly 5% to a GFRPs weight and the absorbed water can cause between 20 to 25% knockdowns in tensile strength after high-stress fatigue loading. Specifically, Kennedy tested and modeled quasi-isotropic glass/epoxy laminates in tension-tension fatigue at  $R=0.1$ . The stress ratio,  $R$ , refers the ratio of the minimum to the maximum stress of the fatigue cycle. Kennedy also reported a fatigue curve for the general shape of elastic modulus reduction throughout the life of a given fatigue test, which is shown in Figure 2-4.

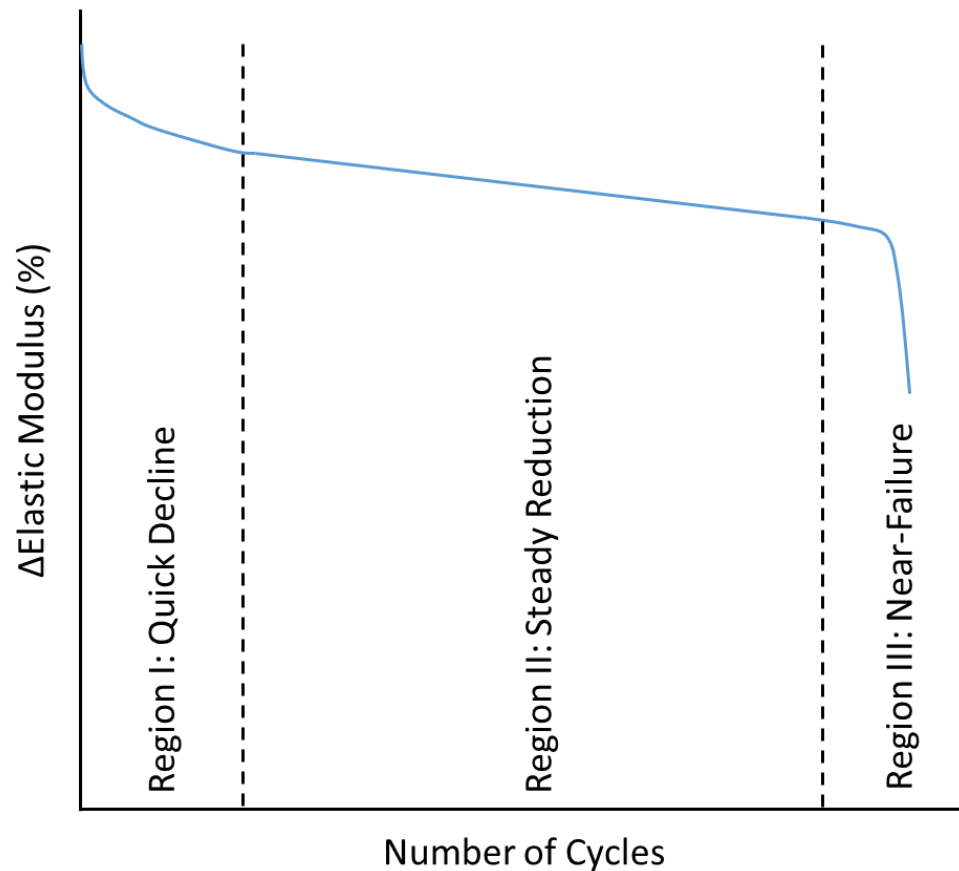


Figure 2-4. General shape of elastic modulus loss throughout an  $R=0.1$  tension-tension fatigue test using finite element models of quasi-isotropic glass/epoxy laminates (based on Kennedy, 2013)

Kennedy (2013) also mentioned that, when submerged in water, GFRPs do not corrode electrochemically like metals, but instead takes in water. When the water enters the matrix, the water molecules diffuse and settle into any defects in the composite such as voids or manufacturing defects. The molecules can also chemically interact with the matrix causing a reduction in crosslink density, which degrades mechanical properties. If the water is saline, microscopy has shown that salt ions do not typically enter the matrix but may hinder the diffusion of water molecules into the polymer. Once the water has entered the composite, the water molecules can hydrolyze the sizing compounds and can weaken the bonds between fiber and matrix. Additionally, water molecules can induce stress corrosion cracking (SCC) on glass fibers

by accelerating the growth of pre-existing cracks in the fibers through attacking crack tips. SCC gets its name from the acceleration of material degradation due to applied loading. There are several varying proposed mechanisms for SCC of glass fibers in salt water, but the commonality in the mechanisms suggest that sodium ions react and dissolve the solid glass fiber. Even when organosilane coupling agents are used to improve bonding at the fiber-matrix interface and inhibit stress corrosion cracking, saturated water can attack the interface bond and promote SCC of fibers. Glass fibers become prone to early fracture due to SCC. The author reported a 26% reduction in quasi-static determined tensile strength due to elevated temperature water conditioning. In fatigue, the conditioned specimens saw a 20% reduction in fatigue strength at one thousand cycles, but only an 8% reduction at one million cycles. Matrix plasticization caused by the ingress of water consequently allows 0° fibers to align with the load direction. Alternatively, the quasi-isotropic specimens only lost 1% in elastic modulus due to the same conditioning. Due to the quasi-isotropic samples' small loss in modulus, the author mentions that weakening of the fiber-matrix bond and SCC of glass fiber affect fatigue strength more than matrix plasticization

Pauchard et al. (2002) argued the brittle fracture of glass fibers resulting from submersion in water can be predicted using fracture mechanics models and can subsequently be used to predict fatigue life. The authors studied a glass/epoxy unidirectional laminate for their investigation. Equation 3 shows a model to predict fatigue life of fibers under sinusoidal fatigue loading given several variables: failure time,  $t_f$ , stress ratio,  $R$ , sub-critical crack growth rate,  $\frac{da}{dt}$ , fracture toughness,  $K_{IC}$ , crack-shape parameter,  $Y$ , unconditioned strength of fiber,  $\sigma_i$ , and material parameters  $A$  and  $n$  deriving from Equation 4.  $K_{IC}$  defines the critical stress-intensity factor,  $K_I$ , of a crack that has reached its maximum crack length for a given crack geometry and load.

$$\int_0^{t_f} \left[ \sigma_{max} \left[ \frac{1+R}{2} + \frac{1-R}{2} \sin \left( 2\pi t \left( \frac{da}{dt} \right) \right) \right] \right]^n dt = \frac{(2K_{IC}^{2-n})}{AY^2(n-2)} \sigma_i^{n-2} \quad (3)$$

$$\frac{da}{dt} = AK_I^n \quad (4)$$

Pauchard et al. (2002) also states that SCC in glass fibers occurs relatively early in fatigue life in water-conditioned and aged glass/epoxy composites. Therefore, the failure of fibers may aid in the initial reduction in stiffness. When investigated, the authors found that initial reduction in stiffness in fatigue samples was directly proportional to the quantity of failed fibers. This indicates that fracture of the micro-sized fibers contributes to the detriment of the composite's macro-scale properties.

Jones (2003) claimed that although epoxy resins tend to absorb more water than other polymer resins, glass/epoxy unidirectional 0° composites still fail based on fiber fracture. The author stated that the ability of a thermoset polymer resin depends heavily on the polarity of the molecular structure, the degree of crosslinking, and the presence of residuals. Due to this, epoxy resins tend to have a higher saturation concentration of water ( $M_\infty = 6.9$  wt. %) and a lower diffusion coefficient ( $D = 2.8 \text{ mm}^2\text{s}^{-1}$ ) compared to polyester or cyanate ester resins, which are known for their low-cost and easy manufacturing process. While the absorption of water may affect damage mechanisms, the author suggests that fatigue lifetime predictions can be devised based on the fracture of the glass fibers. These predictions involve fracture mechanics incorporating probability of failure through a Weibull distribution. The fracture mechanics equations are used to find the point of initial failure in glass fibers where brittle fracture occurs as pre-existing defects propagate to a critical length. The author relates the three regions of stress to crack growth in the fibers as opposed to the matrix. It should be noted that the author states that the delivery of sodium ions to the glass fibers causes SCC of the fibers' silica network. In stage I (high-stress region), fracture occurs without effects of SCC since the water cannot deliver sodium

ions to the cracks before mechanical loads induce fracture. In moderate stress stage II, corrosion of the glass fibers allows flaws to propagate faster. In low stress stage III, hydrolysis of the fibers' silica network prevails. SCC actually increases the radius of crack tips in this stage and hinders crack propagation.

Contrasting with Jones, Mourad et al. (2010) argued that hydrolysis and plasticization caused by absorbed water still plays a major role in the degradation of mechanical properties. As other authors have stated, hydrolysis and plasticization lead to alterations in the matrix's chemical structure. The magnitude of their effects is related to the amount of water absorbed from the surrounding environment. Using room temperature seawater that was collected in the Arabian Gulf, composite weight gain was found to be 0.9%, 1.3%, and 2.5% after 3, 6, and 12 months, respectively. With water heated to 65°C in those same time intervals, weight gain was measured at 2.8%, 2.9% and 5%. This increase is caused by the dependence of molecular diffusion on temperature. X-Ray spectra were taken pre-and post-conditioning to determine if residual ions from sea water were also absorbed into the glass/epoxy specimens. The authors found that residual ions did not enter the composite, although, they did find reductions in sodium and magnesium concentrations in conditioned samples. This leaching of sodium and magnesium ions from the sample into the water indicates that the absorbed water chemically degrades the fiber-matrix interface, thus weakening the composite. Leaching refers to the dissolution of sodium ions in glass fibers into the surrounding water.

The effect of this degradation on tensile strength and elastic modulus is plotted in Figure 2-5 and Figure 2-6. When conditioned at room temperature, the composite initially suffers from a 10% reduction in tensile strength, followed by an increase to a higher strength than the control, and finally returning to a strength similar to the control. The preliminary reduction in strength after three months is said to be caused by the non-uniformity of water uptake within the composite. The gradient of absorbed water causes an uneven stress distribution within the

composite. The authors further state that the relatively high scatter shown in the data results from defect-controlled failures. As the absorbed water reaches equilibrium within the composite, the presence of stress concentrating flaws as well as residual stresses resulting from manufacturing diminish, which lead to the eventual increase in strength. Additionally, matrix swelling caused by hydrolysis can improve the fiber-matrix bond by squishing matrix and fibers together. Hydrolysis refers to the reaction of the polymer matrix and absorbed water resulting in swelling. After this, absorbed water slowly attacks the fiber-matrix interface and gradually reduces strength. When conditioned at 65°C, specimens encounter a similar progression at a faster pace. This faster pace means that the initial release in residual stresses, and the following plasticization, leaching, and hydrolysis all occur in less time than specimens conditioned at room temperature (Mourad et al., 2010).

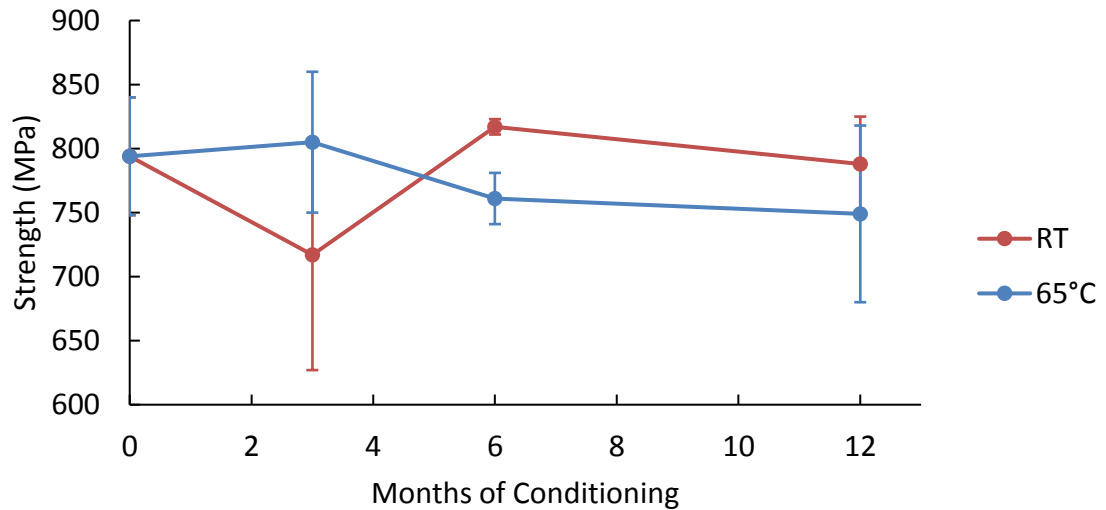


Figure 2-5: Plot of tensile strength vs. conditioning time in Arabian Gulf seawater of a unidirectional glass/epoxy composite (based on Mourad et al., 2010)

Mourad et al., (2010) also reported that elastic modulus initially increases, but begins to decline and after six months, specimens conditioned at room temperature encounter a 10% reduction. This reduction occurs due to plasticization of the matrix, which makes the polymer

matrix more ductile. After six months, the strain to failure was shown to increase compared to the unconditioned samples. The following increase in elastic modulus occurs due to the squeezing together of fibers and matrix due to hydrolysis swelling within the unidirectional composite. Similar trends can be seen in the elevated temperature conditioned samples except for the absence of an initial increase in modulus

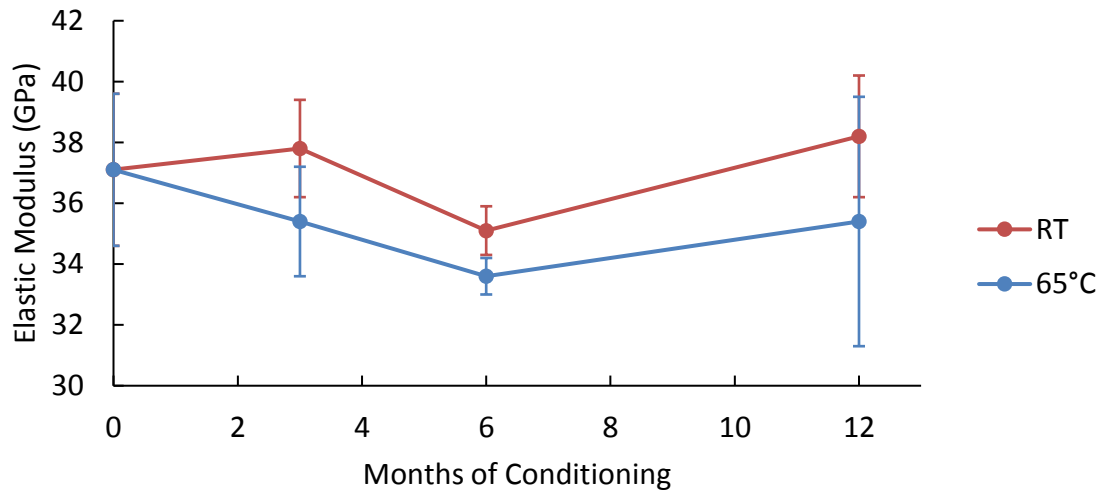


Figure 2-6: Plot of tensile elastic modulus vs. conditioning time of glass/epoxy composite (based on Mourad et al., 2010)

Mourad et al. (2010) further investigates the laminates using micrographs of fracture surfaces from samples that were unconditioned, room temperature conditioned after one year, and elevated temperature conditioned after one year. Unconditioned control samples displayed little evidence of fiber-matrix bond degradation with an absence of fiber pull-out and coarse surfaces near fiber-matrix contacts. These unconditioned samples show strong bonding between the fiber and matrix that leads to ductile failure in the glass fibers and brittle fracture of the surrounding epoxy. The micrograph of the room temperature conditioned sample showed coarse surfaces and fiber pull-out at the fiber-matrix interface. Some resin is still left on the failed fibers, which indicates the presence of a good fiber-matrix bond. Compared to control samples, slight

reductions in strength and slight increases in elastic modulus and failure strain were also reported. The elevated temperature conditioned sample's micrograph displayed fiber pull-out, but no resin remained on these failed fibers. The authors conclude that hydrolysis weakens the fiber-matrix interface in these samples prior to failure. Evidence of smooth fiber and coarse matrix surfaces suggests a more ductile matrix failure and a more brittle fiber failure, which are opposite failure mechanisms compared to the control samples. Strength reduced by 6%, while failure strain increased by 2% and elastic modulus increased by 10% in these elevated temperature conditioned samples.

Vauthier et al. (1998) also argued that matrix degradation shortened fatigue life. The authors described the effects of flaws created by absorbed water during fatigue in wet-conditioned unidirectional composites. Dynamic three-point bending at  $R=0.1$  and a frequency of 25 Hz was used for testing. As small cracks form, capillary action allows water to diffuse up the crack and accelerate crack propagation. Elevated temperatures of conditioning further increase the diffusion rate. Although fiber failure occurs more rapidly in conditioned samples, macroscopic damage, such as modulus loss, involves a higher failed-fiber density in conditioned samples compared to unconditioned samples. The reduction of fatigue life found in conditioned samples, however, was found to be caused by a combination of both matrix plasticization and hydrolyzed crack tip opening. In this study, the authors also invoked a statistical approach to connect distributed fiber failures to the reduction of composite properties. Through this analysis, specimens immersed in water were found to have a statistically greater number of fiber failures compared to samples conditioned in moist (50% relative humidity) environments. This data suggests that chemical reactions in both the matrix and fibers induced by absorbed water, such as leaching or hydrolysis, negatively affect the statistical distribution of fiber strength within the composite.

Weitsman (1995) also attested to the degradation of polymers by the fluid it is immersed in. Absorbed fluid in epoxy composites increases the creep rate in the polymer matrix for any given value of stress. The fluid can also attack the fiber-matrix interface through hydrolysis and chemically decay glass fibers through leeching. The author also stated that Grant (1991) found quasi-isotropic laminates to have less-severe losses in strength when immersed in water compared to losses in unidirectional glass/epoxy samples.

The sizing compound that surrounds the fibers protects the fibers during handling and manufacturing and prevents the buildup of static charge on the fiber. Most important for this study, the sizing compound also strengthens the fiber-matrix bond. Boisseau et al. (2013) mentioned the importance of fiber sizing when fatigue testing GFRPs in marine environments. The authors tested bending specimens manufactured with an available optimal sizing formulation and with two “non-optimal” sizing formulations developed for different types of manufacturing. Prior to loading, the specimens were conditioned at 60°C for 15 weeks until saturation. When fatigued in four-point bending while submerged in seawater, the optimal sizing specimens display decade-longer fatigue life than specimens with the non-optimal sizing. The authors imply that stress corrosion cracking at the fiber-matrix interface plays a major role in fatigue life of glass/epoxy composites.

From the extensive work in water-conditioned fatigue testing, it can be shown that the matrix, fiber-matrix interface, and fibers are all affected by wet conditioning. While in most cases, water absorption leads to a degradation of mechanical properties, in some short-term scenarios, water absorption can actually lead to an increase in mechanical properties. It is apparent that microscopy will play a key role in an investigation in the effects of wet conditioning on damage and failure mechanisms in glass/epoxy composites.

#### References:

- Abdel-Magid, B., Ziaee, S., Gass, K., & Schneider, M. (2005). The combined effects of load, moisture and temperature on the properties of e-glass/epoxy composites. *Composite Structures*, 71(3), 320-326.
- Boisseau, A., Davies, P., & Thiebaud, F. (2013). Fatigue behaviour of glass fibre reinforced composites for ocean energy conversion systems. *Applied Composite Materials*, 20(2), 145-155.
- Crank J, Park GS. Diffusion in polymers, New York: Academic Press, 1968.
- Davies, P., Mazeas, F., & Casari, P. (2001). Sea water aging of glass reinforced composites: shear behaviour and damage modelling. *Journal of Composite Materials*, 35(15), 1343-1372.
- Grant, T. S., (1991). "Seawater Degradation of Polymeric Composites," Texas A&M University, Master Thesis, May 1991.
- Jones, F. R. (2003). The Effects of Aggressive Environments on Long-Term Behavior. In B. Harris (Ed.), *Fatigue in Composites* (pp. 117-145). Cambridge: Woodhead Publishing Ltd.
- Kennedy, C. R. (2013). *Fatigue of Glass Fibre Composites in Marine Renewable Energy* (Doctoral dissertation).
- Ladevèze P, "On a damage mechanics approach," in *Mechanics and Mechanisms of Damage in Composites and Multimaterials*, ESIS 11, ed. D. Baptiste, MEP, London, 1991, p. 119.
- Mourad, A. H. I., Abdel-Magid, B. M., El-Maaddawy, T., & Grami, M. E. (2010). Effect of seawater and warm environment on glass/epoxy and glass/polyurethane composites. *Applied Composite Materials*, 17(5), 557-573.
- Pauchard, V., Grosjean, F., Campion-Boulharts, H., & Chateauinois, A. (2002). Application of a stress-corrosion-cracking model to an analysis of the durability of glass/epoxy composites in wet environments. *Composites Science and Technology*, 62(4), 493-498.
- Shen, C. H., & Springer, G. S. (1976). Moisture absorption and desorption of composite materials. *Journal of Composite Materials*, 10(1), 2-20.
- Vauthier, E., Abry, J. C., Bailliez, T., & Chateauinois, A. (1998). Interactions between hygrothermal ageing and fatigue damage in unidirectional glass/epoxy composites. *Composites Science and Technology*, 58(5), 687-692.
- Weitsman, Y. J. (1995). Effects of Fluids on Polymeric Composites-A Review (No. MAES-95-1.0). Tennessee University Knoxville Department of Mechanical and Aerospace Engineering.

## **Chapter 3**

### **Literature III: Textile Composite Damage Mechanics**

#### **Overview of Textile Composites**

As mentioned previously, tape laminates consist of several stacked layers of unidirectional plies. However, other manufacturing methods of composite laminates give rise to other types of composites with different behaviors. Laminates with relatively complex fiber architectures are known as textile composites due to their manufacturing. The three main types of textile composites include woven, stitched, and braided fiber architectures. As will be explained, textile composites offer a relatively inexpensive solution to manufacturing a PMC structure capable of operating in complex, multiaxial stress states such as hydrokinetic turbines. Moreover, textile composites also simplify manufacturing as many conformable layers can be laid up at once, as opposed to laying up each layer individually like a tape laminate.

Woven architectures involve undulating several parallel fibers tows over and under another set of parallel fibers. Different patterns such as plain, twill, and satin weaves are created based on the number of tows skipped before undulating. By nature, woven laminates have crimped or undulated fiber structures as shown in Figure 3-1. The weave innately holds the warp (undulated) and weft or fill (straight) fibers together. Also, the undulations in the weave produce some out-of-plane reinforcement such as the fibers shown in blue in Figure 3-1. However, the undulations cause reductions in in-plane strength and stiffness compared to traditional unidirectional laminates of the same matrix and fibers because the fibers do not solely provide in-plane reinforcement. Moreover, the crimps in the fabric are stress concentrating points that

especially affect fatigue loading. Stress cycles applied in-plane can cause the fibers to travel out of plane and cause matrix damage in the process (Vectorply 2016).

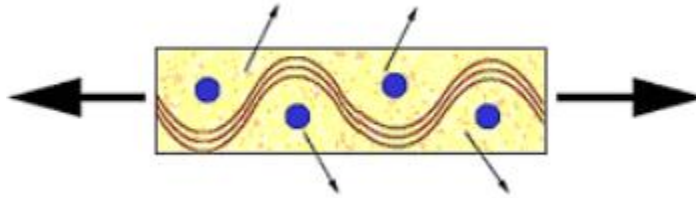


Figure 3-1. Illustrated cross section of a woven fiber-reinforced laminate showing movement of weft fibers during loading (Vectorply, 2016). *Permission granted by Vectorply.*

Figure 3-2 shows the structure of a quadaxial, tricot stitched laminate including a chopped strand mat. Not all stitched laminates include the chopped strand mat including the laminate used later in this study. Unidirectional, continuous fibers are laid down in layers and the stitch goes through the four layers to tie the fibers together. The advantages of stitch bonding include some out-of-plane reinforcement since the stitches run orthogonal to the fiber plane and a smooth surface since the stitches do not produce an undulated texture in the resin. Additionally, the mechanical connection of the tape layers through stitching provides many benefits, especially when loaded in compression (Cox & Flanagan, 1997). Stitched laminates are also relatively inexpensive in comparison to other multi-axial composite laminates (Vectorply, 2016).

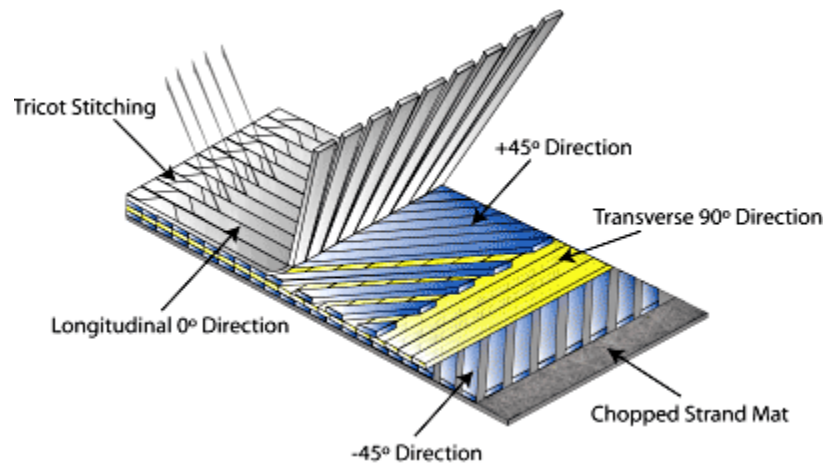


Figure 3-2: Illustration of a multi-axial tricot-stitched laminate including a mat (Vectorply 2016). *Permission granted by Vectorply.*

### **Review of Tape Laminate Composite Fatigue Damage & Failure**

In testing unidirectional plies, Kennedy (2013) identified three separate regions of mechanical response to fatigue prevail. A plot of these regions would look similar to the plot of modulus reduction shown previously in Figure 2-4. Region I is an area of high stress where the specimen typically fails in less than a thousand cycles. In region I, the failure mechanism is comparable to failure in quasi-static testing where fiber failure initiates almost immediately. Fibers fail randomly throughout the gauge section forcing neighboring fibers to carry higher loads until final failure occurs. In region II, moderate stresses lead to non-catastrophic transverse matrix cracks. The matrix cracks spread from the specimen edges inwards and occasionally encounter fibers. These inward-bound cracks either navigate around fibers or occasionally go through the fibers. As fatigue cycling continues, a damage network develops as cracks propagate and coalesce until the composite is weakened to the point of failure. In region III, the stresses are low enough that even after high cycle counts, few minor cracks develop and the material is below its fatigue endurance limit.

Kennedy further determined that, in quasi-isotropic layups, the matrix cracks typically found in regions II and III occur in transverse ( $90^\circ$ ) plies first. Again, these cracks form on the specimen's edges and work their way inwards. Similar to transverse plies,  $45^\circ$  plies may also accumulate matrix cracks. Delamination often follows shortly after the formation of cracks in  $45^\circ$  plies. If the load is high enough, cracks parallel to the load direction may form in  $0^\circ$  plies. These cracks, however, are not common in regions II and III. A majority of these matrix cracks form and propagate during the first quarter of the specimen's fatigue life. The remaining 75% of the specimen's fatigue life sees relatively little decrease in elastic modulus after the initial drop. The damage leading to failure in the remaining 75% of fatigue life involves matrix and fiber cracks in the  $0^\circ$  plies. Throughout the life of the specimen, strength degrades steadily when testing in constant amplitude fatigue. Promising models have shown a linear relationship between residual strength and number of cycles. Stiffness has been shown to decline in an S-shaped manner as opposed to linear with maximum stiffness reductions between 10-20% if plotted on a log-scale.

### **Overview of Textile Composite Damage & Failure**

There are several contributing factors to the failure of textile composites. While some out-of-plane reinforcement exists in both 2D woven and stitched laminates, both are considered quasi-laminar, and in being quasi-laminar, behave similar to common tape laminates and can be evaluated using classical laminated plate theory with some modifications. In fact, numerous studies compare a stitched or woven laminate to a tape laminate containing the same plies and the same layup sequence. These laminates will be referred to as similar or comparable tape laminates in this paper. The modifications to the classical laminated plate theory may include proportional reductions in stiffness or strength due to fiber misalignments within the fiber architecture. Stitching has been shown to increase the damage tolerance of composites due to the out of plane

reinforcement provided by the stitches (Cox & Flanagan, 1997). These stitches may penetrate fiber bundles and break or damage fibers. To minimize damage, manufacturers prefer to stitch the composite before the fibers are impregnated with resin. Resin tends to build-up on the stitching needle, which increases the effective needle size and subsequently increases the area of stitching-induced damage. The resin also prevents fibers from bending around the needle. Crimping is the term associated with fibers bending or otherwise geometrically distorting nearby a stitch (Mouritz & Cox, 2010).

### Quasi-Static Tension

When in tension, a load applied to textile composites is primarily distributed throughout the fibers aligned with the loading direction. Compared to a similar tape ply laminate, however, stitched laminates tend to exhibit lower tensile strength (Cox & Flanagan, 1997). This decline in tensile modulus can be attributed to the misalignment of in-plane fibers aligned with the loading direction. Fibers may be misaligned due to manufacturing error or due to distortions caused by stitching, such as crimping. The decline can be quantified using Equation 5, given by Piggott (1980), if the composite's original tensile moduli, shear modulus, and Poisson's ratio as well as the angle of misalignment,  $\phi$ , are known.

$$E(\phi) = \left\{ \frac{\cos^4 \phi}{E_1} + \frac{\sin^4 \phi}{E_2} + \frac{1}{4} \left( G_{12} - \frac{2\nu_{12}}{E_1} \right) \sin^2 \phi \right\}^{-1} \quad (5)$$

Conversely, stitching, especially in a VARTM manufactured composite, has been shown to increase a composite's tensile modulus by increasing fiber volume fraction via compaction (Khan & Mouritz, 1996). Increases in elastic modulus due to compaction, however, should not be expected to exceed 10%. Various stitch densities (distance between stitches) have resulted in no more than a 20% change in elastic modulus compared to a similar stacked laminate. Thus, no

statistically significant conclusion can be drawn regarding the connection between stitch density and elastic modulus. Similarly, stitch diameter and elastic modulus appear to be unrelated as well. Reductions in elastic modulus have also been noted to not be attributed to broken fibers or the presence of small regions of high matrix content. It should be noted that since there are a number of factors that can affect elastic modulus in textile composites, it can be difficult to pinpoint the effects of one factor as its effects may fall within the data noise (Mouritz & Cox, 2010).

Similar comments made for tensile modulus can be made for tensile strength in stitched composites, as no more than a 20% change in tensile strength compared to a similar stacked laminate has been shown. Fiber defects such as crimps and other misalignments as well as fiber breakages during manufacturing contribute to strength reductions of stitched laminates in comparison to similar tape laminates. As a consequence of the defects, plastic deformation of the matrix will occur in regions of high shear stress surrounding the misaligned fibers (Mouritz et al., 1997). Less information is available regarding increases in tensile strength compared to the more thorough studies of elastic modulus, but compaction is considered the most probable explanation for increases in tensile strength (Mouritz & Cox, 2010).

Unlike stitched laminates, fiber tows in 2D weaves have been found to rupture at loads around 30-50% lower than in aligned, unwoven fiber bundles. This reduction in fiber strength may be caused by damage to fibers during textile manufacturing, undulations causing lengthwise stiffness variations, fiber misalignment, and lateral loads caused by orthogonally adjacent fibers (Cox & Flanagan, 1997). Curtis and Bishop (1984) found that woven laminates tested in the fill direction suffered a 15-25% reduction in tensile strength compared to comparable tape laminates.

## Quasi-Static Compression

Stitched composites with more than 0.04 stitches/mm<sup>2</sup> have a reduction in compression strength compared to similar tape laminates (Mouritz & Cox, 2010). This reduction equates to nearly 10-20% and can best be explained by a kink band dominated failure, as kink bands develop more readily in fibers misaligned with the loading direction. Immediately following the formation of a few kink bands, a stitched specimen fails under catastrophic buckling. Since Euler buckling does not play a major role until final failure, internal energy is not released through delamination cracks under in-plane loading. Thus, stitched composites can be evaluated using a modified plate theory that incorporates stitches as Winkler foundations that bridge delamination (Mouritz & Cox, 2000). Delamination has been noted to not be a major source of damage in stitched specimens since the stitches offer delamination resistance. This gives stitch-bonded composites an advantage over woven composites in compression (Cox & Flanagan, 1997). On the contrary, stitched composites with a stitch content of less than 0.04 stitches/mm<sup>2</sup> have been shown to have an advantage in compressive strength over comparable tape laminates. At lower stitch densities, less misalignments occur because less stitches are present. Apparently, until a certain critical stitch density, the benefits of delamination resistance due to stitches can outweigh the reduction of strength resulting from fiber misalignments caused by stitching (Mouritz & Cox, 2010).

Since only a few kink bands form before failure, stitched laminates are far more brittle than woven laminates and are more prone to catastrophic failure (Cox et al., 1994). This brittle failure mechanism makes compressive strength predictions fairly simple since the critical axial compressive stress,  $\sigma_c$ , can be based off of the maximum shear stress of the matrix,  $\tau_m$ , and the maximum angle of misalignment of aligned fibers (measured in radians),  $\phi$ , as shown in Equation 6 (Argon, 1972).

$$\sigma_c = \frac{\tau_m}{\phi} \quad (6)$$

Although undulations are not generally present in stitched composites, fiber misalignments do form where stitches are present. As previously established, either the stitching needle or simply the area of local compaction caused by the stitch yarn cause these fiber misalignments, which have been noted to be the main factor for reductions in compressive strength and fatigue life (Mouritz & Cox, 2000). Furthermore, Farley (1992) suggests that kink band failure caused by misalignments tend to be closer to the composite's surface since fibers closer to the surface tend to be mostly affected by stitching. However, compressive failure has also been noted near the surface of unstitched composites as well since there is little support at the free edge. Reeder (1995) found longitudinal fibers in stitched composites that were offset  $8.5^\circ$  near stitching sites. Similarly, Mouritz and Cox (2000) showed that the maximum distortion angle may even be as high as  $20^\circ$ , with a high distribution of fibers offset between  $5^\circ$  and  $15^\circ$ .

Besides fiber misalignment, stitching may also lead to resin micro cracks, resin-rich or void-rich areas, and damaged or broken fibers. Despite the threat internal composite damage poses to the integrity of the matrix, the compaction of the composite caused by stitching raises the volume fraction of fibers, which subsequently increases the composite's compressive elastic modulus (Mouritz & Cox, 2000).

Unlike stitched composites, 2D weaves do contain undulations, and different weave patterns have varying levels of undulation. Studies have shown that quasi-isotropic laminates made from 2D satin weave have lower tensile strength than comparable tape laminates. In compression, 2D weaves generally accumulate damage through delamination cracks and sites of plastic shear flow within the matrix near future kink band sites. Delamination in woven composites occurs both between plies and between fiber bundles within a ply. Due to the amplitude of undulations, load bearing fibers tend to be misaligned with the loading direction,

which promotes kink banding. When this kink banding initiates, delamination failure occurs rapidly (Cox & Flanagan, 1997).

### **Tension-Tension Fatigue**

Compared to the amount of literature surrounding quasi-static testing and damage mechanisms for stitched composites, there is significantly less information regarding fatigue, especially for tension-tension fatigue. A majority of studies report that stitches decrease the fatigue performance of laminates. Unfortunately, most fatigue studies did not report how fatigue damage initiates and propagates throughout the sample, or how stitch density or stitch diameter affects fatigue life (Mouritz & Cox, 2010). Khan and Mouritz (1996) showed that the S-N curve of stitched composites tend not to have a slope that is consistent with that of a comparable tape laminate. This difference implies that there is a difference in tensile fatigue damage mechanisms between the two types of laminates. Furthermore, stitches separating from the matrix in fatigue hasten damage accumulation within the stitched samples.

Cox et al. (1994) mentions that in tension-tension fatigue, tensile matrix cracks (i.e. cracks perpendicular to the loading direction) develop faster than in compression-compression fatigue. The quantity of micro-sized matrix cracks increases as more cycles are accumulated. These cracks may even form in loads within the linear-elastic region of quasi-static test data. By forming, the cracks decrease the stiffness of the specimen slightly. The tension-tension specimens eventually fail due to tensile failure of fiber tows, but the connection between the matrix cracks and the final-tow failure have not been shown to be necessarily related. The tow failure, however, usually occurs where fibers are misaligned with the loading direction.

## Compression-Compression Fatigue

Numerous studies regarding the effects of out-of-plane reinforcements, including stitches, show that compressive fatigue life and fatigue strength decrease compared to similar tape laminates due to these reinforcements. Unlike tension-tension fatigue, the slope of the tape laminates' and stitched laminates' compression-compression S-N curves are nearly the same, which implies both types of laminates have similar damage mechanisms (Mouritz & Cox, 2010).

Similar to quasi-static compression behavior, kink-banding is a dominant contributor to damage caused by cyclic loading. Again, the magnitude of misalignment of fibers that are supposed to be aligned with the loading direction considerably affects fatigue life. Under cyclic loading, fibers may even twist slightly, causing local shearing around the fiber before the fiber kinks. If this mechanism of failure is accurate, a modified Paris Law equation can be used to quantify damage within a sample so long as some material constants can be calculated using previous data. Equation 7 displays the modified Paris Law that incorporates resin shear stress,  $\tau_C$ , stress amplitude,  $\Delta\sigma_s$ , material constants  $A$  and  $m$ , the number of cycles,  $N$ , and the misalignment angle (measured in radians),  $\phi$ .

$$\frac{d\tau_C}{dN} = -A(\Delta\sigma_s\phi)^m \quad (7)$$

If the fatigue tests are completed using load control, only a few kink bands develop prior to failure. In fact, stitched specimens have been shown to immediately fail following the formation of the first kink band (Cox & Flanagan, 1997).

If the shear stress of the matrix is known, then the critical number of cycles until kink band formation occurs can be calculated using Equation 8 (Cox & Flanagan, 1997).

$$N_k = \frac{\tau_C - \Delta\sigma_s\phi}{A(\Delta\sigma_s\phi)^m} + 1 \quad (8)$$

3D woven samples, which differ from 2D woven samples in that they have fibers woven through the entire thickness of the laminate, have been shown to produce significant matrix cracking in quasi-static compression, but almost no matrix cracks form during fatigue. These few matrix cracks occur near kinking aligned fibers. Under cyclic loading, the matrix inside aligned fiber bundles accrues damage and less fibers carry the compressive load. Contrary to stitched composites, woven composites are more damage resistant and accrue damage throughout the entire specimen (Cox et al., 1994).

### **Thermoplastic Stitches**

The aforementioned literature regarding stitching technology involved the use of glass fiber, carbon fiber, or Kevlar stitches, which has comprised the majority of stitched composite laminates for the past three decades. However, thermoplastic stitches have accumulated interest within the past ten years due to their ability to soften. During the cure cycle of the composite manufacturing process, the soluble stitches soften or melt, decreasing fiber misalignment caused by the initial stitching process that compromises the mechanical properties of the composite in both quasi-static and fatigue loading. Polyamide yarns, including nylon, have been shown to produce statistically superior or equal modulus and strength in both tension and compression when compared to a non-stitched reference tape laminate. Prior to testing, the stitched composite was cured at 180 °C with a two hour hold time (Beier et al., 2008). In addition to minimizing the presence of distorted fibers, the softened thermoplastic addition can toughen the composite through a host of mechanisms. These mechanisms, whose adjacent parenthetical numbers correspond to labels in Figure 3-3, include crack pinning (1), particle bridging (2), and crack path deflection (3), localized shear yielding (4), and micro cracking (5) (Meister, 2000) (Zhang,

2003). Thus, thermoplastic stitches appear to outperform traditional non-softening stitching fibers and may lead to more failure-resistant parts in the future.

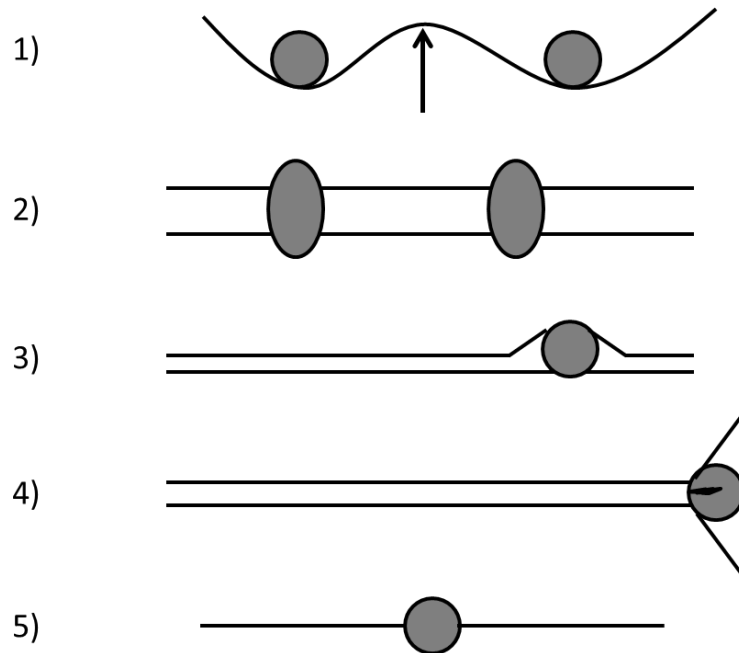


Figure 3-3: Diagram illustrating toughening mechanisms within thermoplastic-toughened epoxies (based on Meister, 2000)

## References

- Argon, A.S. (1972). Fracture of composites. *Treatise of Materials Science and Technology*, Vol. 1, Academic Press, New York.
- Beier, U., Wolff-Fabris, F., Fischer, F., Sandler, J. K., Altstädt, V., Hülder, G., Schmachtenburg, E., Spanner, H., Weimer, C., Roser, T., & Buchs, W. (2008). Mechanical performance of carbon fibre-reinforced composites based on preforms stitched with innovative low-melting temperature and matrix soluble thermoplastic yarns. *Composites Part A: Applied Science and Manufacturing*, 39(9), 1572-1581.
- Chang, P., Mouritz, A. P., & Cox, B. N. (2006). Properties and failure mechanisms of pinned composite lap joints in monotonic and cyclic tension. *Composites Science and Technology*, 66(13), 2163-2176.
- Cox, B. N., & Flanagan, G. (1997). Handbook of analytical methods for textile composites. NASA Contractor Report 4750. NASA Langley Research Center. Hampton, Virginia.
- Cox, B. N., Carter, W. C., Dadkhah, M. S., & Morris, W. L. (1994). Micromechanics of fatigue in woven and stitched composites. NASA Contractor Report 4626. NASA Langley Research Center. Hampton, Virginia.
- Curtis, P. T., & Bishop, S. M. (1984). An assessment of the potential of woven carbon fibre-reinforced plastics for high performance applications. *Composites*, 15(4), 259-265.
- Farley, G. L. (1992). A mechanism responsible for reducing compression strength of through-the-thickness reinforced composite material. *Journal of Composite Materials*, 26(12), 1784-1795.
- Kennedy, C. R. (2013). *Fatigue of Glass Fibre Composites in Marine Renewable Energy* (Doctoral dissertation).
- Khan, M. S., & Mouritz, A. P. (1996). Fatigue behaviour of stitched GRP laminates. *Composites Science and Technology*, 56(6), 695-701.
- Meister, J. (2000). Polymer modification: principles, techniques, and applications. CRC Press.
- Mouritz, A. P., & Cox, B. N. (2000). A mechanistic approach to the properties of stitched laminates. *Composites Part A: Applied Science and Manufacturing*, 31(1), 1-27.
- Mouritz, A. P., & Cox, B. N. (2010). A mechanistic interpretation of the comparative in-plane mechanical properties of 3D woven, stitched and pinned composites. *Composites Part A: Applied Science and Manufacturing*, 41(6), 709-728.
- Mouritz, A. P., Leong, K. H., & Herszberg, I. (1997). A review of the effect of stitching on the in-plane mechanical properties of fibre-reinforced polymer composites. *Composites Part A: Applied Science and Manufacturing*, 28(12), 979-991.
- Piggott, MR. (1980) Load bearing fiber composites. *Oxford: Pergamon Press*, (74).
- Reeder, J. R. (1995). Stitching vs. a toughened matrix: compression strength effects. *Journal of Composite Materials*, 29(18), 2464-2487.
- Stitch-Bonded Reinforcements - Vectorply. (n.d.). Retrieved November 10, 2016, from <http://Vectorply.com/stitch-bonded-reinforcements/>
- Zhang, M. (2003). A review of the epoxy resin toughening. Syracuse University, New York.

## **Chapter 4**

### **Research Opportunities and Objectives**

#### **Research Opportunity**

Most of the literature concerning glass/epoxy composites immersed in water focuses on unidirectional or crossply laminates. Many of these studies utilize tape laminates and involve three or four point bending as opposed to traditional dogbone samples. Thus, there is inadequate information regarding the effects of fatigue loading on textile glass/epoxy composites used in a marine environment. Understanding the fatigue behavior of immersed glass/epoxy composites could inspire low-cost and durable marine structures such as hydrokinetic turbine blades.

There is also little information regarding the effect of varying the maximum stress of high-cycle fatigue loading in immersed conditions on quasi-isotropic glass/epoxy laminates. If different damage mechanisms are apparent, then there is academic interest in defining the difference's cause.

Damaged and failed specimen microscopy in the literature is mostly limited to images of failed fibers imaged using scanning electron microscopy (SEM). SEM is usually expensive since polymers require a metal coating to improve conductance and machine/staff time adds up. Few publications report micrographs of damage within immersed and fatigues composites, while fewer publications show an image containing more than a dozen glass fibers in the micrograph that is usually in an unmarked, local region of the fracture surface. Therefore, there is opportunity to investigate full cross sections of damaged and failed fatigue samples to investigate the mechanisms that degrade composite mechanical properties during immersion and fatigue testing.

## Research Objectives and Tasks

The objective of this research is to characterize and compare the quasi-static and T-T fatigue behaviors of stitch-bonded and woven roving laminates in unconditioned and marine environments. The objectives are met by the following tasks.

- *Manufacture quasi-isotropic stitch-bonded and woven E-glass/epoxy laminates using the out-of-autoclave (OOA) vacuum-assisted resin transfer molding (VARTM) method.* OOA signifies that the manufacturing process did not require immense pressure applied by an autoclave during curing to achieve acceptable void contents. OOA composites typically reduce the cost of manufacturing compared to traditional autoclave prepregs because an autoclave is not required. Quasi-isotropic composite laminates were selected for investigation since quasi-isotropic laminates are often used in structures undergoing multi-axial loading such as hydrokinetic turbine blades. The stitch-bonded system is of greatest interest since it has been chosen by ARL for future use in hydrokinetic turbine blades. The woven system, which contains the same matrix as the stitch-bonded system, serves as a means of evaluating the effects of fiber architecture on mechanical response.
- *Test specimens in quasi-static tension and T-T fatigue.* Tensile loading spectra are of main interest in the design of hydrokinetic blades. Two testing regimens were used: Wet & Elevated Temperature (WET) and Room Temperature Ambient (RTA). WET testing, which refers to elevated temperature conditioning in artificial seawater for two weeks and subsequent testing in room-temperature distilled water, is intended to simulate the marine environment of hydrokinetic blades. Initial (baseline) quasi-static tensile modulus and strength, T-T S-N behavior, and residual quasi-static tensile strength after selected modulus changes were obtained. Stress levels corresponding to fatigue lifetimes of approximately ten million cycles were determined. The suitability of classical laminated plate analysis for

predicting the tensile modulus and quasi-static strength of the stitch-bonded and woven laminates was evaluated.

- *Analyze post-fatigue specimens.* Damage in specimens cycled to failure and in specimens cycled partially to failure was analyzed using surface scanning and microscopic imaging of polished cross-sections.

## **Chapter 5**

### **Experimental Procedures**

#### **Specimen Manufacturing**

##### **Woven Roving WRE581T/ST94 Panels**

The material system WRE581T/ST94 consists of Gurit WRE581T woven roving E-glass fibers and Gurit ST94 epoxy resin. WRE581T comes as a 2x2 twill weave and has a balanced quantity of warp and weave fibers. WRE581T/ST94 has a cured ply thickness of about 0.018 in. and has a fabric weight of roughly 581 gsm or 17 oz/yd<sup>2</sup>, which makes each layer about 8.5 oz/yd<sup>2</sup>. ST94 is an epoxy resin that is used in prepreg OOA manufacturing. Gurit states that ST94 tends to resist micro-crack growth and has a wide range of cure temperatures from 85°C to 120°C (Russell, 2016). In the WRE581T/ST94 system, ST94 is attached to the fibers as a tacky backing that seeps through the fibers during curing.

A quasi-isotropic layup was desired and thus the WRE581T/ST94 is cut into four [0°/90°] squares and four [±45°] squares. Each square was cut from the same roll using a common 24 in. x 24 in. aluminum plate as a guide. The aluminum plate was rotated 45° to cut the [±45°] squares. The squares are then laid up into a [0°/90°/±45°]<sub>2s</sub> laminate by creating two identical 8-ply stacks and flipping them over at the mid-plane to consolidate the full, 16-ply composite panel. It should be noted that there is an epoxy-epoxy bond at the mid-plane where back-to-back adhesion occurs. Figure 5-1 shows the prepreg sheets prior to layup.

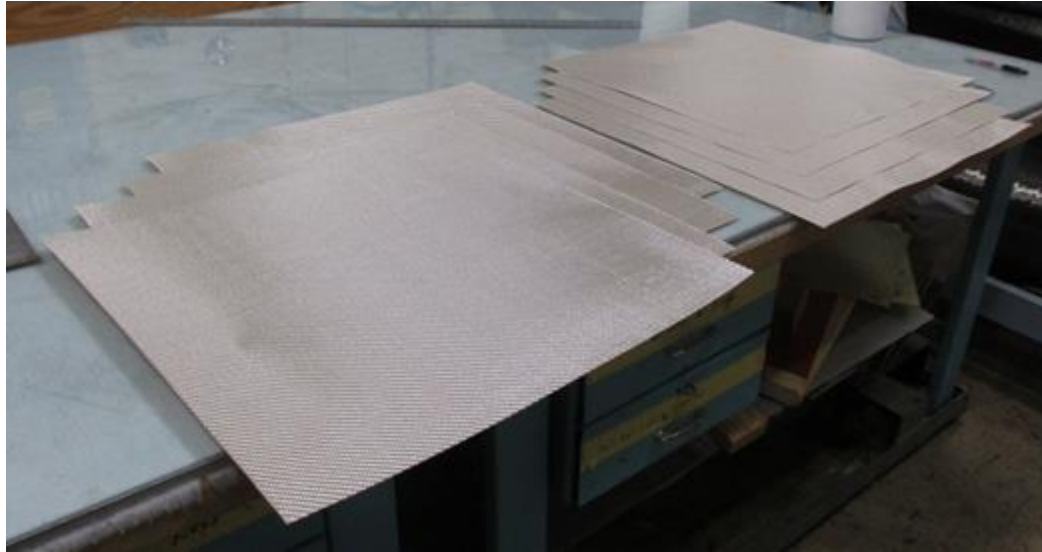


Figure 5-1. Four  $[0^\circ/90^\circ]$  and four  $[\pm 45^\circ]$  plies of WRE581T/ST94 twill weave prepreg awaiting hand layup

Once the plies were stacked correctly, the following manufacturing layup was utilized (listed from bottom to top): aluminum tool, non-porous Teflon, porous Teflon, 16-ply laminate, porous Teflon, perforated release film, porous Teflon, and a vacuum bag. The flat aluminum tool was equipped with a built-in vacuum-hose adapter port. The top side of the adaptor port is covered with scrap cloth of woven glass fiber to impede excess resin from entering the vacuum port. The excess glass fiber cloth is shown on the lower right-hand corner of Figure 5-2. Sealant tape was applied around the perimeter of the tool and a vacuum bag was placed over the tool. Vacuum was applied via a vacuum pump that was initially closed a few times to check for leaks.

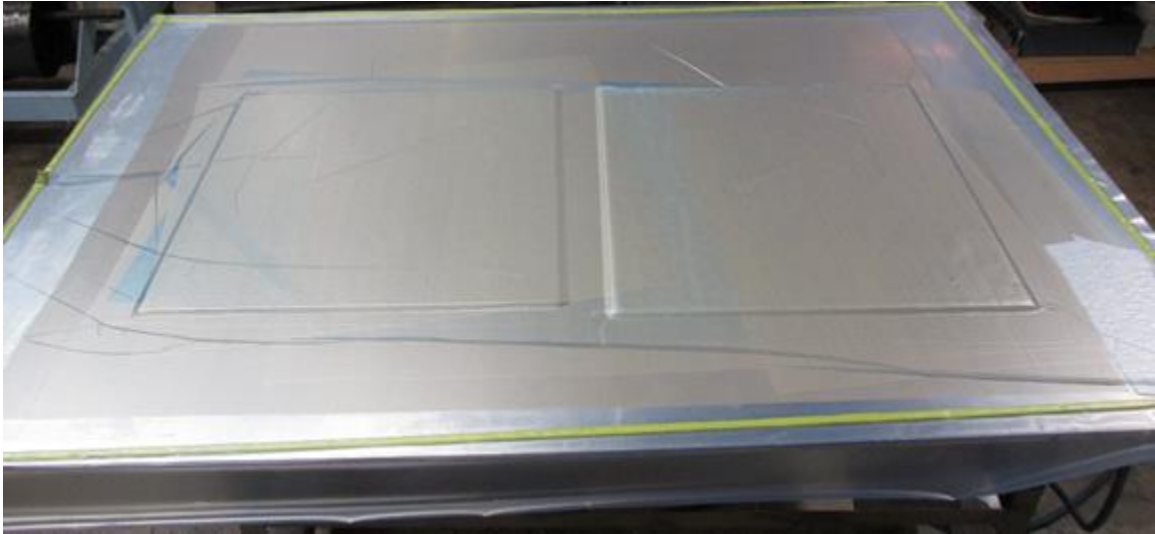


Figure 5-2. Woven and stitched laminates under vacuum bag before insertion into oven

Once all leaks were mitigated, the tool was inserted into an oven with vacuum constantly being applied. The oven curing cycle is illustrated in Figure 5-3. Changes in temperature are denoted as dashed lines because the oven used did not have programmable ramp capabilities. After curing and cooling, the samples were de-bagged and sent to ARL's machine shop to be cut into dogbone samples.

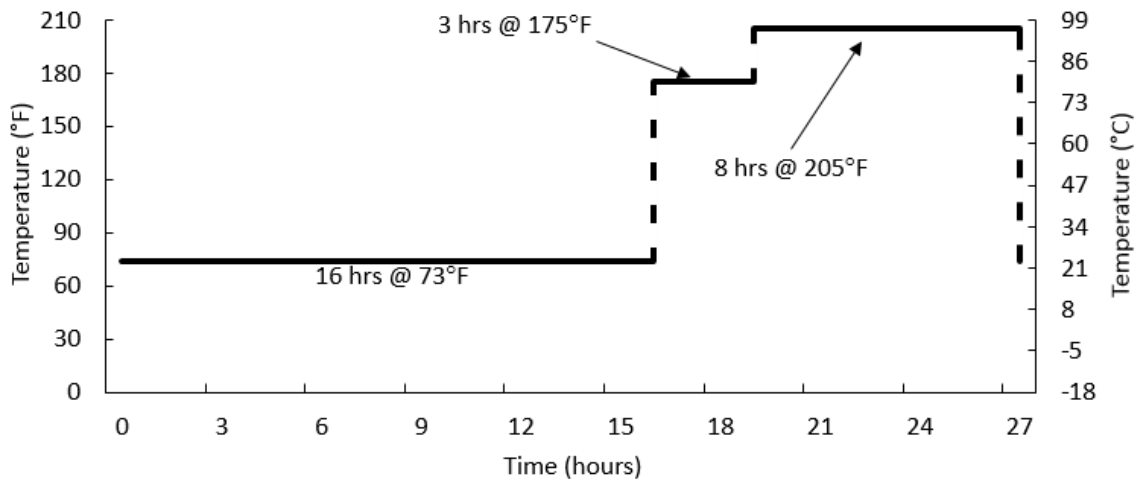


Figure 5-3. Diagram of oven curing cycle for WRE581T/ST94 and QE1203/ST94 panels

### **Stitch-Bonded QE1203/ST94 Panels**

The material system QE1203/ST94 consists of Vectorply QE1203 fibers and Gurit ST94 epoxy resin. QE1203 is named after its quadaxial fiber pattern involving E-glass fibers with a fabric weight of 1203 gsm or roughly 35 oz/yd<sup>2</sup>, which makes each of the four constituent plies approximately 8.7 oz/yd<sup>2</sup>. The QE1203/ST94 laminate had a cured ply thickness of approximately 0.039 in.

While the exact same layup was desired for the QE1203/ST94 stitch-bonded panel, creating a  $[0^\circ/90^\circ/\pm 45^\circ]_{2s}$  laminate was not possible since the stitch-bond material was manufactured as a quadaxial  $[0/+45/90/-45]$  design. Thermoplastic polyester stitches in a tricot pattern held the quadaxial fiber tows together. An illustration of tricot stitching was displayed previously in Figure 3-2 and a comparison photograph of the twill weave and tricot stitching patterns of either laminate are shown in Figure 5-4. Again, the prepreg comes attached as a tacky film at the bottom of the quadaxial fiber pattern ( $[0/+45/90/-45/(\text{resin film})]$ ). Table 5-1 summarizes the laminate properties relevant to manufacturing.

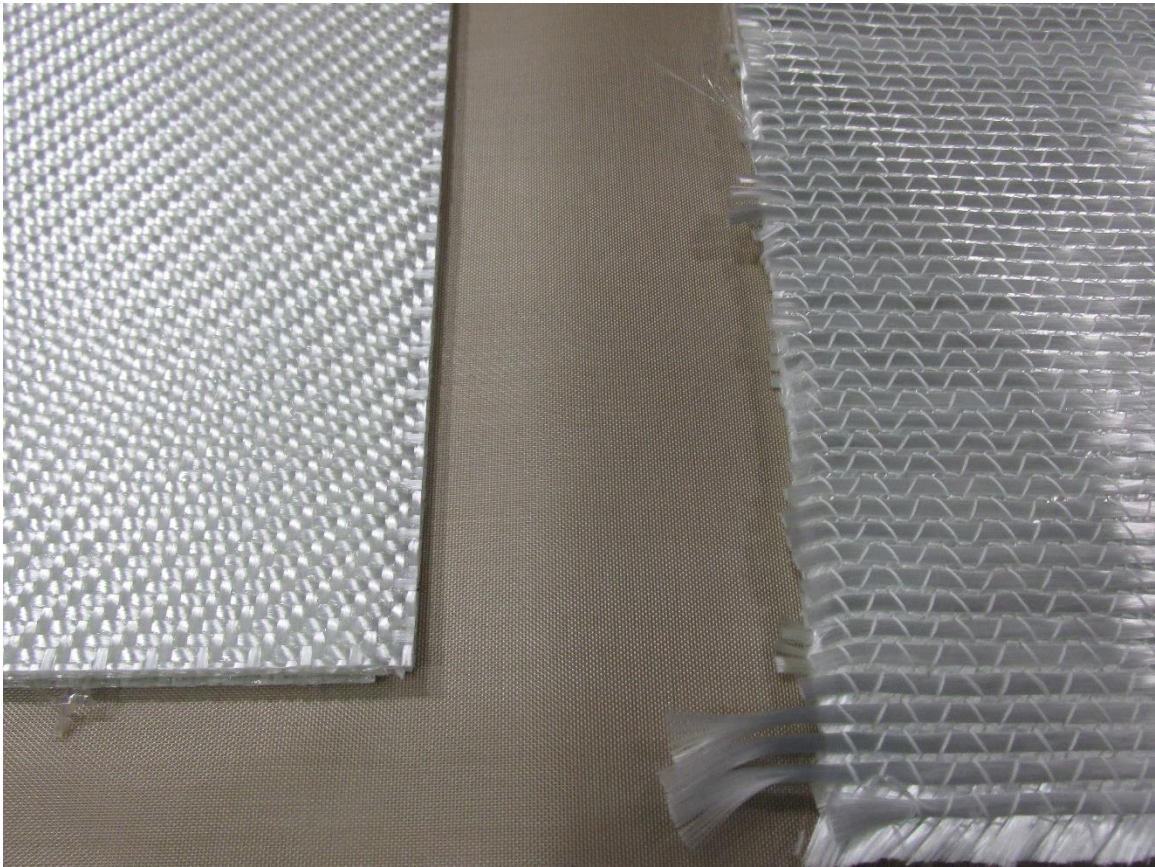


Figure 5-4. Photograph of woven (left) and stitched (right) laminate pre-cured surfaces

Table 5-1. Summary of laminate manufacturing and textile properties

	WRE581T/ST94	QE1203/ST94
Fiber Architecture	2x2 Twill Weave	Quadaxial Tricot-Stitched
Panel Stacking Sequence	$[0^\circ/90^\circ/\pm 45^\circ]_{2s}$	$[(0^\circ/45^\circ/90^\circ/-45^\circ)_2/(45^\circ/90^\circ/-45^\circ/0^\circ)_2]$
Cured Ply Thickness	0.457 mm (0.018 in.) for $[0^\circ/90^\circ]$	0.991 mm (0.039 in.) for $[0^\circ/45^\circ/90^\circ/-45^\circ]$
Fiber Weight	581 gsm (17.1 oz./yd <sup>2</sup> ) for $[0^\circ/45^\circ/90^\circ/-45^\circ]$	1203 gsm (35.5 oz/yd <sup>2</sup> ) for $[0^\circ/90^\circ]$

## Dogbone Specimen Machining

Dogbone specimens were cut using a diamond-blade bandsaw in ARL's machine shop. The edges of the samples were then polished with a 6 in. diameter aluminum oxide grinding wheel with a rotation rate of 3600 rpm to create a smooth finish. The dimensions of the specimens followed a modified ASTM D638 Type III dogbone geometry. ASTM's D638 standard was created for mechanical testing of plastics (ASTM, 2017). The modification was made in the grip area where one inch in length was removed from each of the two grip sections. The dimensions of the modified D638 Type III dogbone specimen used is displayed in Figure 5-5. Once the specimens were cut, each specimen's gauge-section width and thickness were recorded for stress calculations. A technician used calipers to take several measurements of the width and thickness of the dogbone specimens and recorded the mean value of these measurements.

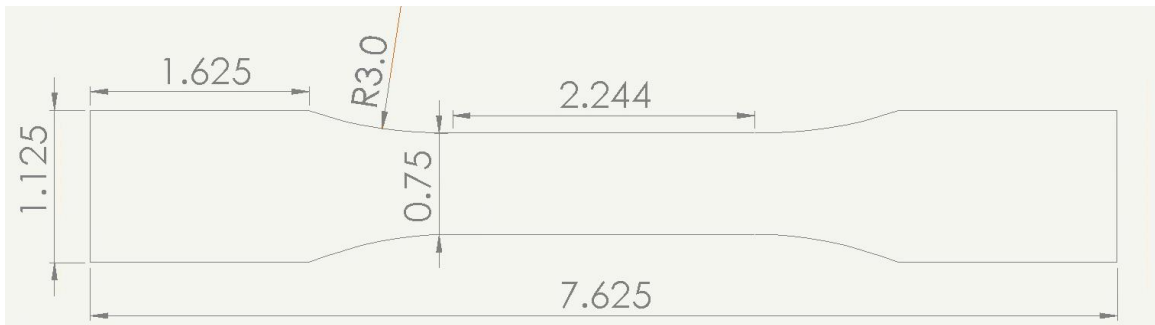


Figure 5-5. Drawing of modified ASTM D638 Type III dogbone specimen used in testing program, dimensions in inches (ASTM, 2017)

## WET Conditioning

Conditioning of dogbone specimens utilized ASTM D1141, section 6 saltwater formula (ASTM, 2017). The acronym WET is used to denote Wet, Elevated Temperature testing. WET testing, as it is described for this project, involves the elevated temperature conditioning of a

sample followed by mechanical fatigue testing with the specimen submerged in room temperature distilled water. WET testing differs from ETW testing since ETW implies loading at an elevated temperature, rather than WET's immersion at elevated temperature and loading at room temperature. ASTM D1141 was initially developed to mimic seawater for corrosion testing of marine structures. The composition of ASTM D1141 is depicted in Figure 5-6. In this study, composite specimens were immersed in the artificial seawater to track water uptake and to measure the effects of water absorption in a simulated saline environment. Prior to conditioning, the specimens were kept in a sealed plastic bag for two months before they were weighed to record their pre-conditioning dry mass. The artificial seawater and the specimens were placed in Tupperware™ containers with stiff, buoyant nets placed between the specimens so that the specimens did not lie on top of one another. The lid was then sealed and placed in a temperature controlled oven held at a constant  $160\pm 3^{\circ}\text{F}$  for fourteen days. Following the two-week conditioning period, the specimens were removed from the heated water, dried using chemical tissues (Kimwipes™) and allowed to stand on-edge for 30 minutes to allow any remaining surface water to evaporate. The air-dry setup is shown in Figure 5-7. The specimens were then wiped a second time before being weighed to record post-conditioning wet mass. Due to the length of the samples and the size of the scale available, specimens had to be weighed using binder clips to stand the specimen upright. The mass of the binder clips was first measured alone and zeroed. Then, the clips were attached to the bottom of the specimen and the clips and specimen were weighed together. Figure 5-8 displays the weighing procedure including the upright dogbone specimen.

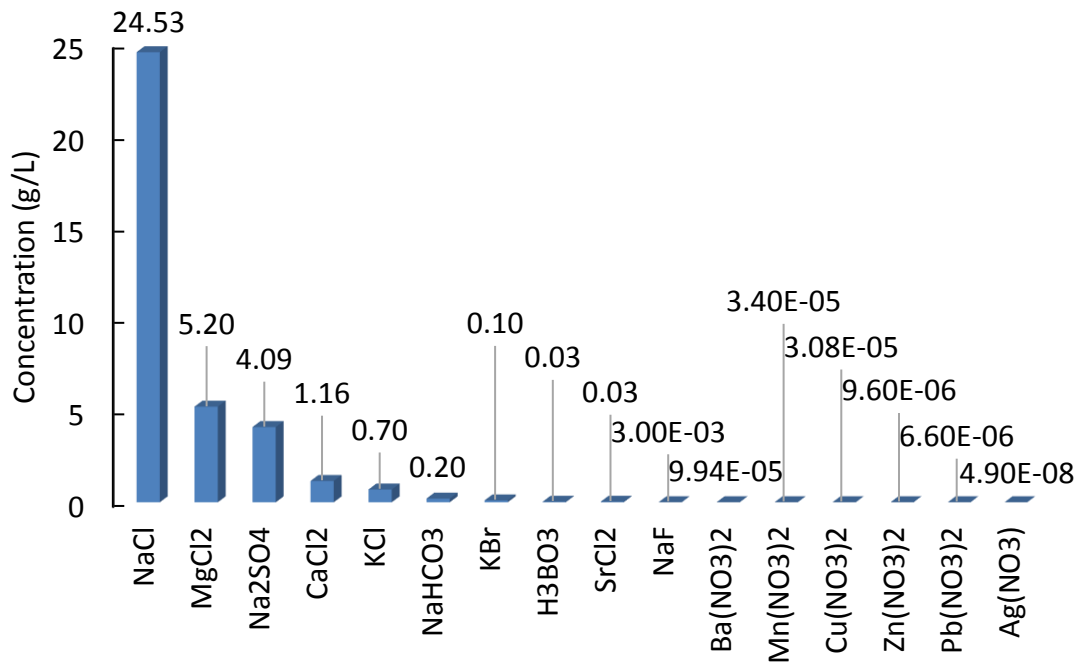


Figure 5-6. Bar chart depicting concentrations of compounds in ASTM D114 artificial seawater (ASTM, 2003)

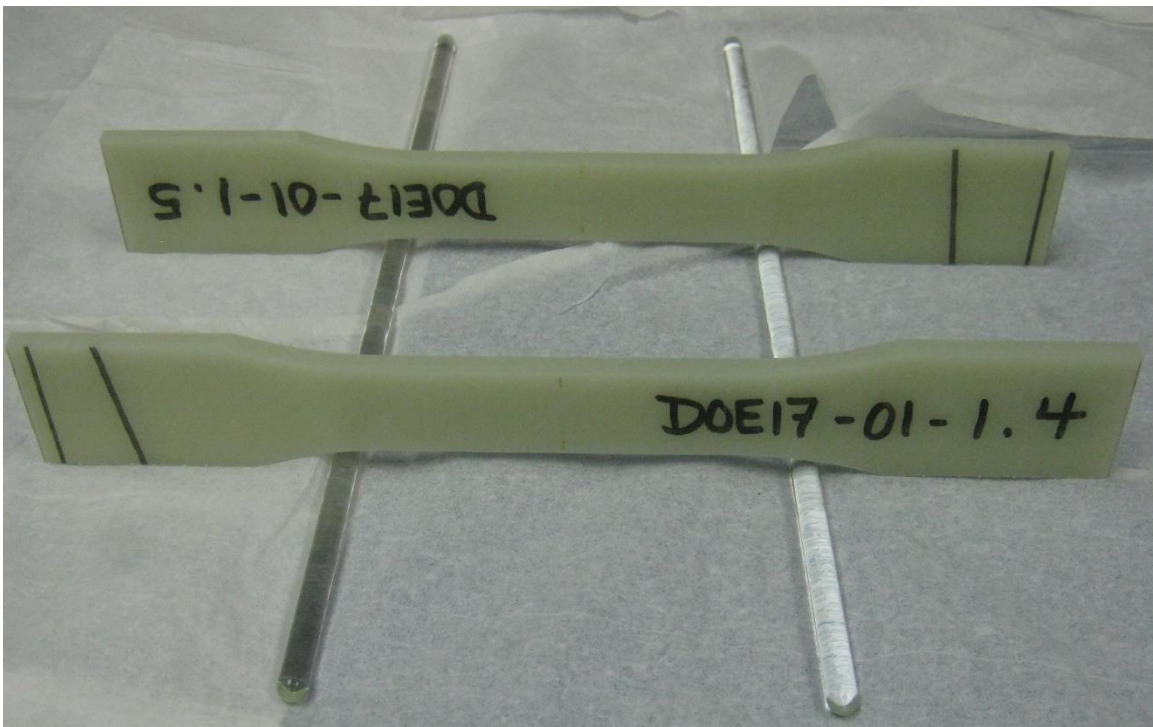


Figure 5-7. WET specimens during air-dry period prior to weight measurement



Figure 5-8. Dogbone specimen weight measurement procedure including binder clips

After conditioned specimens were weighed, Teflon tape was applied over the bagged and tool sides of each dogbone and polysulfide was applied onto the edges to ensure water-induced microcracking would not occur in the composite during immersed fatigue testing. Although edge-microcracks are a major issue for composites in marine environments, most marine-composite structure edges are protected by a coating, sealant, or secondary structure. Thus, to accurately test the composite's behavior for its application in a marine structure, the polysulfide was used to seal the edge. The Teflon tape was applied in order to keep moisture from escaping from the composite after conditioning. The tape would be removed prior to testing. 3M™ Aerospace

Sealant AC-350 Class B was used due to its bond strength and relatively quick cure. The sealant was packaged as a two-part mix including a base and a catalyst with correct stoichiometric ratios. Once the two parts are mixed and sufficiently stirred, the mixture was inserted into an empty plastic syringe and slowly deposited around the perimeter of each sample. Once an even layer of sealant was applied around the entire perimeter, the specimens were left to dry using binder clips to hold the specimens off the ground. Completed specimens were flipped every five minutes to ensure the sealant on the bottom of the specimen was not dripping. After 30 minutes of flipping, the specimens were left out overnight to cure. The next morning, specimens were placed in room temperature distilled water until they were chosen for fatigue testing when the tape would be removed and the sealant would be trimmed with a razor blade to be flush with the tool/bagged sides.

Several samples were dried and weighed twice a day for two weeks so that water uptake could be measured and plotted over the full fourteen-day conditioning period. These samples were removed from the oven and left to dry for 30 minutes before the specimens were wiped with Kimwipes™ and weighed. The conditioning water was also left out of the oven for 30 minutes during this time and only placed back into the oven once the specimens had been weighed and re-immersed. This was done to fit the water uptake curve to a Fickian-based model to predict water uptake beyond the two-week conditioning period. The same procedure for drying and weighing the specimens was used as the procedure for the other conditioned samples with one exception. Since the specimens were put back in the oven several times, the seawater container was also left out of the oven during the 20-minute air-drying period as to not cause thermal shock by placing cooled specimens in heated water. The container was covered during this time to prevent the evaporation of the simulated seawater.

## **Fiber Volume and Void Volume Measurements**

### **ASTM 2584-11 Burnoff**

The ASTM 2584-11 test method was followed to measure void volume and fiber volume fraction in the various composite samples (ASTM, 2011). The burnoff procedure began with washing six ceramic crucibles with soap and tap water before they were left to dry overnight. Once dry, remaining dust or other particles were air-blown with a pressurized pneumatic hose. The empty crucibles were then weighed and their empty mass was recorded. Next, composite specimens were placed into the crucibles and the combined composite/crucible mass was recorded to find the dry composite weight. The crucibles were labelled on the bottom so that specimens could be later identified. Next, the scale was modified to include a bridge setup for measuring the immersed weight of the composite. The bridge held a container of distilled water above the scale, while a pole attached to the scale's measuring mechanism hung above the container. The pole held a metal-mesh basket that was lowered into the water without touching the edges of the surrounding container. Each sample was individually lowered into the container and its immersed mass was recorded. The temperature of the water was also recorded for later density calculations. After immersed mass measurements, the specimens were placed back in their respective crucibles, lids were placed over the crucibles, and the crucibles were placed side-by-side in a small oven designated for burnout. The samples underwent the heating procedure laid out in Figure 5-9.

Figure 5-9. Burnoff heating procedure including times and temperatures of holds

Once the samples completed the temperature cycles, they were held at 250°F until a user turned the oven off. Once the oven was off, the crucibles were removed from the oven and placed in a glass desiccator to cool down to room temperature. After two hours of cooling, the crucible

lids were removed and each crucible was weighed again. After burnoff, only the tows of the E-glass fibers remained, as shown in Figure 5-10. Equations 9 through 13 list the calculations necessary to calculate fiber volume and void volume percentages.

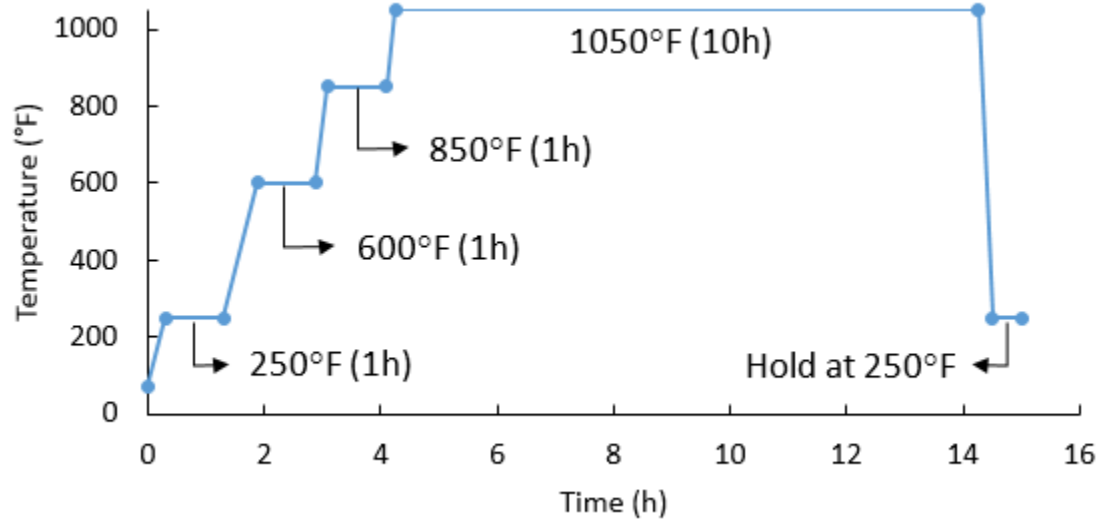


Figure 5-9. Burnoff heating procedure including times and temperatures of holds

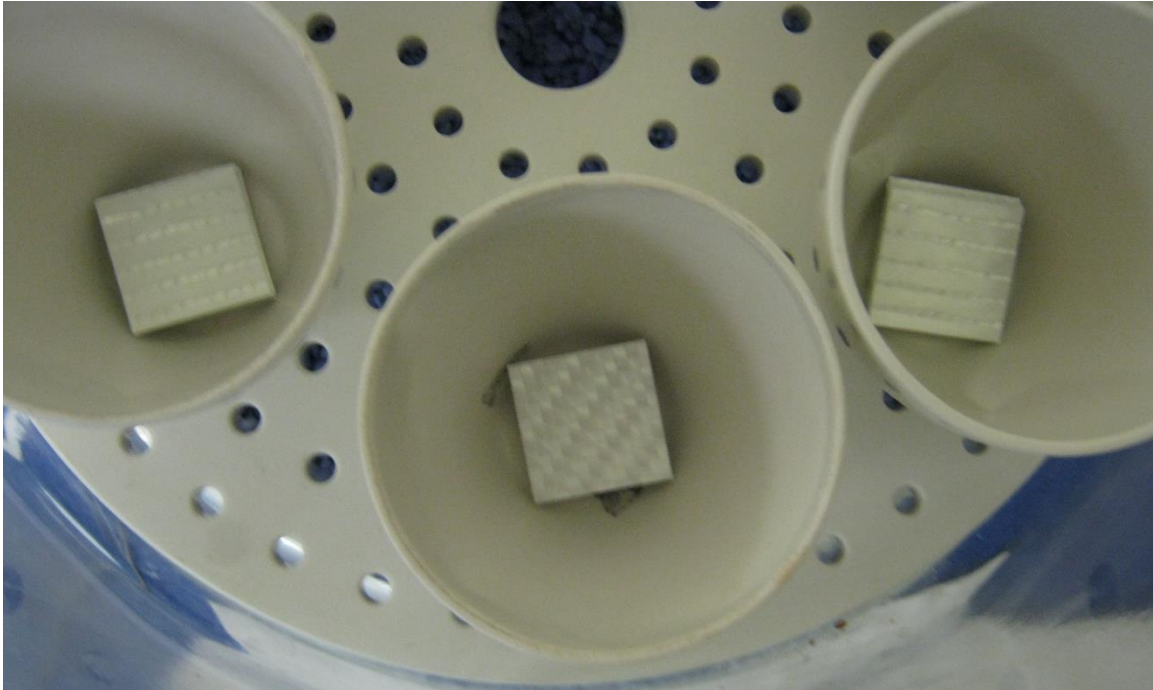


Figure 5-10. Remnants of burnoff procedure with woven sample (middle) and stitched samples (left & right)

$$\rho_c = \frac{m_{dry}}{m_{dry} - m_{wet}} \rho_{H_2O} \quad (9)$$

$$wt\%_{fiber} = \frac{m_{crucible+fiber} - m_{crucible}}{m_{dry}} * 100 \quad (10)$$

$$wt\%_{resin} = \frac{m_{dry} - (m_{crucible+fiber} - m_{crucible})}{m_{dry}} * 100 \quad (11)$$

$$Vol\%_{fiber} = \frac{\frac{(m_{crucible+fiber} - m_{crucible})}{\rho_{fiber}}}{\frac{m_{dry}}{\rho_c}} \quad (12)$$

$$Vol\%_{void} = 100 - \rho_c \left( \frac{wt\%_{resin}}{\rho_{resin}} + \frac{wt\%_{fiber}}{\rho_{fiber}} \right) \quad (13)$$

These equations utilize the following parameters: composite dry mass,  $m_{dry}$ , composite density,  $\rho_c$ , submerged composite mass,  $m_{wet}$ , fiber weight percentage,  $wt\%_{fiber}$ , resin weight

percentage,  $wt\%_{resin}$ , crucible and fiber combined mass,  $m_{crucible+fiber}$ , empty crucible mass,  $m_{crucible}$ , resin density,  $\rho_{resin}$ , fiber density,  $\rho_{fiber}$ , water density,  $\rho_{H_2O}$ , fiber volume percentage/fraction,  $Vol\%_{fiber}$ , void volume percentage/fraction,  $Vol\%_{void}$ . Fiber density was found previously through helium pycnometry experiments run by ARL and resin density was provided by the manufacturer (Juska, 2016).

### **Microscopy Void Volume Approximation**

(See Sectioning, Polishing, and Microscopy: Microscopy)

## **Quasi-Static Testing & Modeling**

### **Baseline Axial Laminate Tensile Modulus & Strength Testing**

Several room-temperature ambient (RTA) specimens and WET specimens were tested in quasi-static tension and compression in order to develop a baseline for mechanical properties. For simple laminate baseline testing, an unreported number of warps-parallel plies of WRE581T/ST94 were stacked and six aligned QE1203/ST94  $[0^\circ/+45^\circ/90^\circ/-45^\circ]$  plies for baseline RTA and WET testing. The initial woven roving WRE581T/ST94 data comes from unpublished data collected by the Mississippi Polymer Institute that was provided by Dr. Thomas Juska of ARL (Juska, 2016). The initial stitch-bonded QE1203/ST94 comes from unpublished ARL data (Strauch, 2016). The woven roving tensile samples were tested under ASTM D3039 while the stitch bonded laminate was tested using the modified ASTM D638 Type III mentioned earlier (ASTM, 2014) (ASTM, 2017). Shear woven roving samples were tested as ASTM D5379 v-notch samples (ASTM, 2013). While  $E_1$  ( $0^\circ$  direction),  $E_2$  ( $90^\circ$  direction), and  $G_{12}$  were

provided for the woven roving material, only  $E_l$  was available for the stitch-bonded material.

Tensile strengths in the  $0^\circ$  direction are also provided for both laminates.

### **Baseline Sun/Li Model and Ply Discount Model**

Sun & Li (1988) discusses the Sun/Li model, which is used to predict 3D laminate properties based on several input parameters necessary for calculations. The Sun/Li model relies on in-plane isostrain and out-of-plane isostress assumptions and assumes plies are a rectangular prism like a tape-laminate. The model was used in an attempt to test whether the quasi-laminar assumption mentioned in the literature could be used for the stitch-bonded and woven roving material system. To break the material systems into plies, the woven roving material was analyzed as laminated  $0^\circ$  and  $90^\circ$  plies with equal thicknesses and the quadaxial stitch-bonded laminate was analyzed as separate  $0^\circ$ ,  $+45^\circ$ ,  $90^\circ$ ,  $-45^\circ$  plies, again with equal thicknesses across each ply. If the predicted value from the model fell within the statistical error of measured results, the assumption would at least be deemed plausible for future use in more complex structural models.

Since individual ply properties were not known and could not be measured easily, they were approximated using the Halpin-Tsai model (Ashton et al., 1969). Equations 14 through 20 display the Halpin-Tsai model used to calculate  $E_1$ ,  $E_2$ ,  $G_{12}$ , and  $\nu_{12}$  of each laminate. Inputs for fiber and matrix properties are shown in Table 5-2.

$$\xi_t = 2, \quad \xi_s = 1.5 \quad (14)$$

$$\eta_t = \frac{E_{2f} - E_m}{E_{2f} + \xi_t * E_m} \quad (15)$$

$$\eta_s = \frac{G_{12f} - G_m}{G_{12f} + \xi_s * G_m} \quad (16)$$

$$E_1 = V_f E_{1f} + (1 - V_f) E_m \quad (17)$$

$$E_2 = E_m * \frac{1 + \xi_t \eta_t V_f}{1 - \eta_t V_f} \quad (18)$$

$$G_{12} = G_m * \frac{1 + \xi_s \eta_s V_f}{1 - \eta_s V_f} \quad (19)$$

$$\nu_{12} = \nu_f V_f + \nu_m (1 - V_f) \quad (20)$$

Table 5-2. Input composite properties for Halpin-Tsai/Sun-Li models using properties for E-glass and known ST94 resin elastic modulus

Fiber Volume Fraction ( $V_f$ )	0.4 to 0.65
Fiber-Direction Elastic Modulus of Fiber ( $E_{1f}$ )	73 GPa <sup>[1]</sup>
Transverse-Direction Elastic Modulus of Fiber ( $E_{2f}$ )	73 GPa <sup>[1]</sup>
Shear Modulus of Fiber ( $G_{12f}$ )	30 GPa <sup>[1]</sup>
Poisson Ratio of Fiber ( $\nu_{12f}$ )	0.28 <sup>[1]</sup>
Elastic Modulus of Matrix ( $E_m$ )	3.4e9 <sup>[2]</sup>
Poisson Ratio of Matrix ( $\nu_m$ )	0.35 <sup>[1]</sup>

Daniel & Ishai (2006)<sup>[1]</sup>  
Russell (2016)<sup>[2]</sup>

Once the ply properties are calculated, the Sun-Li model requires laminate properties in the third dimension. Since there was no data available for either material system, an assumption of transverse isotropy was made. For a composite material, this means that mechanical properties are identical in planes orthogonal to the fiber direction. Using the assumption of transverse isotropy as well as an assumed  $\nu_{23}$  of 0.4 and using the isotropic material assumption to find  $G_{23}$ , the full 6x6 stiffness matrix of each composite ply can be created. The Sun-Li model then takes these three-dimensional ply properties and a user-input layup and outputs three-dimensional laminate properties. The model was transferred into MATLAB and the code is displayed in Appendix A. The code then takes input measured properties and

compares the values by displaying the predicted and measured value along with the percent error.

Strength predictions were also made using the ply properties calculated from the Halpin-Tsai model. These ply properties were input into MATLAB code, which determines ply stresses in a pre-determined direction. In this case, the loading was aligned with the  $0^\circ$  fibers on the outer surfaces of both the woven and stitched laminates. The ply stresses are determined using calculations that include an applied stress value and laminate stiffness/compliance matrices. Using these tools, total in-plane laminate strains can be calculated under an isostrain assumption. Ply strains can then be calculated from the overall laminate strain and ply stresses can be calculated using the ply strains. Residual stresses due to curing or temperature change was not included in the model. Once the ply stresses are calculated, the Tsai-Wu method for predicting failure was utilized. The Tsai-Wu method is an interactive failure model that incorporates axial and transverse tension and compression as well as shear strengths of laminates to determine when plies fail. When the Tsai-Wu number becomes greater than 1, there is an indication of tensile/compressive failure or shear failure. Ply strength values used for the Tsai-Wu method were taken from textbook values listed for a unidirectional E-glass/epoxy tape laminate. These values are shown in Table 5-3. The textbook E-glass laminate was stated to have a fiber volume fraction of 0.55. The ply discount method can be used to determine tensile strength of a composite by increasing stress (input into the code as  $N_x$ , or load normalized by the specimen width) until a ply reaches a Tsai-Wu number of 1. When this occurs, the ply's  $E_2$  and  $G_{12}$  are reduced by 75% of their initially determined values (from the Halpin-Tsai equations) to simulate damage in the matrix of that ply. Load is then increased until another ply reaches a Tsai-Wu number of 1. If a ply reaches a Tsai-Wu number of 1 for the second time, even after having its  $E_2$  and  $G_{12}$  discounted, the  $E_2$  and  $G_{12}$  are decreased to practically zero for that ply. Final failure

occurs when the 0° plies encounter a Tsai-Wu number of 1, which is usually when the stress in the 0° plies reach the longitudinal laminate failure strength.

Table 5-3. Textbook values for ply strengths used in Tsai-Wu portion of the ply discount strength model (Daniel & Ishai, 2006)

Ply Strength Description	Symbol	Strength (MPa)	Strength (ksi)
Longitudinal Tensile Strength	$F_{1t}$	1140	165
Transverse Tensile Strength	$F_{2t}$	39	5.7
In-Plane Shear Strength	$F_6$	89	12.9
Longitudinal Compressive Strength	$F_{1c}$	620	90
Transverse Compressive Strength	$F_{2c}$	128	18.6

### Pre-fatigue Modulus

Pre-fatigue modulus was not measured for samples destined for fatigue to failure. However, in the case of a majority of samples, fatigue loading was stopped prior to failure to acquire damaged specimens. Therefore, individual baseline pre-fatigue modulus measurements were required to quantify each sample's percentage loss in modulus. The reasoning and procedure for acquiring damaged samples is discussed in the next sections.

In order to measure baseline elastic modulus values ten baseline modulus measurements were recorded for every specimen tested excluding those tested to failure. Each test utilized an INSTRON 8511 servo-hydraulic testing machine with a 0.05 in./min displacement ramp rate. The full procedure for aligning and gripping the sample is explained in the RTA T-T Fatigue section. An extensometer was attached to the samples via rubber bands and strain was measured. The extensometer was calibrated using a 1in. precision calibration block and a 0.004 in. (or 4 mil)

block. The extensometer was zeroed using the 1in. block and was deemed calibrated if, when the 4-mil block was added, the extensometer measured  $\pm 1\%$  of 4 mils. The full baseline modulus test setup is shown in Figure 5-11. The loading was applied until a maximum load, usually around 900 lbf, equating to a strain slightly higher than  $2,660 \mu\epsilon$  was reached when the sample was then unloaded via a preset, maximum-load interlock. The hydraulic top grips were opened and re-closed after each modulus measurement. Elastic modulus was calculated using a chord modulus from  $0 \mu\epsilon$  to  $2,660 \mu\epsilon$ , as required by a previously determined ARL standard (Koudela, 2016). The ten modulus measurements were recorded using Instron's FastTrack® data acquisition software and the mean and standard deviation of the elastic modulus as well as the load corresponding to  $2,660 \mu\epsilon$  were calculated in a spreadsheet. The computer connected to the Instron testing machine via an IEEE 488 connector cable.

Oftentimes, the first modulus data point was found to be an outlier in the modulus data due to the extensometer slipping into place. If the outlier was removed from the data set, the mean and standard deviation were recalculated using the other nine data points. If the outlier was more than four standard deviations away from the mean of the other nine data points, then the outlier was removed from the data and an eleventh modulus measurement was recorded and substituted for the outlier. Outliers were found to occur in nearly half of the samples tested.

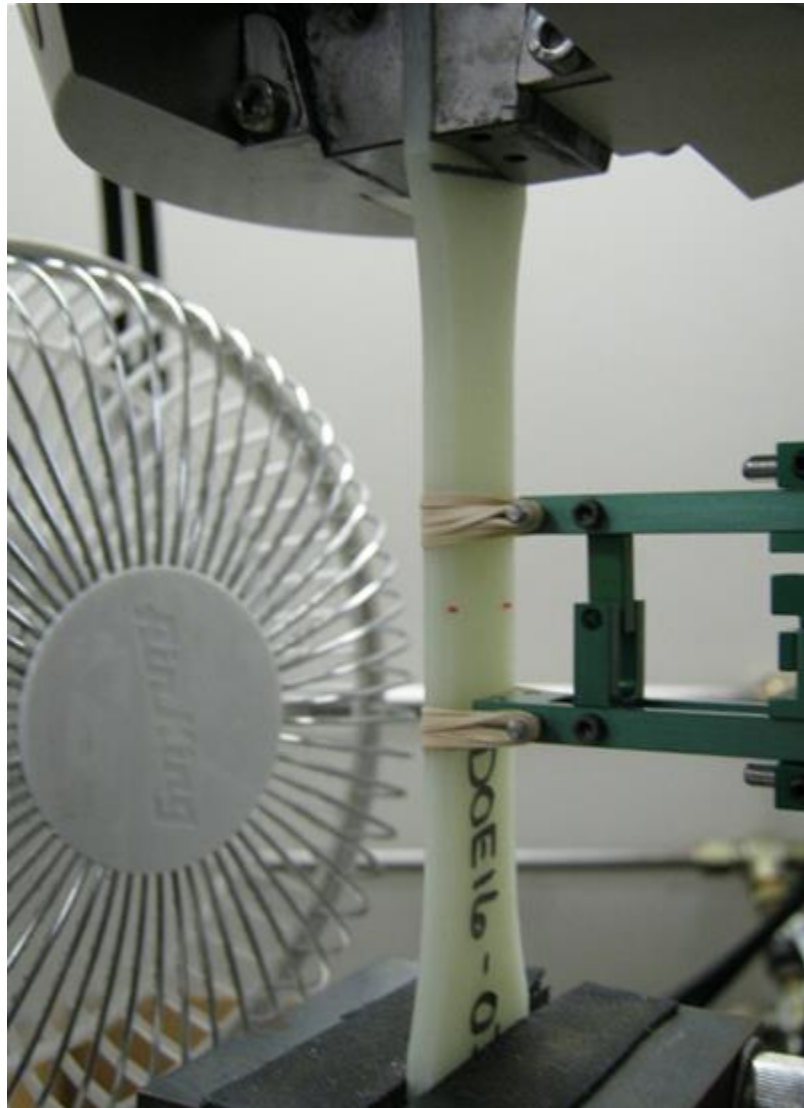


Figure 5-11. Hydraulic grip, specimen block, extensometer, and specimen during pre-fatigue modulus testing

### **Tension-Tension (T-T) Fatigue Testing**

There were two main objectives of fatigue testing, both of which were aimed at comparing the WRE581T/ST94 and QE1203/ST94 material systems as well as comparing their fatigue data with previously tested ARL material systems. The first goal was to develop an S-N curve to compare fatigue failure mechanisms. In many cases, if the S-N plot of the two material

systems' S-N curves have the same shape, they fail in similar mechanisms. Differences in S-N curve shapes, such as quick or steady declines, can provide hints into a material's fatigue failure mechanism. To establish an S-N curve, maximum fatigue stresses of 28.75, 22, and 18 ksi were chosen with an  $R$  ratio of 0.1 to compare these material systems with PAC, a commonly used naval composite material system (Koudela, 2016). Interlocks were set to prevent the testing machine from completely separating the failed specimen so that post-failure microscopy could be performed. At least two samples of each material system were fatigued to these three stress levels. This test plan was identical for both RTA and WET testing.

The second goal of testing was to investigate damage mechanisms in the material systems. To accumulate damage, specimens were fatigued at maximum loads of 18 and 13.75 ksi at  $R=0.1$  and a frequency of 10 Hz. 18 ksi was chosen to compare damage data to failure data since this maximum load was also used in fatigue failure testing. 13.75 ksi was chosen because initial results showed that samples fatigued at this maximum load achieved 16% modulus reduction after approximately ten million cycles, which is the service life goal of the hydrokinetic turbines. These specimens acquired damage until a pre-determined reduction in elastic modulus was reached. Prior ARL testing showed that residual strength tended to drop-off around a reduction of elastic modulus of 10-15% (Koudela, 2016). To generate data for comparison to prior ARL fatigue testing of other material systems, elastic modulus reductions of 10%, 13%, and 16% were targeted in this study. Three specimens of both material systems were fatigued to these three values: two for residual strength and one for microscopy. Again, this test plan was repeated identically for both RTA and WET samples. The full test plan for both RTA and WET testing is displayed in Table 5-4, although, it should be noted that WET woven testing was not performed.

Table 5-4. RTA & WET test plan (note: WET testing was not performed on Woven samples)

<b>RTA &amp; WET TEST PLAN</b>	<b>QE1203/ST94 (Stitch-Bond)</b>	<b>WRE581T/ST94 (Woven Roving)</b>
<i>Fatigue-to-Failure, R=0.1, f=10 Hz</i>		
28.75 ksi maximum – To failure	#1 #2	#1 #2
22 ksi maximum – To failure	MIC#1 #2	MIC#1 #2
18 ksi maximum – To failure	MIC#1 #2	MIC#1 #2
<i>Fatigue-to-Damage (Pre-Failure), R=0.1, f=10 Hz</i>		
18 ksi maximum – 10% Modulus Red.	RS#1 RS#2 MIC#1	RS#1 RS#2 MIC#1
18 ksi maximum – 13% Modulus Red.	RS#1 RS#2 MIC#1	RS#1 RS#2 MIC#1
18 ksi maximum – 16% Modulus Red.	RS#1 RS#2 MIC#1	RS#1 RS#2 MIC#1
13.75 ksi maximum – 10% Modulus Red.	RS#1 RS#2 MIC#1	RS#1 RS#2 MIC#1
13.75 ksi maximum – 13% Modulus Red.	RS#1 RS#2 MIC#1	RS#1 RS#2 MIC#1
13.75 ksi maximum – 16% Modulus Red.	RS#1 RS#2 MIC#1	RS#1 RS#2 MIC#1
Key: RS = Residual Strength, MIC = Microscopy		

### **RTA T-T Fatigue Testing**

The test setup for RTA T-T fatigue testing is shown in Figure 5-12 and was identical to the setup for baseline modulus measurements excluding the cooling fans. First, the specimen was placed into the stainless steel block grip at the bottom of the test fixture. The specimen was aligned with the middle of the top grip and leveled using the edge of the gauge length and a t-shaped bubble level. The top grips were slightly narrower than the specimen’s grip section, so an equal amount of the specimen appeared on both sides of the grip if aligned correctly. Once level, the four bolts on the block grip are torqued to 25 in-lbf. The top grip was then closed. If one of the top grip faces was closer to the specimen than the other (causing a slight bend in the

specimen), then six bolts (not shown in Figure 5-12) on a platform below the specimen block could be loosened and the specimen block/circular plate/platform assembly could be translated by tapping the specimen block with a small mallet.

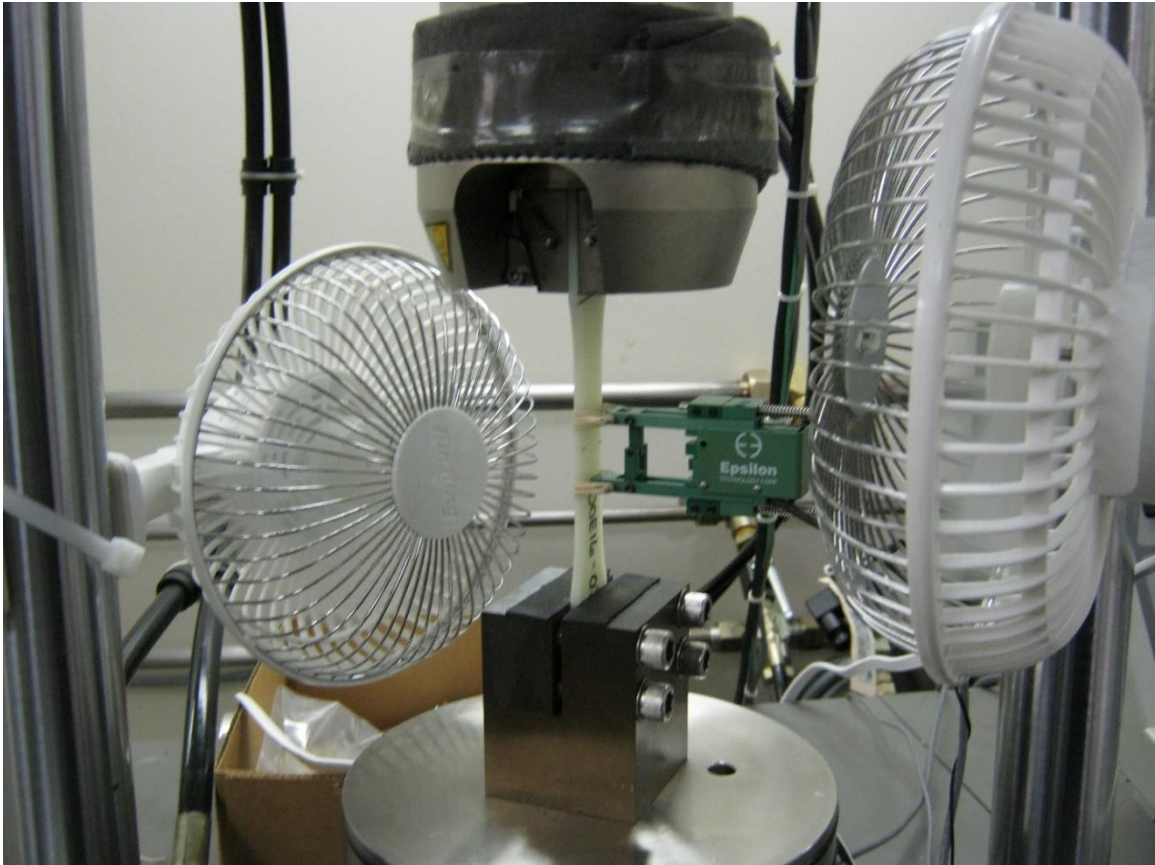


Figure 5-12. RTA T-T fatigue setup with hydraulic grips, extensometer, specimen, and cooling fans

Once the specimen was correctly aligned, the six bolts would be torqued to 50 in-lbf and the top grip would be closed. When closing the top grip, a load control setting with a maximum of 15 lbf was applied to keep the gripping process from applying more than  $\pm 15$  lbf to the specimen. With both grips closed, the load was slowly raised to its predetermined mean load in position control using a set point dial on the user control panel. Once the load neared the mean load, the machine was switched into load control and the load was set to the exact mean load. Next, the predetermined load amplitude was input into the user control panel and the loading cycle was

input as a sinusoid at 10 Hz. A maximum load interlock was set at 100 lbf above the maximum load and a minimum load interlock was set at exactly 90 lbf for every test to assure the correct loading was applied and to prevent damage to the machine in case of premature failure. Cooling fans attached to the sides of the testing machine via plastic clips were turned on and used to mitigate heat generated within the sample during fatigue testing. For some tests, the extensometer used for pre-fatigue modulus was kept on to record changes in displacement amplitude throughout testing. With grips closed, interlocks set, fans on, and loading parameters double-checked, fatigue loading was started. An initial loading envelope of 25 seconds was set on the user control panel. This means that the sinusoidal loading would gradually increase in amplitude and reach its maximum load 25 seconds (or 250 cycles at 10 Hz) after loading began. For longer fatigue tests, maximum and minimum position interlocks were set at 0.04 in. above and below the maximum and minimum position determined after the first 300 cycles of testing. Once testing concluded, the load was brought to zero in position control and the top grip was opened before releasing the specimen from the bottom block.

For fatigue tests with the extensometers attached, the extensometer reading was recorded by the user control panel and the extensometer's measured amplitude was displayed in real time. Unfortunately, the amplitude could not be recorded electronically, so the real-time value was recorded manually every 30 seconds either until the specimen reached its target reduction in modulus or 90 minutes (54,000 loading cycles) passed. The gradual increase in amplitude was often used as an approximation of the modulus reduction of the sample when determining when to stop fatigue cycling and measure residual modulus. For tests without the extensometer, stroke amplitude was used to approximate modulus reduction instead. Tracking the change in displacement amplitude via an extensometer was thought to be a closer approximation since only the displacement in the gauge region was accounted for, whereas tracking stroke amplitude factors in movement in the curvature and grip regions as well.

### **WET T-T Fatigue Testing**

While the same procedure was used for loading specimens and setting interlocks, WET T-T testing involved a different test setup. Like the RTA setup, the specimen was aligned in the specimen block first and torqued into the bottom block. Once aligned, the upper crosshead was raised so that a cylindrical acrylic bucket could be placed around the specimen. The acrylic bucket setup prior with the upper crosshead raised is shown in Figure 5-13. Figure 5-14 displays the bottom of the bucket, which was designed to compression fit to the O-rings surrounding the circular plate underneath the specimen block. A hose clamp was then placed over the O-rings and hand-tightened with a screwdriver. Once clamped, room temperature distilled water was poured into the bucket until the water level rose into the curvature of the dogbone specimen just below the top grip section. To reiterate, the specimens were conditioned in elevated temperature simulated salt solution, then fatigue tested in room temperature distilled water. The upper crosshead was then lowered into place and the top hydraulic grip was closed. The full WET testing setup including immersed specimen, closed grips, fixed hose clamp, and started cooling fans is displayed in Figure 5-15.

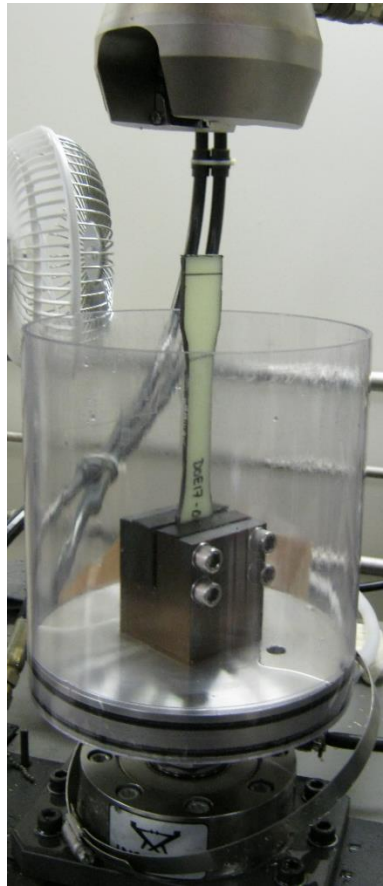


Figure 5-13. Acrylic bucket WET testing setup with raised upper crosshead and unattached hose clamp

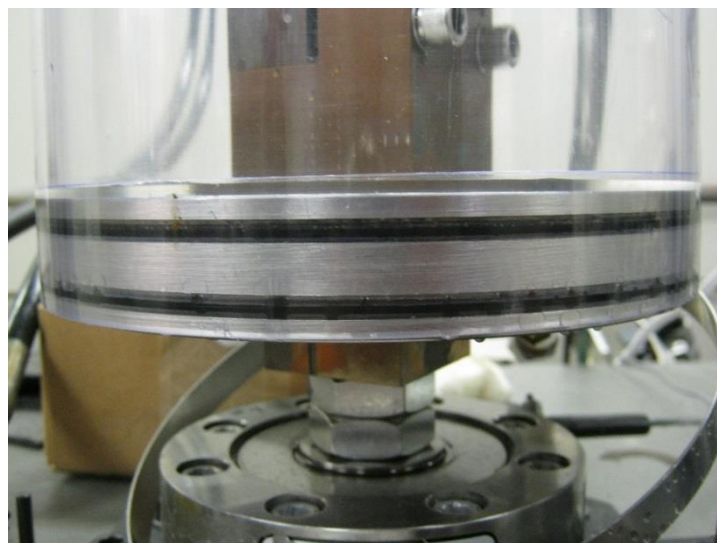


Figure 5-14. WET T-T fatigue setup with two compression fit O-rings to provide watertight seal

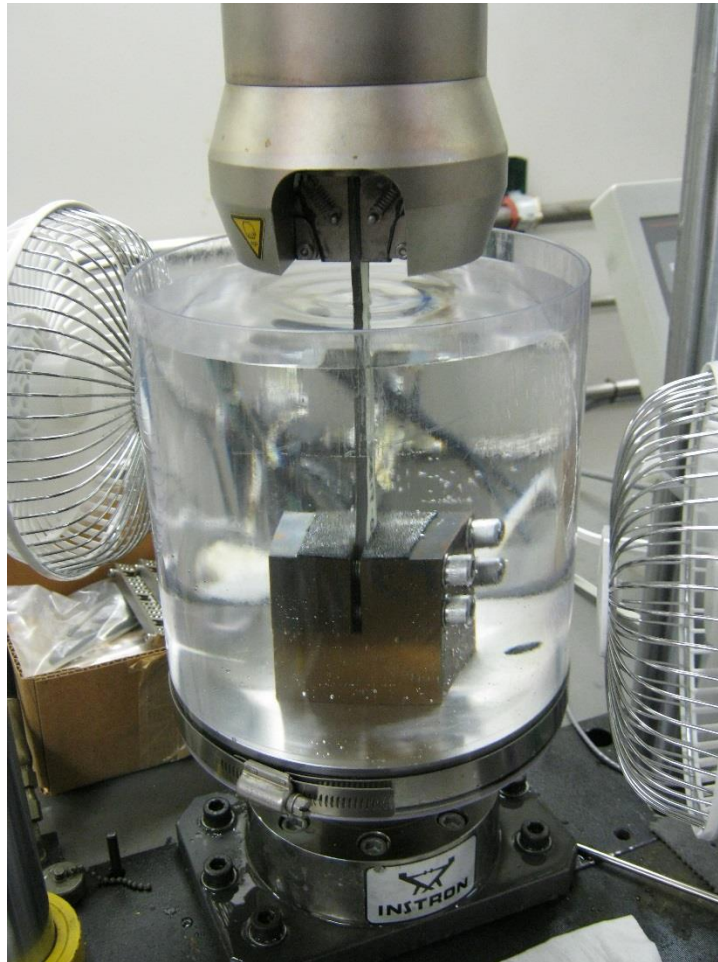


Figure 5-15. Full WET testing setup during fatigue loading including immersed specimen (viewed on edge), grips closed, hose clamp tightened, and cooling fans running

From this point, fatigue loading was applied in the same manner as the RTA samples. The extensometer could not be used for any of the WET samples so stroke amplitude was used to approximate modulus reduction for every WET sample. Once failure occurred or the appropriate modulus loss was reached, the specimen was unloaded in position control and the top grip was opened at near-zero load. The distilled water was then drained from the bucket by opening a ball valve attached to a hose that led into a container behind the testing machine. The hose was attached to a hole in the circular bottom plate below the specimen block, which allowed the water

to drain. Distilled water was reused in the WET testing program even though some hydraulic oil and composite dust entered the water during testing. After the water drained, the excess water remaining was dried by hand. The upper crosshead was then raised, the hose clamp was loosened, and the bucket was removed. The specimen was dried by hand using a Kim-wipe™ and the crosshead was lowered into position for the next test.

### **Post-Fatigue Residual Modulus**

Once fatigue loading concluded, and a specimen was thought to be at the correct reduction in elastic modulus, an extensometer was placed onto the specimen using rubber bands. If the specimen was not yet at the correct reduction in elastic modulus, the specimen was re-gripped and fatigue loading was resumed. The testing procedure for measuring residual elastic modulus was identical to the procedure used to measure the baseline modulus. However, the calculation of elastic modulus was performed differently. Residual modulus was calculated using a chord modulus from 0  $\mu\epsilon$  to the strain caused by the load corresponding to the baseline modulus measurement's 2,660  $\mu\epsilon$ . For instance, if the ten baseline modulus measurements of a sample revealed that, on average, a force of 900 lbf related to 2,660  $\mu\epsilon$  in that sample, then residual modulus would be calculated using a chord modulus between 0  $\mu\epsilon$  and the strain of the first data point that surpasses 900 lbf. Ten residual modulus measurements were recorded for each specimen along with their mean and standard deviation.

### **Post-Fatigue Residual Strength**

If the correct reduction in elastic modulus was reached, the damaged samples were removed from the INSTRON 8511 testing machine and placed in the servo-hydraulic INSTRON

8801. The 8801 was used because it had a 22.5 kip maximum force and failure occurred around 4-6 kip, above the maximum of the 8511. An extensometer was used for residual strength testing to record a stress-strain curve, although, elastic modulus was never calculated using this data since it was recorded at a 0.1 in./min, rather than 0.05 in./min. like those measured on the 8511. Although this machine had two hydraulic grips, a t-shaped bubble level was again used to level the specimen. The bottom grip was closed when the specimen was deemed level. The system was then put into load control keeping load from exceeding  $\pm 100$  lbf and the top grip was closed. This machine had a low gear for manual adjustments and a high gear for running tests. Load control was kept on when the machine was switched into high gear. These samples were loaded at a 0.10 in/min ramp rate until failure. Data was recorded automatically with an Instron data acquisition on a nearby computer. At least two specimens were residual strength tested for each fiber architecture/modulus reduction/maximum fatigue load combination.

## **Sectioning, Polishing, and Microscopy**

### **Sectioning**

Sectioning of samples refers to cutting the dogbone specimens —with the same diamond blade saw they were manufactured with—to produce small pieces that can later be polished for microscopy. Sectioning of samples for microscopy initially began with both longitudinal cuts (such as cut A in Figure 5-16) and transverse cuts (such as cut D in Figure 5-16). Initial microscopy showed little noticeable damage in transverse cuts so transverse cuts were removed from the sectioning plan for forensic microscopy of damaged samples. However, virgin samples included both longitudinal and transverse cuts to compare void contents measured by both types of cut.

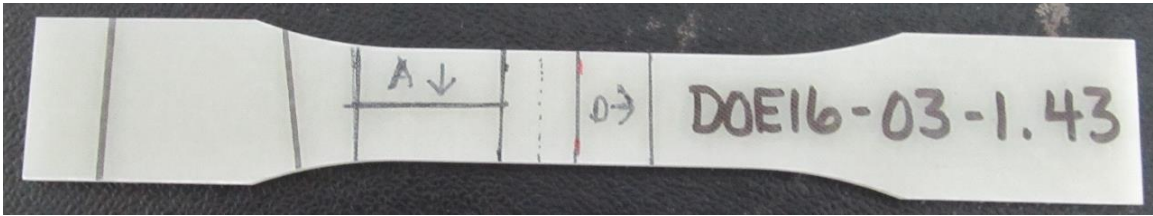


Figure 5-16. Longitudinal and transverse sectioning of virgin sample for microscopy

For damaged specimens, four longitudinal sections were cut as shown in Figure 5-17 and Figure 5-18. Once separated into the four sections, two mid sections (A & C) and two edges (B & D) were polished to evaluate damage within the samples. These sections were between 0.25 in. to 0.5 in. away from the midpoint of the dogbone specimen (shown as a red dashed line) and the sections were 1 in. long so that they fit in the ARL polishing puck mold.

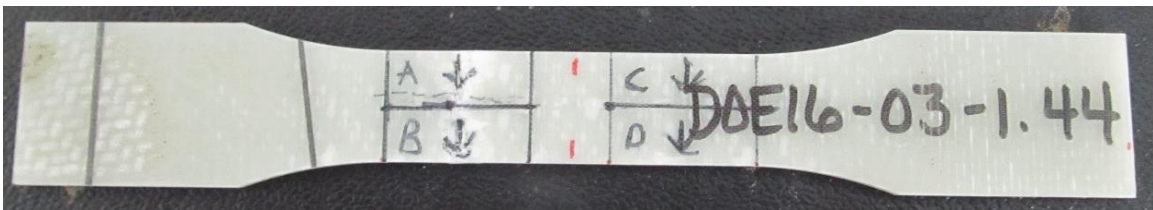


Figure 5-17. Four longitudinal sections mapped out prior to cutting



Figure 5-18. Longitudinal sections cut into four pieces.

### Polishing

Polishing began with placing the sectioned edge into a puck-shaped mold. The mold had approximately a 1.375 in. diameter and was about 1 in. deep. The desired edge from the cut

section was placed faced down in the mold while an undesired cut piece, usually from the grip region, was superglued to the back of the desired section. This was done to hold the specimen in place since the section only filled 0.25 in. of the mold's 1 in. depth. Scotch tape is also placed over the undesired piece to hold the pieces upright during curing. The result is shown in Figure 5-19. Next, EPON 8132 epoxy resin and HEXION 3274 hardener were mixed at a 100:42 stoichiometric ratio with a few drops of dark blue dye and poured into the mold. Once the resin hardened, it was taken to the polishing station.

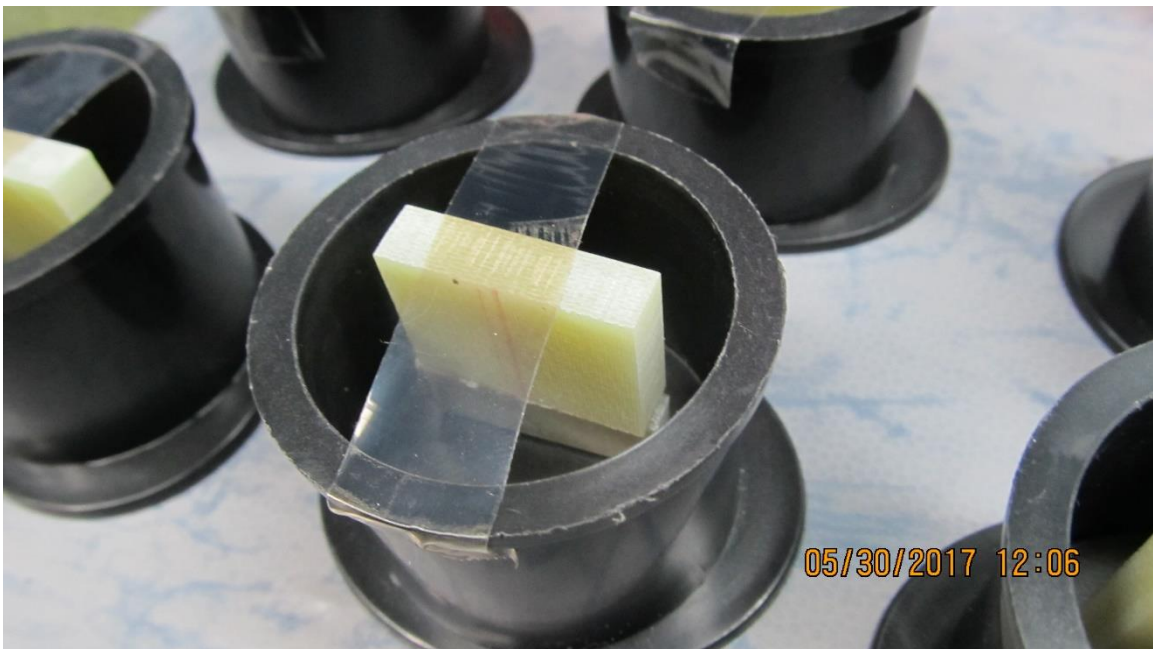


Figure 5-19. Polishing puck mold with extra composite piece for support

Table 5-1 displays the general procedure followed for the polishing of the puck specimens. A Leco GPX 300 polisher was used to polish every specimen, which could accommodate three pucks at a time. Deionized water was used during sanding in order to produce a smooth, wet-sanded surface finish. The table and the spindle both rotated the same way, but at different speeds as listed in the table. Monocrystalline diamond suspension 3 $\mu$ m and 1 $\mu$ m particles were used in conjunction with a polishing cloth to produce a micro-polish finish on the

surface of the puck. After the conclusion of each cycle, the sanding disc or polishing cloth was replaced and the next cycle was initiated. Once polishing was finished, the pucks were rotated upside-down so that the polished edge was protected by a surrounding plastic case and sent to microscopy for further analysis.

Table 5-5. Polishing procedure parameters including grits, rotational speeds, pressures, and cycle times

Sanding Disc Grit	Spindle Speed (rpm)	Table Speed (rpm)	Pressure (lbf)	Cycle Time (min)	Number of Cycles
320	65	120	1	2	Until Flat
800	65	120	1	2	3
1200	65	150	1	2	3
2400	80	150	2	2	3
4000	80	150	2	2	3
Polishing Cloth	Spindle Speed (rpm)	Table Speed (rpm)	Pressure (lbf)	Cycle Time	Number of Cycles
3 $\mu\text{m}$	80	300	2	3	2
1 $\mu\text{m}$	80	300	2	3	2

### Microscopy

Once the specimens were polished, they were analyzed with a modified optical microscope. The optical microscope was equipped with a 3.1 Megapixel digital camera for imaging. The camera software had a time lapse feature that allowed the user to set a defined time increment between photographs. Modifications were made to the camera including the addition of a belt-driven continuous rotation servo affixed to the translation table of the microscope, which allowed for automated movement. The servo was bidirectional and controlled by an Arduino microcontroller programmed with a step length manually adjusted with a potentiometer knob. The modified microscope setup is labelled and shown in Figure 5-20.

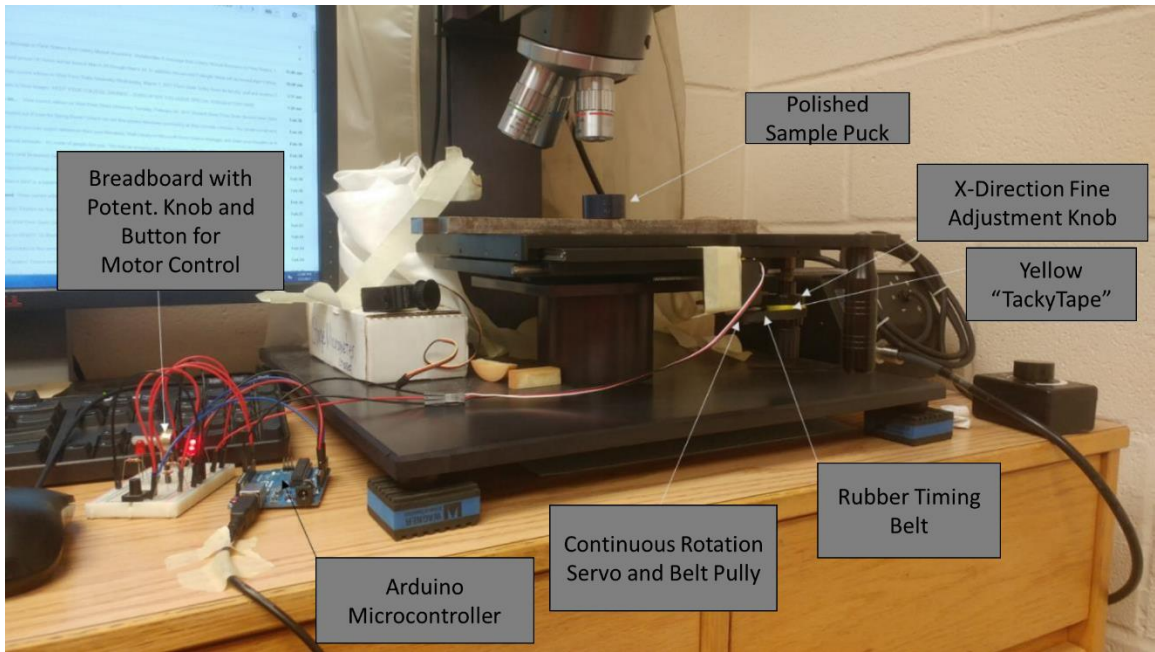


Figure 5-20. Diagram with labeled modifications to microscope for automated imaging

With quick, automated movement, side-by-side pictures could be taken of each sample and placed into an image stitching software for a full, high-definition cross section image. Microsoft Research’s Image Composite Editor (ICE) was chosen as the image stitching software for its reliability and its ability to stitch out-of-order images. Images taken by the microscope were saved as .tif files and input into ICE as such. Many of the first panoramas displayed high brightness gradients, like the gradient in Figure 5-21, not present in the original images. The microscopes digital camera parameters are shown in Table 5-6.



Figure 5-21. Initial microscopy cross section of specimen edge with unwanted brightness gradient

Table 5-6. Microscope digital imaging parameters

Microscope Parameters	Values
Exposure	40-60 ms
Gain	3.09
Gamma Value	0.96
Brightness	10
Contrast	66
Saturation	1
Hue	0
Time Lapse Interval	4 s

The issue was caused by an automatic vignette filtering feature built into ICE that occurs when brightness gradients vary even slightly in the original images. When looking at the original images, there appeared to be a small horizontal brightness gradient caused by uneven lighting from the microscope’s light source. Since the first panoramas were made of images of around 6 rows of 26 columns, the horizontal brightness gradient present in the images was magnified by the software’s built-in feature. To mitigate this issue, specimens were rotated 90° so that 26 rows of 6 columns of images were taken instead. Figure 5-22 shows the revised procedure’s resulting panorama of the same specimen shown in Figure 5-21.



Figure 5-22. Microscopy cross section with new procedure for mitigating brightness gradient

Once the panorama is completed, a user can zoom in on the panorama to view specific sections of the cross-section. An example of this is shown in Figure 5-23.

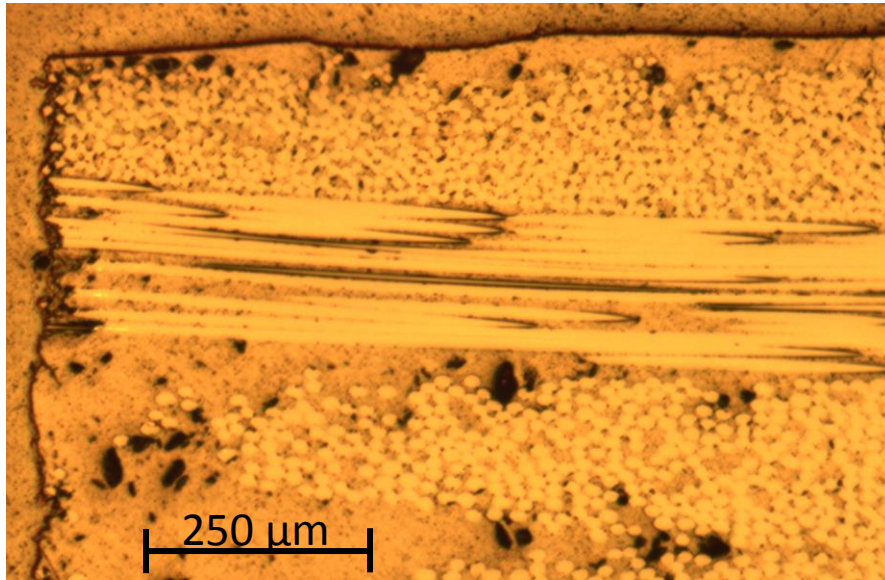


Figure 5-23. Zoomed-in view of upper-left corner of Figure 5-22

Void volume fraction was also calculated using the micrographs. Fiber volume and void volume percentages were initially intended to be calculated using the microscopy results. However, the matrix and fiber colors in the microscope images were too close to discriminate and only the black voids could be accurately measured. Void fraction was measured using 36 individual micrographs taken at random points throughout two woven and two stitched samples' cross sections. These micrographs were taken at 50x magnification. All four samples were virgin (unloaded) samples and one longitudinal and one transverse cross-section was analyzed for each material system. Each specimens' 36 micrographs were transferred into an image analysis software package named ImageJ, where they were converted into 8-bit grayscale images. Once in grayscale, each image could be set with a threshold that defined the difference between the black voids and the surrounding fiber/matrix mix. When the correct threshold was set, ImageJ would display the percentage of pixels in the image below the set threshold, and this value was taken to be the void volume percentage of each image.

The four sets of 35 data points were recorded in a spreadsheet where their Gaussian mean and standard deviation, and Gaussian coefficient of variation (COV) were calculated. COV was found by dividing the standard deviation by the mean. The Weibull characteristic value and modulus were calculated by sorting the measured void volume fractions ( $V_V$ ) from lowest to highest and assigning the values ranks from 1 to 35. Equations 21 and 22 are used to create 35 points for the Weibull plot. The Weibull modulus is calculated using the slope of the trendline created with these 35 data points and the Weibull characteristic value is found by raising  $e$  to the quotient of the trendline's  $y$ -intercept and the trendline's slope.

$$y = \ln \left( - \ln \left( 1 - \frac{Rank}{36} \right) \right) \quad (21)$$

$$x = \ln(V_V) \quad (22)$$

### **Digital Scanning**

A digital film scanner was used to record macroscale damage in the specimens caused by fatigue loading, water uptake, or both. Because the dogbone specimens are translucent, a film scanner can illuminate macro-scale cracks within the specimen and image them. The film scanner has a backlight that shines through the samples as the scanner scans the sample. An example of a specimen scan is shown in Figure 5-24, with a full specimen and magnified view to display damage around a critical crack. This method was used to scan every type of damaged and failed sample as well as virgin RTA and WET samples. The scanner was set to 2,400 dpi with 24-bit color and a low-level backlight correction.



Figure 5-24. Example of scanned image with magnified image displaying macro cracks

## References

- Ashton, J. E., Halpin, J. C., & Petit, P. H. (1969). *Primer on composite analysis*. Technomic, Stamford, CN.
- ASTM. (2003). *Standard Practice for the Preparation of Substitute Ocean Water (D 1141 – 98)*. West Conshohocken, PA: ASTM International.
- ASTM. (2011). *Standard Test Method for ignition Loss of Cured Reinforced Resins (D 2584 – 11)*. West Conshohocken, PA: ASTM International.
- ASTM. (2013). *Standard Test Method for Shear Properties of Composite Materials by the V-Notched Beam Method (D 5379)*. West Conshohocken, PA: ASTM International.
- ASTM. (2014). *Standard Test Method for Tensile Properties of Polymer Matrix Composites (D 3039)*. West Conshohocken, PA: ASTM International.
- ASTM. (2017). *Standard Test Method for Properties of Plastics (D 638 – 14)*. West Conshohocken, PA: ASTM International.
- Daniel, I. M., & Ishai, O. (2006). *Engineering Mechanics of Composite Materials*. New York: Oxford University Press.
- Juska, T. (2016, Nov). Personal correspondence. University Park, PA: The Pennsylvania State University Applied Research Laboratory. Data from the Mississippi Polymer Institute.
- Koudela, K. (2016, Oct). Personal correspondence. University Park, PA: The Pennsylvania State University Applied Research Laboratory.
- Russell, D. (2016, February 25). Datasheet [PDF]. Wattwil, Switzerland: Gurit.
- Strauch, E. (2016, Nov). Personal correspondence. University Park, PA: The Pennsylvania State University Applied Research Laboratory
- Sun, C.T. and Li, S. (1988). Three Dimensional Effective Elastic Constants for Thick Laminates, *Journal of Composite Materials*, 22: 629–639.

## Chapter 6

### Experimental Results

#### Void Fraction

##### Microscopy

Table 6-1 shows the results from the microscopy void fraction investigation including Gaussian and Weibull statistics implemented on the 36 data points for each sample taken at 50x magnification. The Gaussian mean was smaller than the Weibull characteristic value for all four samples. Additionally, transverse cut samples for both the stitched and woven samples showed lower void volume fractions than the longitudinal cut samples. The higher void measurements in the longitudinal samples could stem from the wider dimensions of the longitudinal samples allowing a higher proportion of long fiber-shaped voids than in the less-wide transverse samples. Figure 6-1 and Figure 6-2 display typical voids found during the microscopy of the virgin samples. Figure 6-3 shows the size of a typical micrograph used for void fraction measurement.

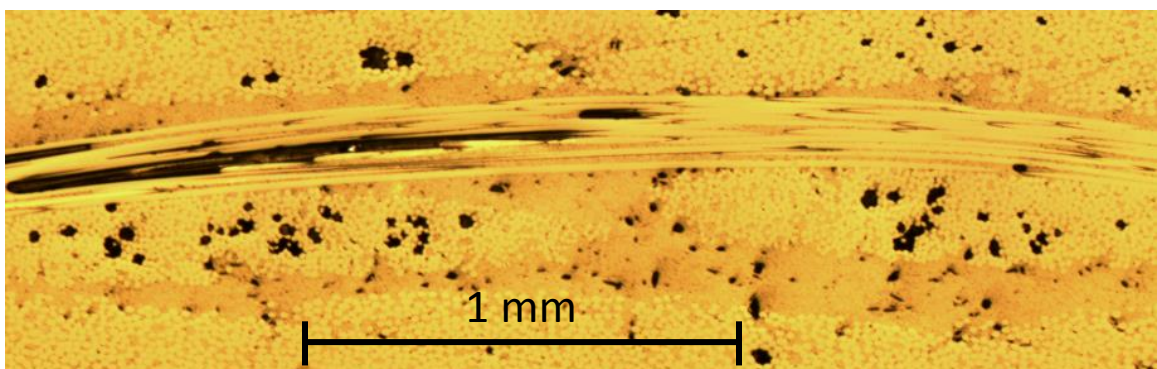


Figure 6-1. Typical voids in the WRE581T/ST94 woven laminate including voids in the fiber direction and assorted matrix voids

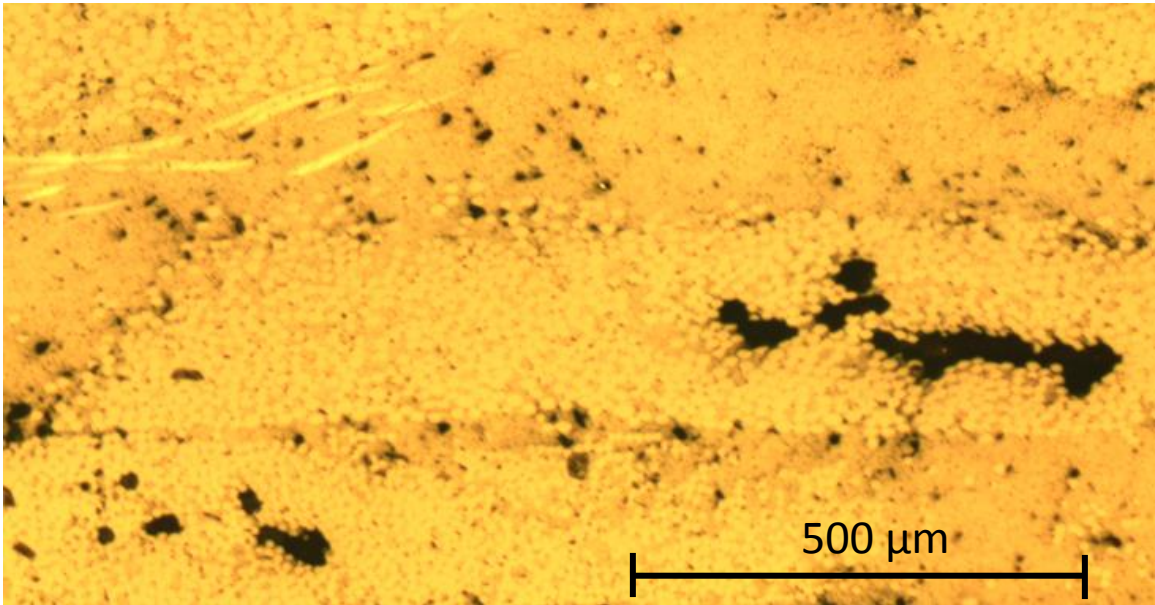


Figure 6-2. Typical voids in the QE1203/ST94 stitched laminate including oblong voids, matrix voids between plies, and voids near stitches (top left)

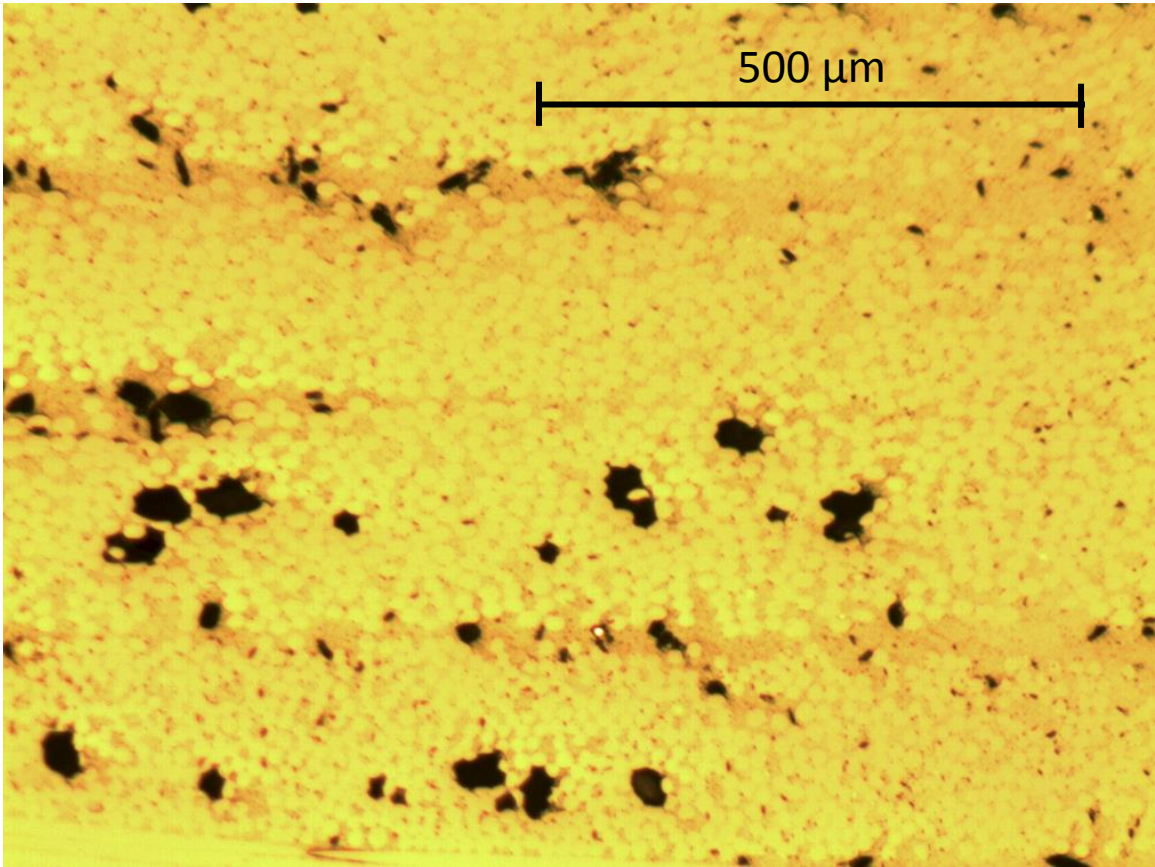


Figure 6-3. Example of one of the thirty-six 50x micrographs used for void fraction analysis

Table 6-1. Microscopy-determined void fraction results utilizing Gaussian and Weibull statistics

	Stitched		Woven	
	Longitudinal Cut	Transverse Cut	Longitudinal Cut	Transverse Cut
Gauss. Mean	2.126	1.915	3.345	2.689
Gauss. Std. Dev.	0.409	0.770	1.380	1.289
Gauss. COV	0.193	0.402	0.412	0.479
Weibull Char. Value	2.297	2.106	3.730	2.976
Weibull Modulus	5.605	2.982	3.306	2.5103

## ASTM 2584-11 Burnoff

Table 6-2 lists the fiber volume and void volume fraction results from the burnoff tests. Fiber density was determined to be 2.6717 g/cm<sup>3</sup> based on previous helium pycnometry measurements and Gurit provided a resin density of 1.22 g/cm<sup>3</sup>. Two specimens from each of the three manufactured panels were tested for voids. Stress-strain curves for baseline samples from each of the three panels are provided in the Stress-Strain curve section. Each specimen was a 1 in. x 1 in. square prepped and cleaned with acetone during dogbone specimen manufacturing.

Compared to the microscopy results, void fraction measured through burnoff was relatively low. This could be due to an imprecise assumed resin density or through an oversensitivity to black specs that were counted as voids in the microscopy results. Additionally, the micrographs used only provide a two-dimensional picture of voids in the matrix. The void fraction of the woven specimens was higher than the RTA stitched specimen panel, but only slightly higher than the WET stitched specimen panel. Higher fiber volume fractions were also found in the woven panel as compared to both stitched panels. The burnoff results also suggest that there is a measurable difference in both the fiber volume and void volume content between the two stitched panels, which were manufactured using the same material system and procedure.

Table 6-2. Burnoff void fraction results for RTA Stitched & Woven and WET Stitched samples

Specimen	$\rho$ Comp.	Wt% Fiber	Wt% Resin	Fiber Vol.	Void Vol.
RTA Stitched 1	1.8850	66.1771	33.8229	46.6903	1.0512
RTA Stitched 2	1.8685	65.4309	34.5691	45.7593	1.2973
RTA Woven 1	1.8873	66.9035	33.0965	47.2604	1.5409
RTA Woven 2	1.8848	67.2790	32.7210	47.5257	1.9855
WET Stitched 1	1.8568	64.8816	35.1184	45.8322	1.4583
WET Stitched 2	1.8484	64.5343	35.4657	45.5868	1.6190

### Baseline Modulus & Strength Measurements

The results from baseline testing are displayed in Table 6-3 (Juska, 2016) (Strauch, 2016). It should be noted that the woven roving moduli and strength are much higher than the stitch-bonded material because of the differences in layups (i.e. the woven roving does not contain 45° plies). These results will be compared to the Sun-Li model results in the next section.

Table 6-3. Baseline modulus and strength quasi-static testing results reported in MPa and ksi (Juska, 2016) (Strauch, 2016)

	QE1203/ST94 Stitch-Bonded [0°/45°/90°/-45°]		WRE581T/ST94 Woven Roving [0°/90°]	
	MPa	ksi	MPa	ksi
$E_{1c}$	18,600±400	2,700±58	25,100±1350	3,650±196
$E_{2c}$	N/A	N/A	27,000±1150	3,910±166
$G_{12c}$	N/A	N/A	4,350±1330	631±193
$\sigma_{UTS}$	340±9.38	49.3±1.36	487±25.1	70.6±3.64

### Quasi-Static Predictions

#### Sun-Li Model Prediction of Quasi-Isotropic Properties

The Sun-Li method slightly under-predicted the experimentally measured results for  $E_1$  and  $G_{12}$  of both material systems. The predictions for  $E_1$  and  $E_2$  as well as  $G_{12}$  are shown in Figure 6-4 and Figure 6-5. In these figures, the dashed lines represent plus or minus one standard deviation from the mean of the three baseline measurements while the solid lines represent the model predicted values. As mentioned in the previous section, the burnoff results showed

between 0.45 and 0.475 fiber volume content for both fiber architectures. This fiber volume fraction puts all predictions either just inside or slightly below the mean of the experimental baselines minus one standard deviation.

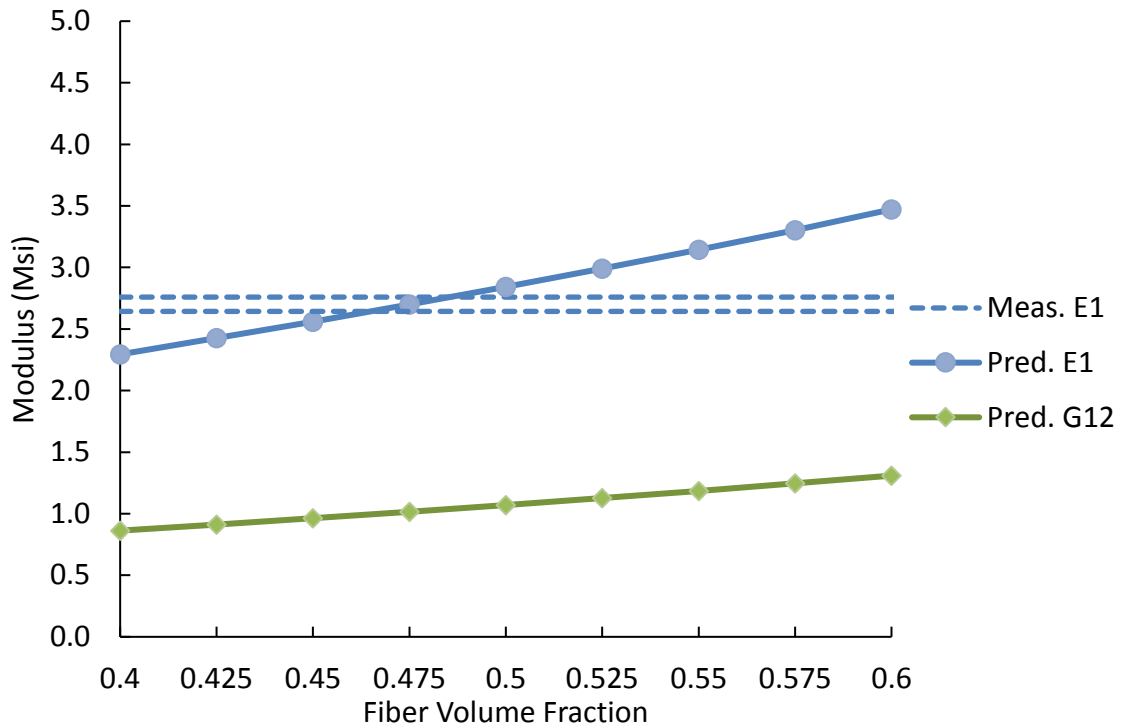


Figure 6-4. Comparison of quasi-static baseline results and Sun-Li model for stitch-bonded QE1203/ST94 quadaxial laminate with experimental results (dashed lines) shown as mean  $\pm$  1 std. dev.

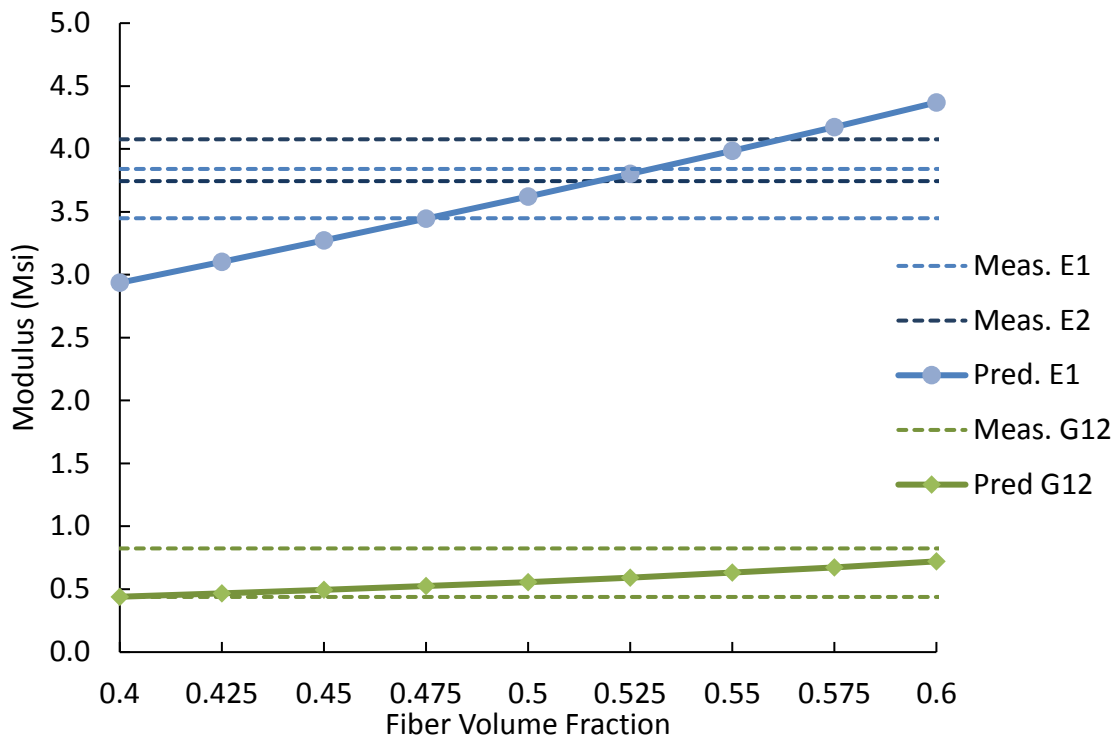


Figure 6-5. Comparison of quasi-static baseline results and Sun-Li model for woven roving WRE581T/ST94 [0°/90°] laminate with experimental results shown as mean  $\pm$  1 std. dev.

Quasi-static strength predictions contained more error than the Sun-Li model. In addition, the ply discount method incorrectly predicted the laminate with the higher strength. These errors most likely stem from the quasi-laminar assumption. The error may be caused by the use of textbook values listed for tape laminate plies as the ply strengths used in the Tsai-Wu failure criterion. Again, the quasi-laminar assumption suggests that a tape laminate can be used to predict the mechanical properties of a 2D woven or stitch-bonded laminate. Modulus loss just prior to failure is displayed with the ply discount results in Table 6-4. Some of the 45° plies fail at different loads due to the non-symmetric layup of the stitched laminate. During testing Transverse load and moments are kept at zero in the model.

Table 6-4 Results from ply-discount strength predictions using Tsai-Wu failure criterion with total applied stresses listed for each ply failure

Plies Discounted	Woven Roving WRE581T/ST94 [0°/90°/±45°] <sub>2s</sub>	Stitch-bonded QE1203/ST94 [(0°/45°/90°/-45°) <sub>2</sub> /(45°/90°/-45°/0°) <sub>2</sub> ]
90° (all)	10.45 ± 0.11 ksi	10.18 ± 0.32 ksi
±45° (outermost)	18.72 ± 0.20 ksi	16.74 ± 0.52 ksi
±45° (midplane)	18.72 ± 0.20 ksi	17.51 ± 0.55 ksi
±45° (remaining)	18.72 ± 0.20 ksi	17.51 ± 0.55 ksi
90° (2 <sup>nd</sup> time)	26.68 ± 0.28 ksi	25.88 ± 0.81 ksi
<b>0° (all) or Pred. Strength</b>	<b>59.74 ± 0.62 ksi (-4.9% error)</b>	<b>57.02 ksi ± 1.79 ksi (+36% error)</b>
<b>Measured Strength</b>	<b>62.85 ± 1.19 ksi</b>	<b>41.89 ± 1.42 ksi</b>
<b>Modulus Change at Failure</b>	<b>-29%</b>	<b>-30%</b>

The ply discount results were performed before a second stitch-bonded panel was manufactured for WET testing. Baseline, as-manufactured samples were quasi-static tested to measure baseline strengths for comparison to the first stitch-bonded panel. Three baseline samples from the second panel were found to have an average mean of  $50.1 \pm 1.6$  ksi. The strength of the second panel has a lower percent error (+13.8%) when compared to the panel's ply-discount predicted strength. Further investigation will be used to determine the cause of this difference in properties.

### Panel Comparisons & Stress Strain Curves

Figure 6-6 through Figure 6-10 depict the stress-strain curves of the woven and stitched samples quasi-statically tested for baseline strength measurements. As shown, the baseline RTA stress-strain curves for the two stitched laminates have an apparent difference even though they were manufactured and tested using the same conditions. This difference is still under investigation.

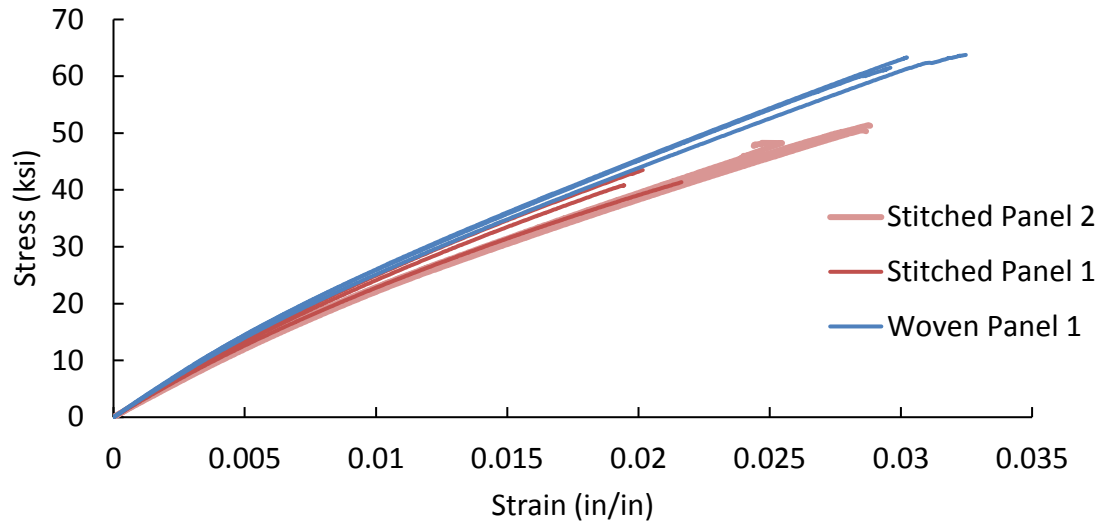


Figure 6-6. Stress-strain curves for three RTA baseline samples from each of the three panels manufactured for this study

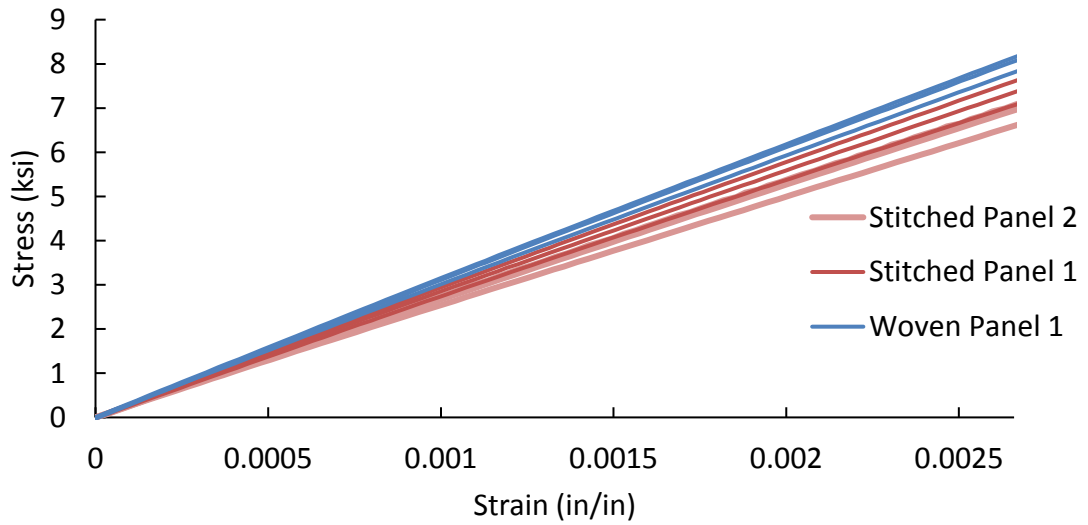


Figure 6-7. Stress-strain curves between 0 and 2,660  $\mu\epsilon$  for three RTA baseline samples from each of the three panels manufactured for this study

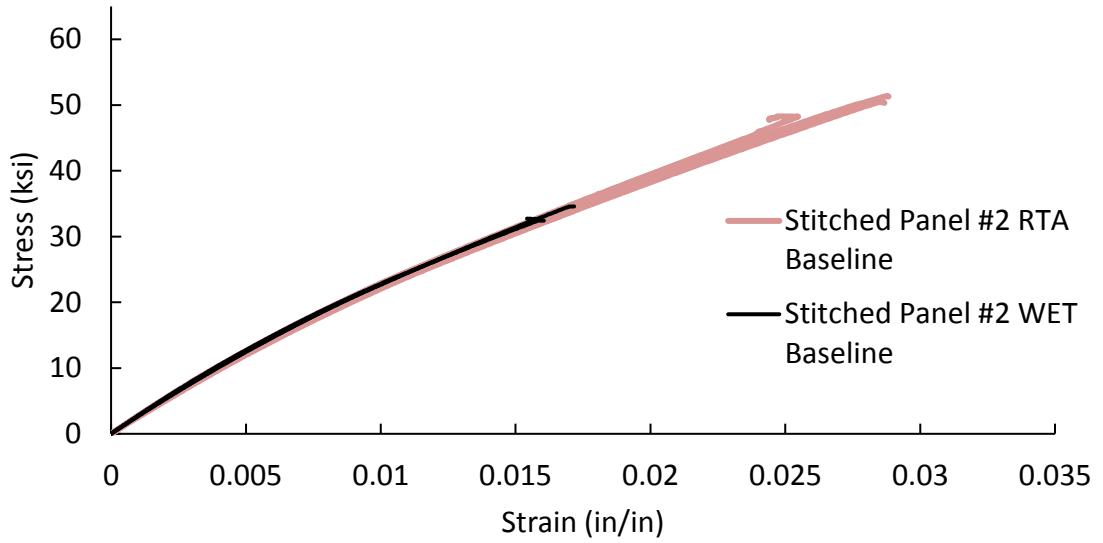


Figure 6-8. Stress-strain curves for three RTA baseline and three WET conditioned baseline samples from the second stitched panel used for WET testing

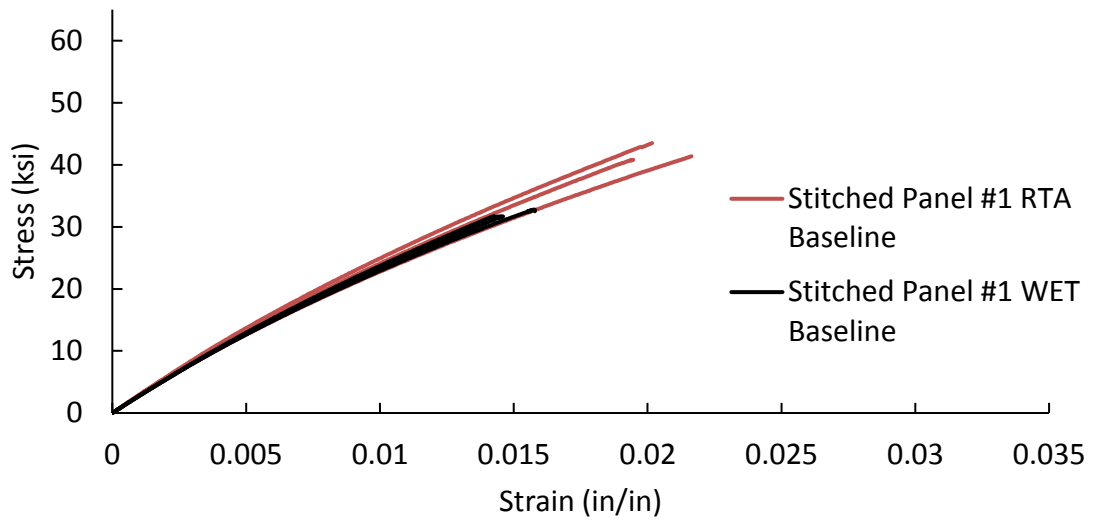


Figure 6-9. Stress-strain curves for three RTA baseline and three WET conditioned baseline samples from the first stitched panel used for RTA testing

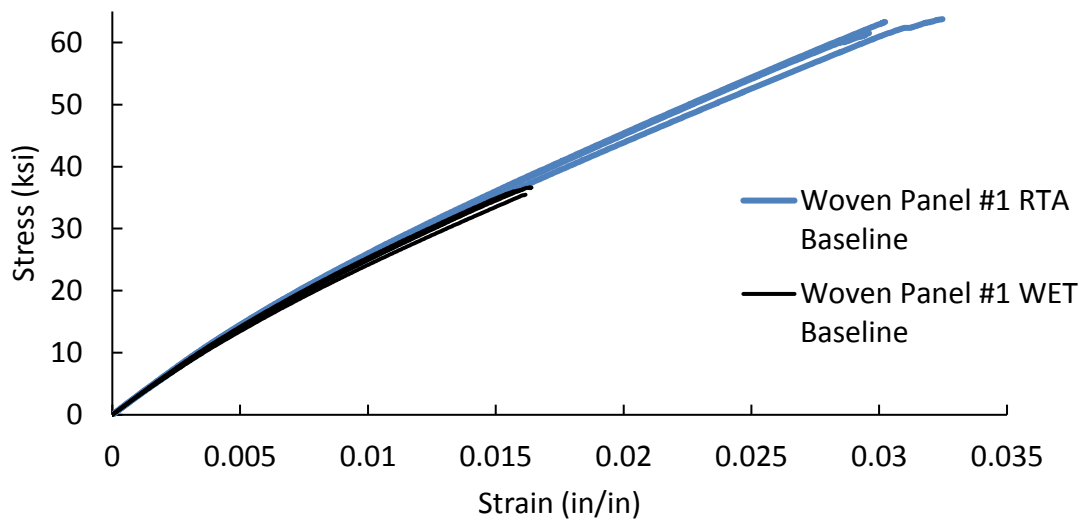


Figure 6-10. Stress-strain curves for three RTA baseline and three WET conditioned baseline samples from the woven panel used for RTA testing

### Water Uptake Measurements

Figure 6-11 displays the results from two weeks of water uptake measurements conducted on two stitched dogbone samples. The results show a mostly linear trend when plotted on with a square root of hours is plotted against weight percentage increase. However, this mostly linear trend implies that the two-week conditioning of the samples does not come close to saturation. To predict the weight percentage at saturation, Equations 1 and 2 are used to back out  $M_{\infty}$  based on each measurement. The resulting plots of each specimen with each model is plotted in Figure 6-12, and the predictions level off between 1.93% and 2.00% increase in weight. The diffusion coefficient was assumed to be a literature-suggested value of  $2.8 \text{ mm}^2/\text{s}$ , although, the exact epoxy and environment in which the epoxy was conditioned in was not stated.

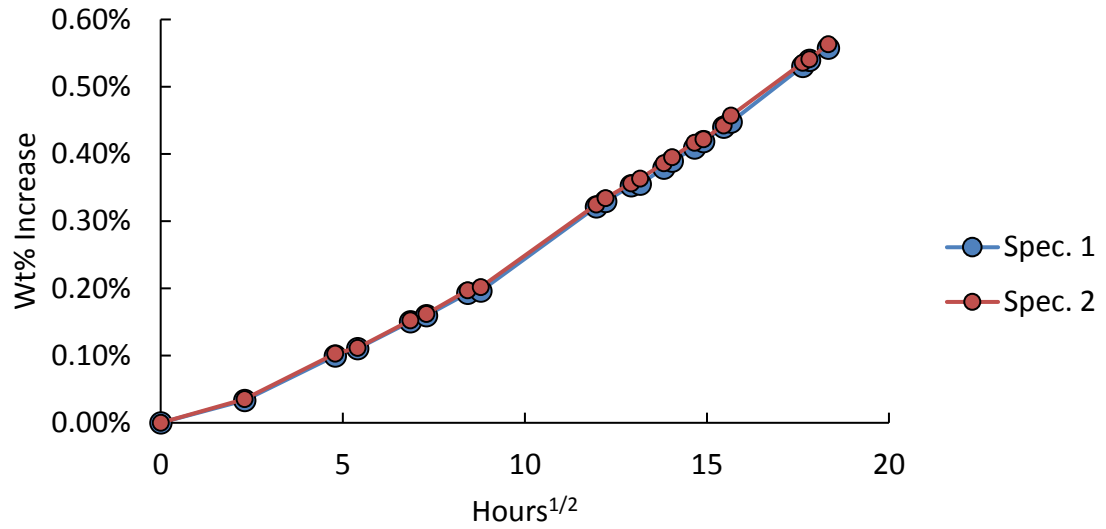


Figure 6-11. Water uptake measurements for two conditioned stitched dogbone samples over two weeks (336 hours)

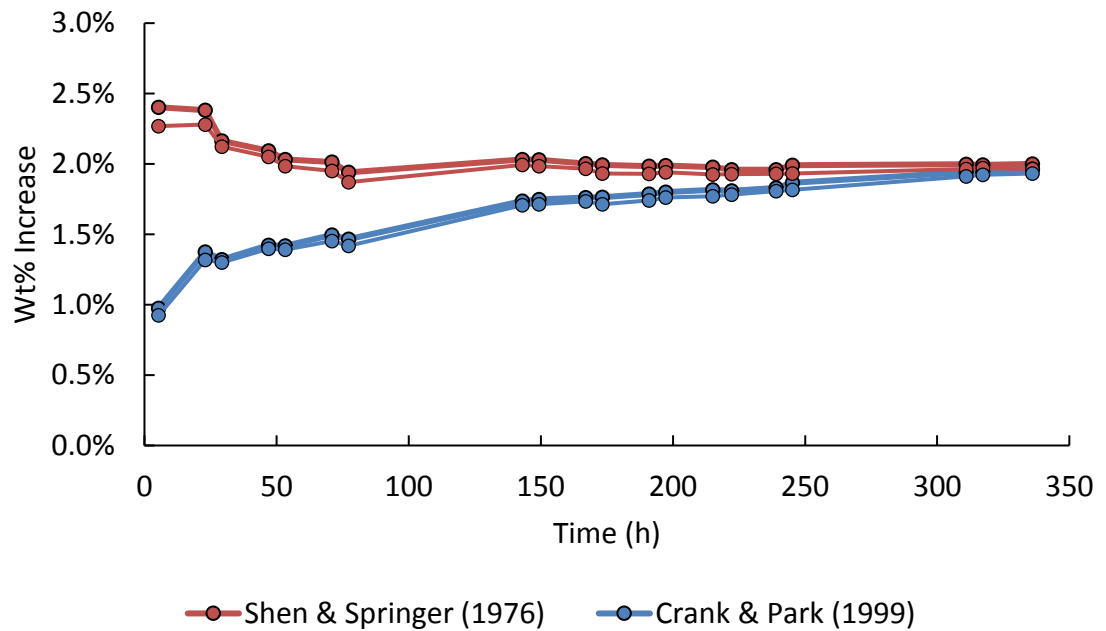


Figure 6-12. Water uptake models from Shen & Springer (1976) and Crank & Park (1999) plotted to predict saturation using weight uptake data points from two stitched samples with  $D=2.8 \text{ mm}^2/\text{s}$  (Jones, 2003)

## S-N Curve

### RTA S-N Curve

As mentioned in the procedure, the S-N curve for RTA tests was created by measuring the number of cycles at which failure occurred for fatigue loading at three different stress levels at  $R=0.1$  and  $f=10$  Hz. In the ensuing figures providing various fatigue testing results, QE1203/ST94 is denoted as the “stitched” material and WRE581T/ST94 is denoted as the “woven” material for simplicity and to keep the figures’ legends relatively small. “PAC” denotes unpublished data from prior testing of the common naval material (Koudela, 2016). While the initial plan called for testing specimens at maximum fatigue stresses of 28.75, 24, and 18 ksi, one sample of both the woven and stitched material was accidentally tested at a maximum stress of 25 ksi instead of 24 ksi, but the results are included in the final data set. Figure 6-13 displays the S-N curve for the RTA specimens of all three material systems. The S-N curve shows that both the stitched and woven systems outperform PAC in terms of fatigue life, especially at lower maximum stress values. PAC refers to a commonly used material for naval applications and comprises of Cytec 1583/5920, an 8-harness satin weave of E-glass combined with rubber toughened, autoclave cured epoxy. The stitched system has a shorter life than the woven system at higher maximum stress levels where failure occurs before 10,000 cycles, but appears to cross over and overtake the woven system at lower maximum stress levels. The difference in the shape of the S-N curve alludes to differences in the T-T fatigue failure mechanisms of each material system. The higher statistical scatter in the stitched system data compared to the woven system data also suggests differing failure mechanisms since both systems were tested equivalently. In fact, the two woven data points at a maximum stress of 28.75 ksi and the three data points at a maximum stress of 13.75 ksi appear to overlap one another.

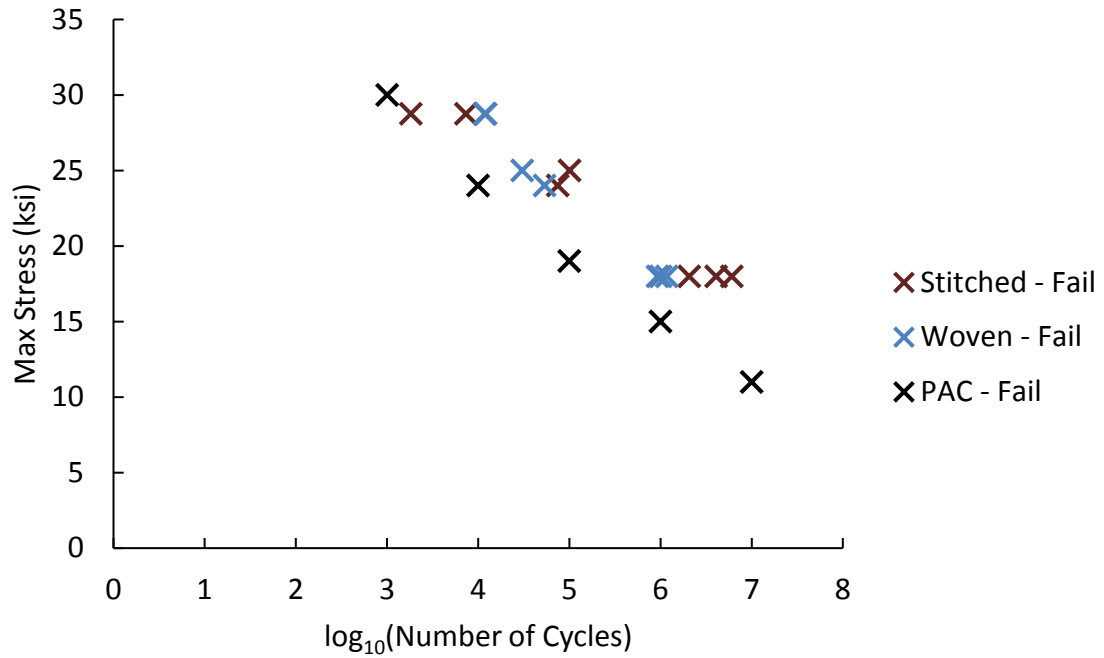


Figure 6-13. RTA S-N curve including QE1203/ST94 (Stitched), WRE581T/ST94 (Woven), and PAC data at maximum fatigue stresses of 28.75, 24, and 18 ksi (PAC data from Koudela, 2016)

Figure 6-14 displays the S-N curve plotted in Figure 6-15, but includes quasi-static strengths plotted as fatigue samples failed at one cycle. Through this plot, the linearity of the three material systems' S-N curves becomes apparent. The trendlines are plotted to show the reduction in maximum strength required to fail the materials as fatigue life increases. The slope of the trendline represents the decrease in strength per decade increase of fatigue life. Percentage decline of strength per increase in decade can be found by dividing the slope by the y-intercept from trendlines. The stitched fatigue strength declines at -8.61% per decade, the woven material declines at -12.4% per decade, and the PAC material declines at -11.4% per decade.

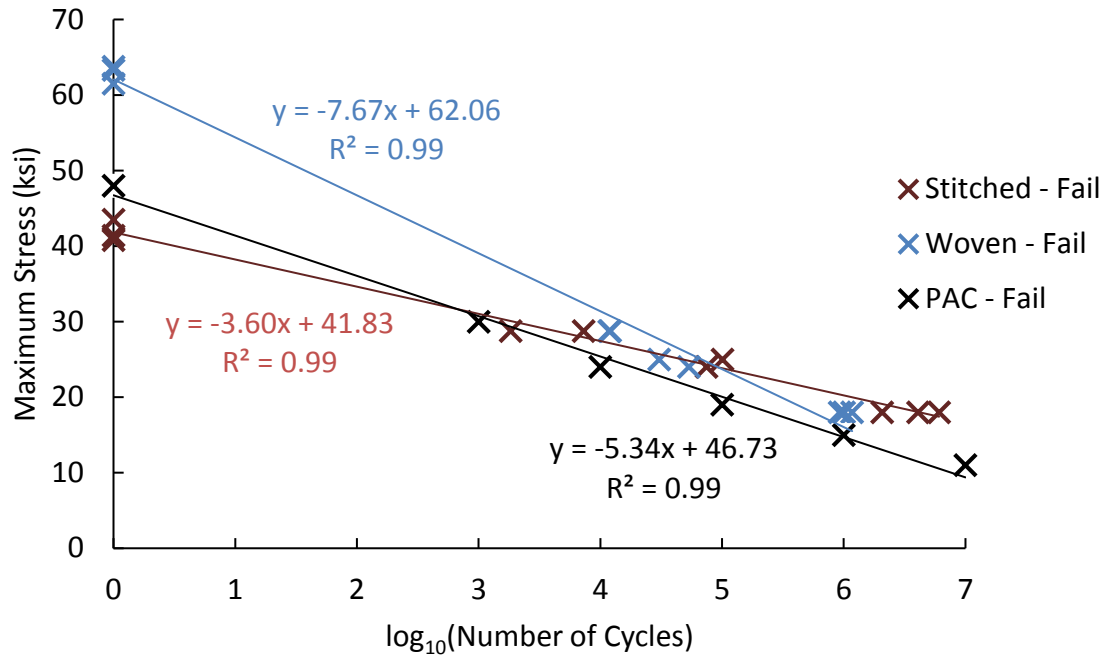


Figure 6-14. RTA S-N curve for stitched, woven, and PAC material systems including quasi-static strength data and trendlines with equations shown in matching colors (PAC data from Koudela, 2016)

### WET & RTA S-N Curve

When the WET data is plotted against the RTA data, a loss of fatigue life between one-half decade and one decade becomes apparent. Figure 6-15 displays the WET S-N data plotted with the previously shown RTA S-N data. Note that the *x*-axis now begins at 100 cycles to better view the data points adjacent to one another. While the WET data points for the stitched system shift to the left in the figure, the same S-N shape prevails (within the scatter of each data set) implying that the failure mechanisms have stayed the same, but other factors, such as degradation

of the matrix, have caused a decline in the material's strength. Post-fatigue damage and failure analysis of specimens are shown in later microscopy and scanning result sections.

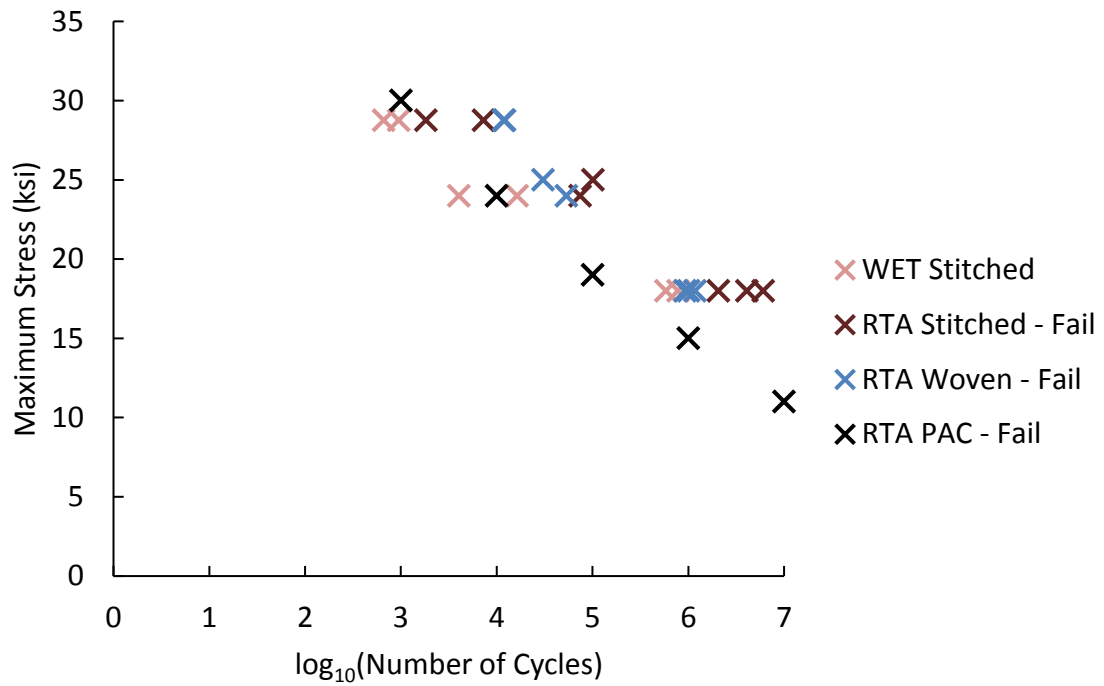


Figure 6-15. WET and RTA S-N curve including QE1203/ST94(Stitched), WRE581T/ST94 (Woven), and PAC data at maximum fatigue stresses of 28.75, 24, and 18 ksi (PAC data from Koudela, 2016)

Figure 6-16 displays the quasi-static baseline strengths measured in RTA and WET conditions of each of the stitched panels and includes other fatigue failed samples plotted in previous figures. For WET samples, strength declines at -8.0%, whereas the RTA samples declined at -8.6%.

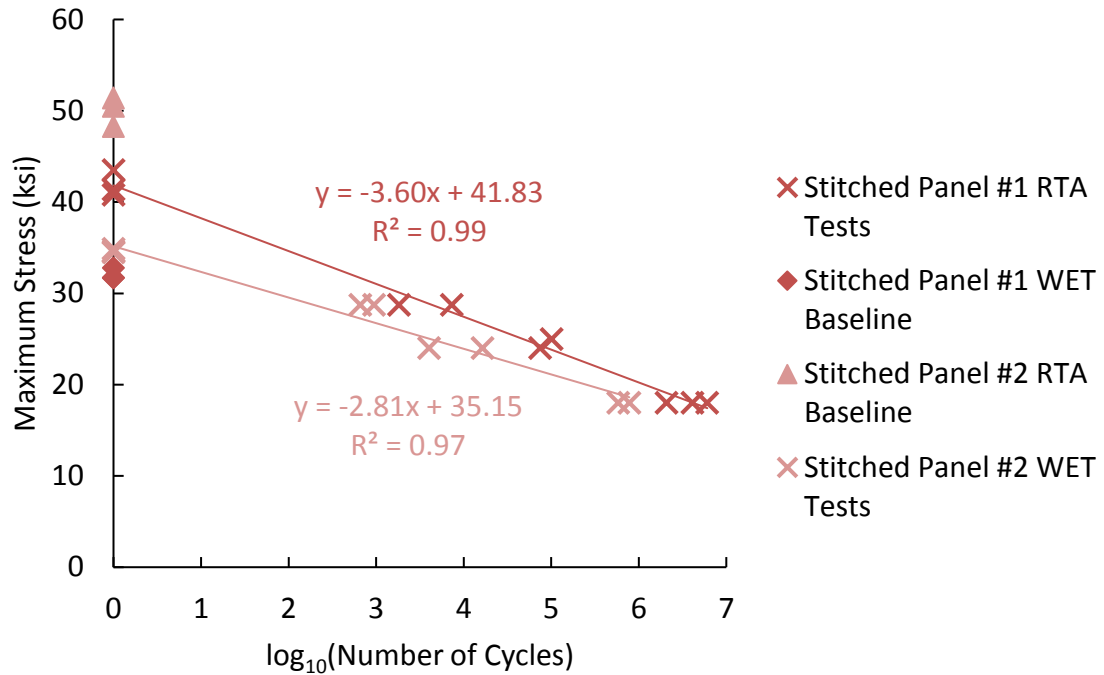


Figure 6-16. S-N curve for the two stitched panels including quasi-static strength data in both RTA and WET conditions and color-coded trendlines

### Modulus Reduction & Residual Strength

#### RTA

The RTA residual modulus results are broken up into two sections: one including data points from 13.75 ksi maximum fatigue stress samples and the other from 18 ksi maximum fatigue stress samples. Results are plotted with number of cycles on a logarithmic scale and change in modulus (modulus reduction) on a linear scale.

### 13.75 ksi maximum

Figure 6-17 shows the modulus loss data collected for the 13.75 ksi maximum fatigue samples. The woven material system shows a general linear trend downward between 10 and 17% reduction in elastic modulus. As a reminder, each individual samples' residual (post-fatigue) modulus is compared against the individually measured baseline modulus for that sample. As shown previously in the S-N results, the woven material system tends to have less statistical scatter when compared to the stitched samples. To quantify the difference, the woven data set has a Pearson's correlation coefficient of -0.948 whereas the stitched data set's is -0.323. It is difficult to make an overarching comparison between the two material systems because of the spread of the stitched data. Pearson's correlation coefficient quantifies the linear correlation in a given data set. A coefficient of 0 suggests an uncorrelated data set and a value of 1 or -1 suggests a perfectly positively or negatively correlated data set, respectively. Pearson's correlation coefficient is denoted as the square root of  $R^2$  in Microsoft Excel's commonly used trendline plotting tool.

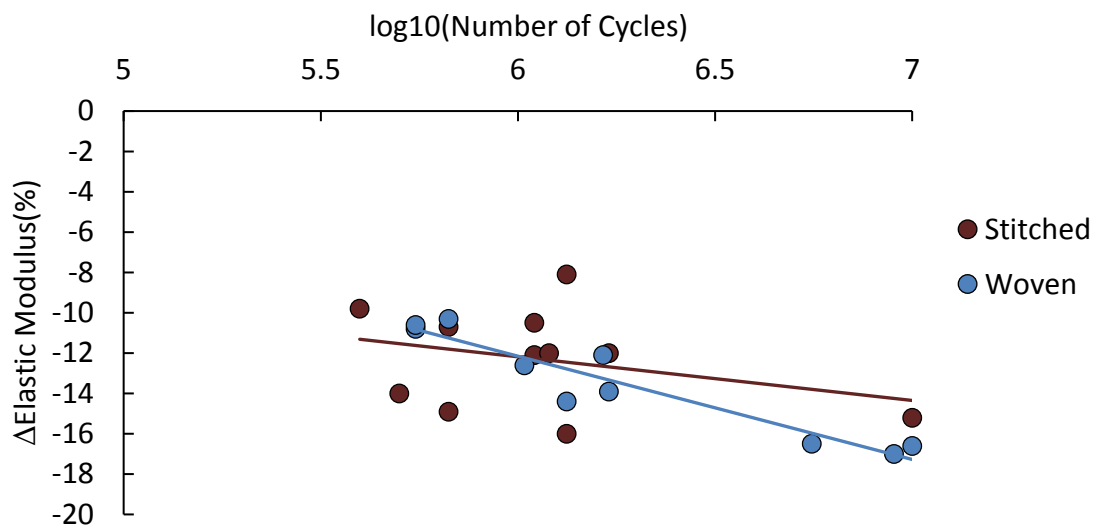


Figure 6-17. Quantification of damage through plotting number of cycles vs. modulus reduction for RTA woven and stitched samples tested at 13.75 ksi maximum (includes linear trendlines)

Figure 6-18 and Figure 6-19 display the residual strength data of both material systems plotted against number of cycles and reduction in elastic modulus, respectively. Reductions in elastic modulus are shown as positive values along the  $x$ -axis to display a negative slope in Figure 6-19 even though the actual changes in modulus are negative. Again, since each specimens' strength could only be measured once, all residual strength specimens were compared against results from three baseline measurements (two material systems so six baselines total). Unlike the residual modulus results, there are statistically-evident differences in the stitched and woven data sets. The woven specimens tend to have higher reductions in residual strength than the stitched specimens at higher cycle counts and at higher reductions of elastic modulus. This result is similar to the idea stemming from the S-N data that the stitched samples exhibits less damage, at least in a Paris Law sense, than woven samples; microscopy and specimen scans will identify whether visible damage follows the same trend.

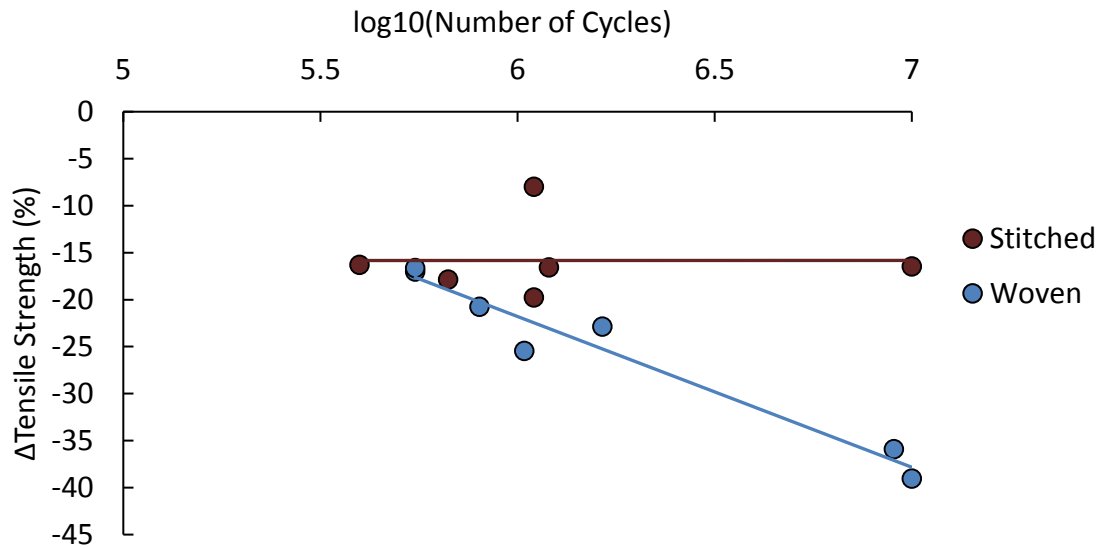


Figure 6-18. Quantification of damage through plotting number of cycles vs. change in tensile strength for RTA woven and stitched samples tested at 13.75 ksi maximum (includes linear trendlines)

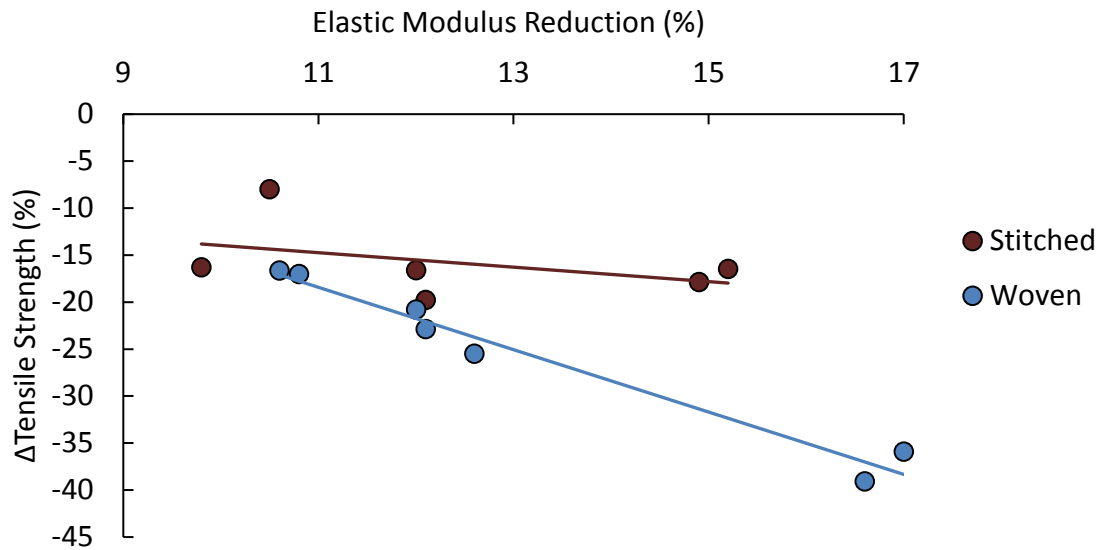


Figure 6-19. Quantification of damage through plotting modulus reduction vs. change in tensile strength for RTA woven and stitched samples tested at 13.75 ksi maximum (includes linear trendlines)

***18 ksi maximum***

Figure 6-20 shows the modulus loss data collected for the 18 ksi maximum fatigue samples. Compared to the samples from the 13 ksi maximum dataset, the Pearson’s correlation coefficient has increased in both datasets. Although the plots of both material systems seem to overlap one another, the general trends show a slight offset, with stitched specimens tending to encounter less change in elastic modulus over the same number of cycles. The slopes of the two trendlines suggest that there is a crossover point between a modulus reduction of 8% and 10%.

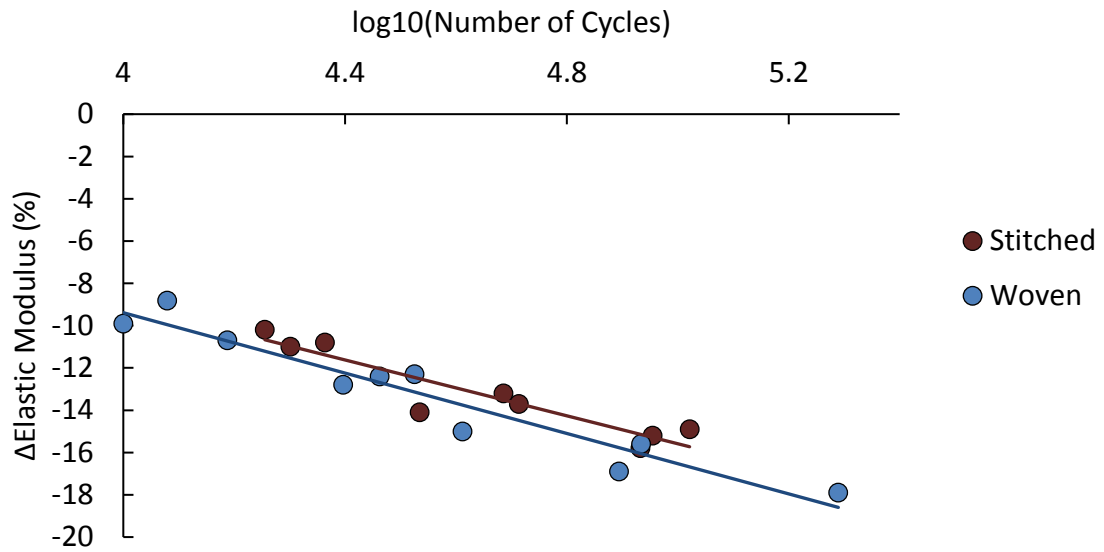


Figure 6-20. Quantification of damage through plotting number of cycles vs. modulus reduction for RTA woven and stitched samples tested at 18 ksi maximum (includes linear trendlines)

Figure 6-21 shows the full data comparison for the residual modulus measurements from both the 13.75 ksi maximum and the 18 ksi maximum data sets. The compared data shows an almost two-decade difference between the data sets. Additionally, the trendlines from the 13.75 ksi maximum data have a slightly lower magnitude slope than the 18 ksi data implying that the 13.75 ksi maximum samples accumulate damage more slowly than the 18 ksi maximum samples.

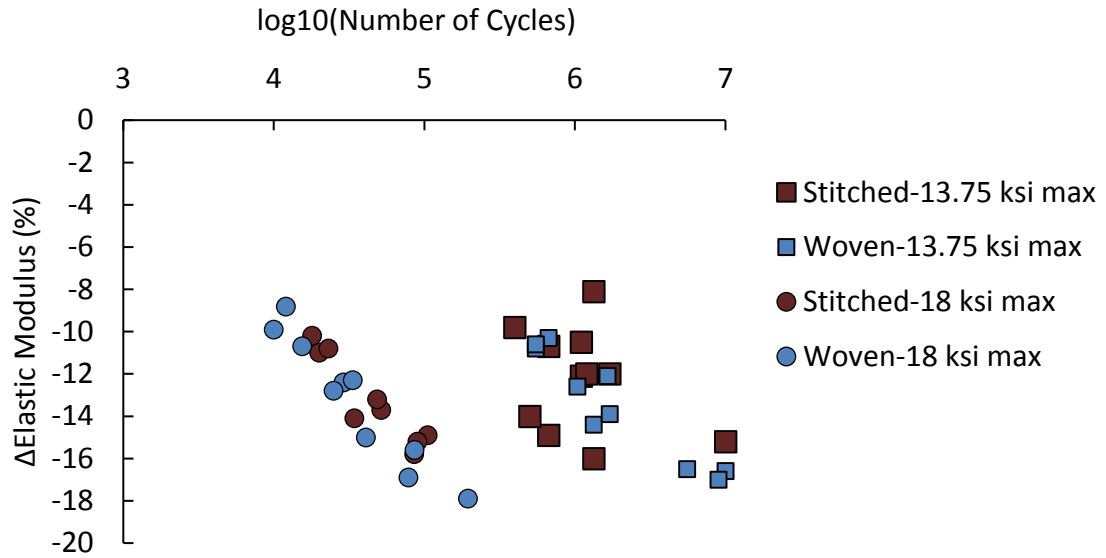


Figure 6-21. Comparison of damage accumulation within 13.75 ksi maximum and 18 ksi maximum woven and stitched RTA specimens through plot of number of cycles vs. modulus reduction

Figure 6-22 and Figure 6-23 display residual strength data for the RTA 18 ksi maximum samples. Unlike the data for the 13.75 ksi maximum samples, fatigue was run to failure for six of the 18 ksi maximum samples. These failed samples are plotted on the strength loss chart by assuming fatigue failure occurred when residual tensile strength fell to 18 ksi. The failed samples are not plotted on the change in modulus chart because elastic modulus was not measured prior to failure. It is difficult to discern general trends in the figures due to the statistical scatter in the data, although two main points can be made. First, most woven samples encounter higher losses in tensile strength over the same number of cycles or losses in modulus when compared to stitched samples. Second, there appears to be a residual strength drop-off somewhere in between 16% modulus reduction and failure for both stitched and woven samples tested at an 18 ksi maximum fatigue load.

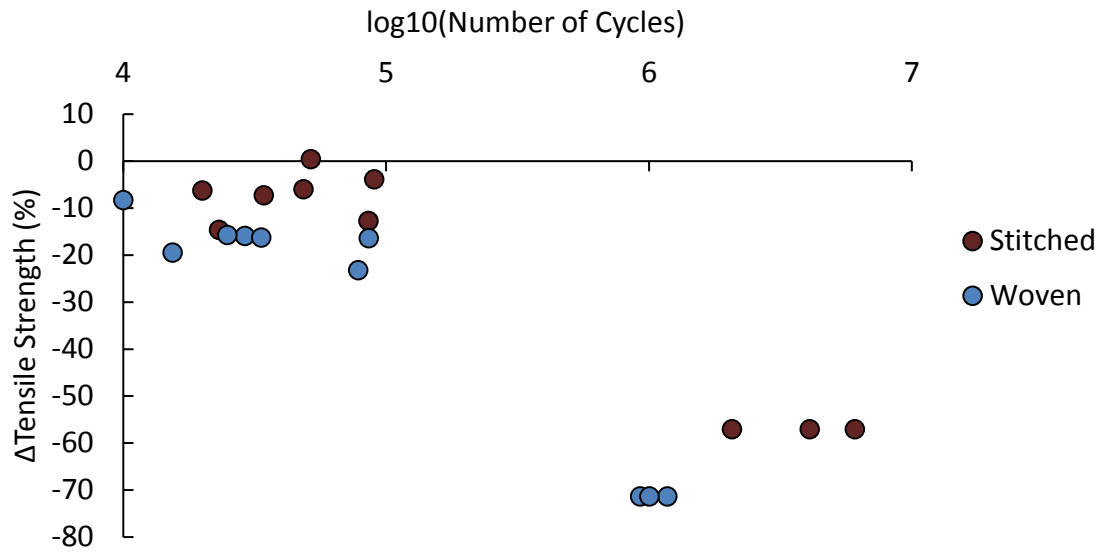


Figure 6-22. Quantification of damage through plotting modulus reduction vs. change in tensile strength for RTA woven and stitched samples tested at 18 ksi maximum (includes linear trendlines)

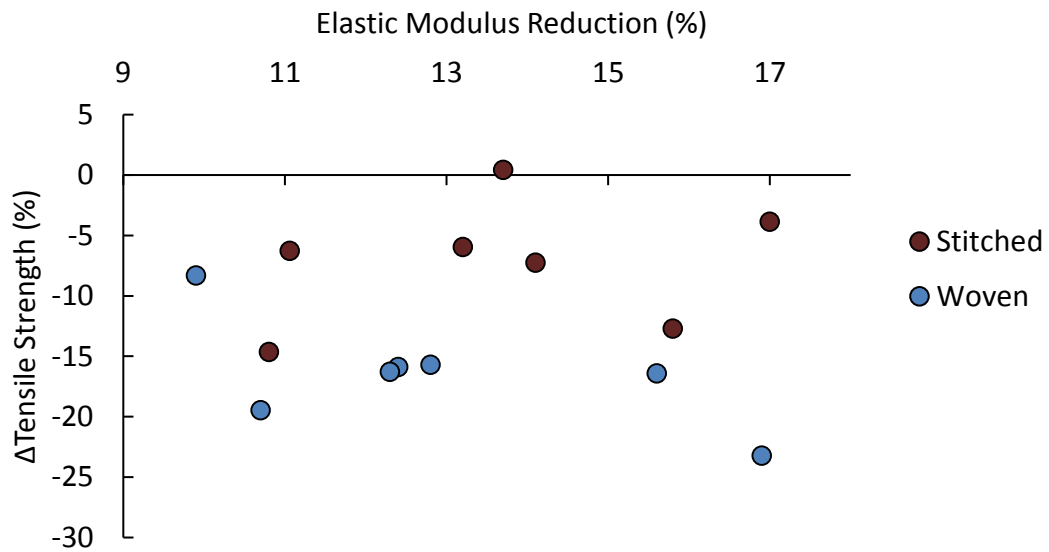


Figure 6-23. Quantification of damage through plotting modulus reduction vs. change in tensile strength for RTA woven and stitched samples tested at 18 ksi maximum (includes linear trendlines)

Figure 6-24 and Figure 6-25 display the residual strength comparison data charts for the 13.75 ksi maximum and the 18 ksi maximum data sets. Figure 6-24 indicates that woven samples

tested at lower fatigue stress levels may have a more gradual drop off in strength reduction compared to woven samples tested at higher fatigue stress levels. While this may also be true for stitched samples, it is difficult to determine due to the variability of the stitched specimen data. Again, when drawing comparisons between the stitched and woven data, the stitched data appears to accumulate damage more slowly than the woven data, but it is difficult to quantify this difference.

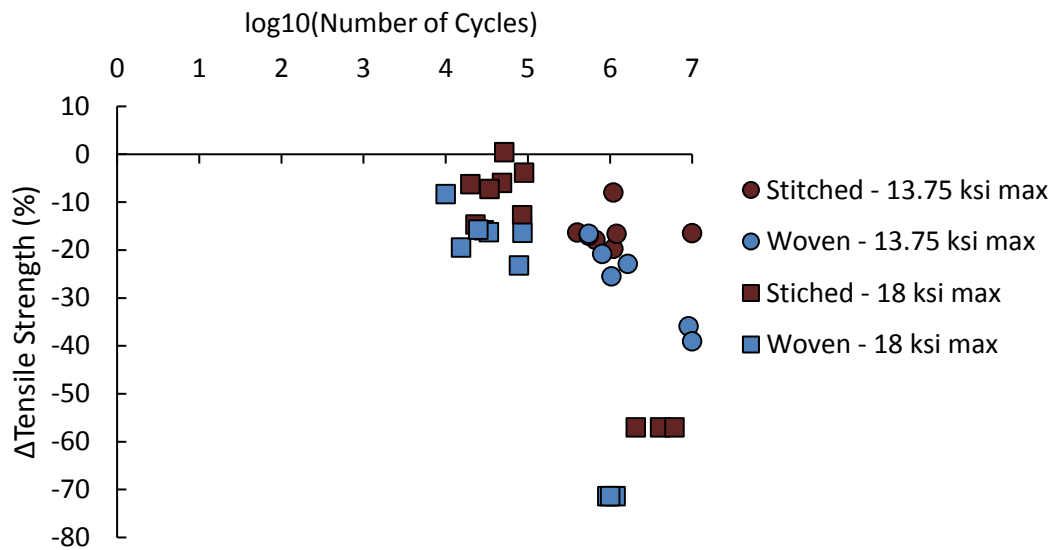


Figure 6-24. Comparison of damage accumulation within 13.75 ksi maximum and 18 ksi maximum woven and stitched RTA specimens through plot of number of cycles vs. change in tensile strength

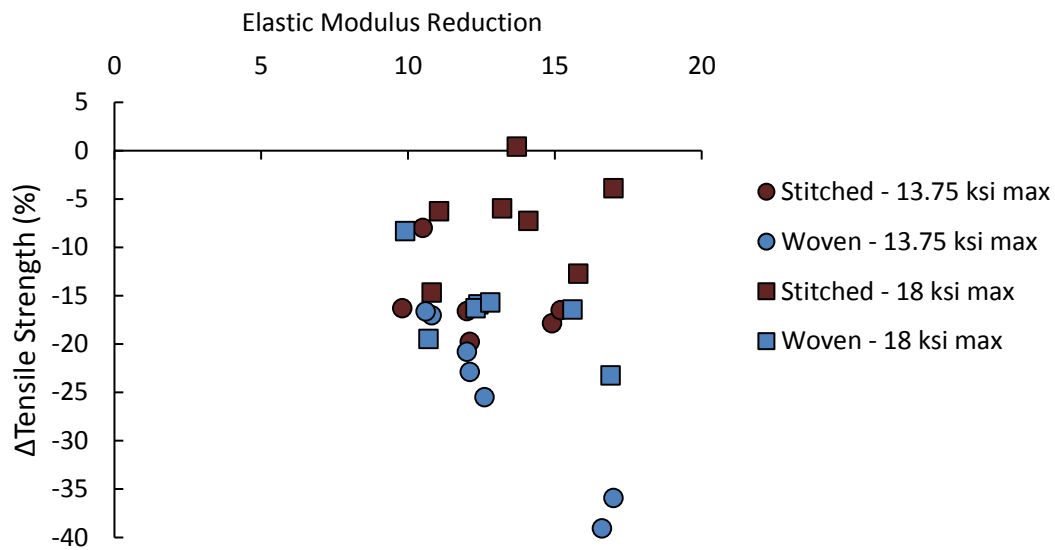


Figure 6-25. Comparison of damage accumulation within 13.75 ksi maximum and 18 ksi maximum woven and stitched RTA specimens through plot of elastic modulus reduction vs. change in tensile strength

## WET

A general trend that can be seen for the stitched specimens is equal amounts of damage occurring nearly a decade earlier in WET tested specimens when compared to RTA specimens. Figure 6-26 and Figure 6-27 display this trend in modulus reduction samples at 13.75 ksi and 18 ksi maximum, respectively. The stitched data from these charts are plotted together in Figure 6-28 for comparison. Figure 6-29 shows the drop-off in residual strength over time for both WET and RTA stitched samples as well as RTA woven samples for comparison. The baseline strength used for the WET tested stitched specimens comes from the mean quasi-static strength of three “as-manufactured” samples. Figure 6-30 plots just the WET tested stitched specimen data from Figure 6-29 for ease of viewing.

*13.75 ksi maximum*

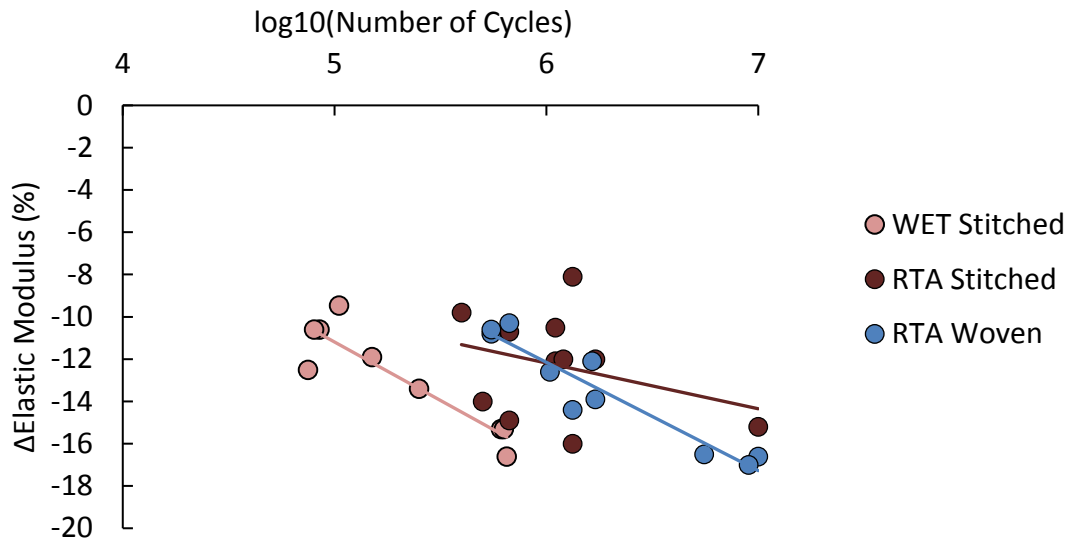


Figure 6-26. Quantification of damage through plotting number of cycles vs. modulus reduction for RTA and WET samples tested at 13.75 ksi maximum (includes linear trendlines)

*18 ksi maximum*

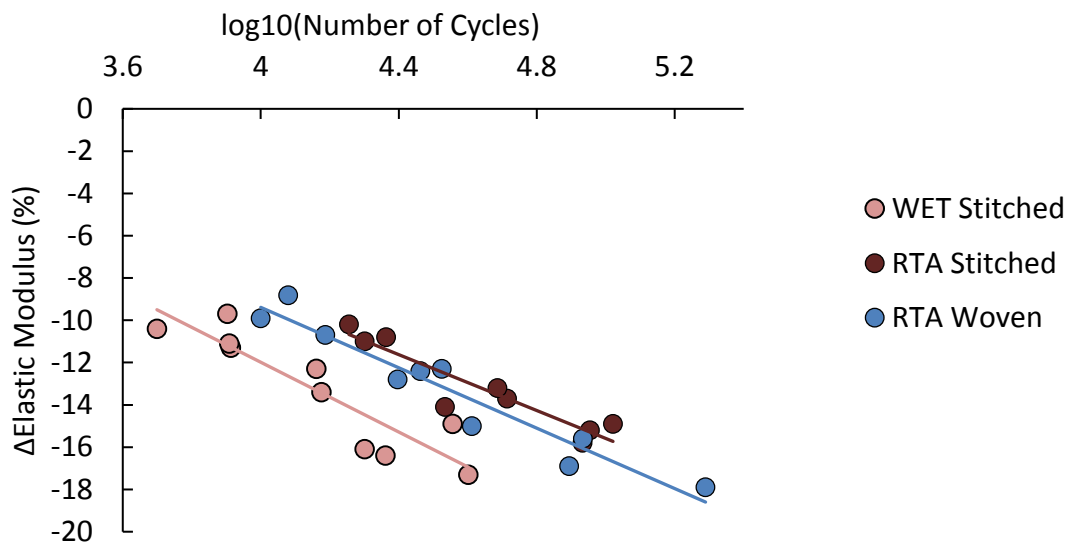


Figure 6-27. Quantification of damage through plotting number of cycles vs. modulus reduction for RTA and WET samples tested at 18 ksi maximum (includes linear trendlines)

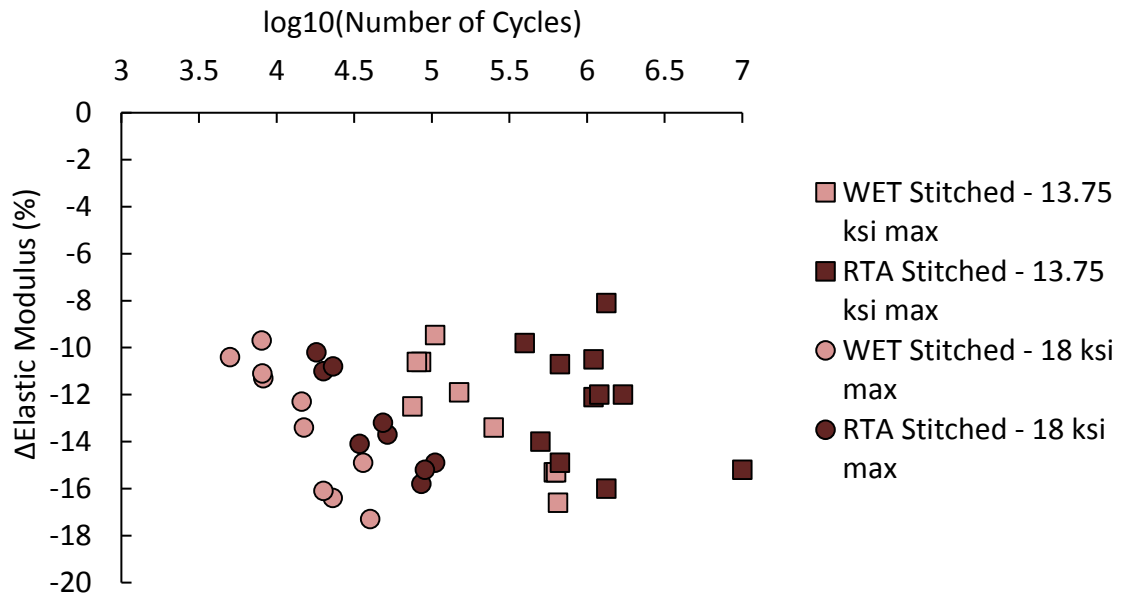


Figure 6-28. Quantification of damage through plotting number of cycles vs. modulus reduction for RTA and WET samples tested at 13.75 and 18 ksi maximum (includes linear trendlines)

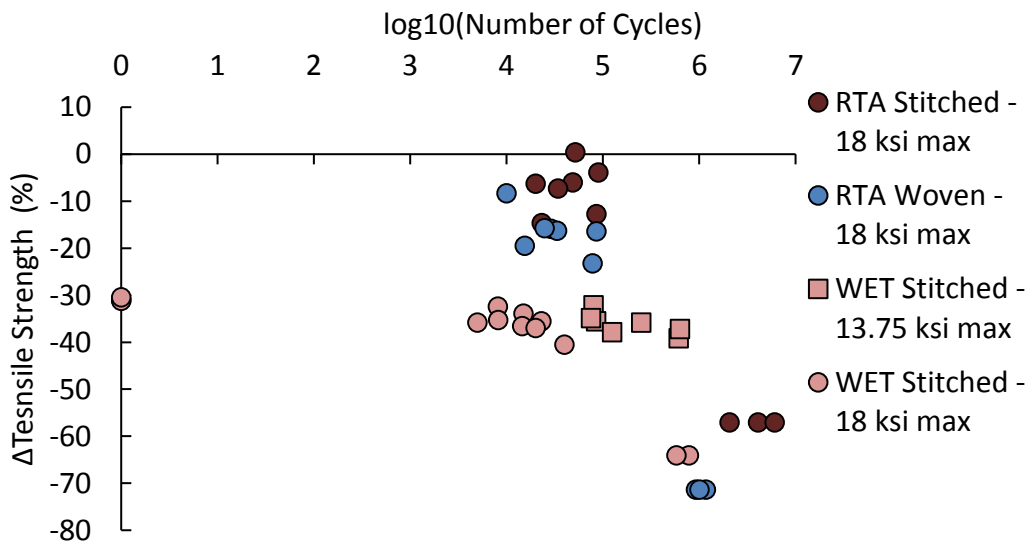


Figure 6-29. Quantification of damage through plotting number of cycles vs. change in tensile strength for RTA and WET samples tested at 13.75 and 18 ksi maximum

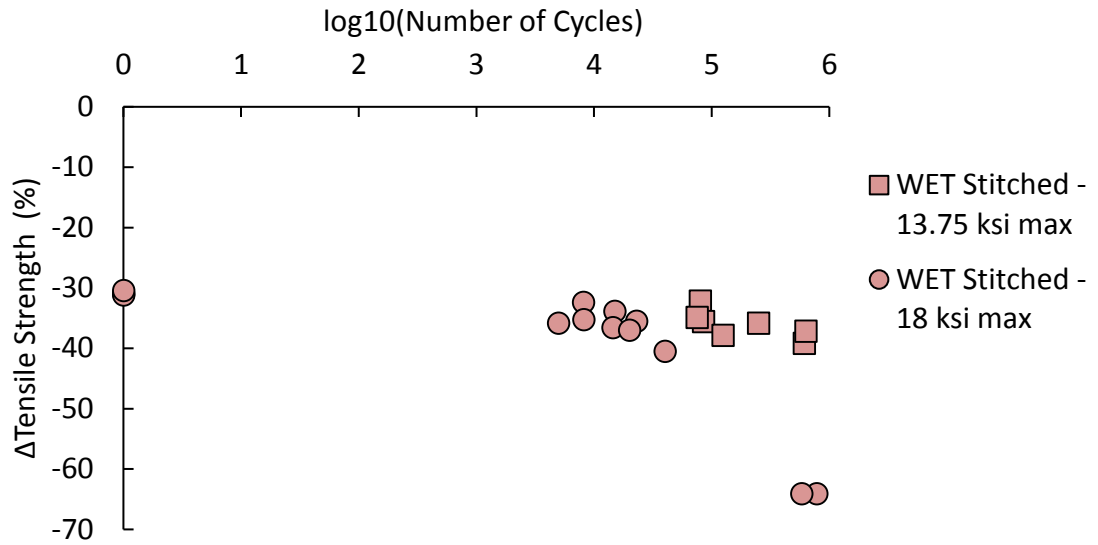


Figure 6-30. Residual Strength change over time for all WET stitched samples; far left baseline strengths apply to both data sets

### Initial Displacement Amplitude Increase

#### RTA

For some RTA tests, extensometers remained attached to samples during fatigue loading. The difference between the maximum and minimum extensometer-measured displacement was automatically calculated and displayed through the INSTRON data acquisition system. The difference of the maximum and minimum displacement was displayed as an amplitude value by the INSTRON user-interface. The reading of the amplitude was recorded every 30 seconds and the results are displayed in Figure 6-31 and Figure 6-32 with comparison in Figure 6-33.

### 13.75 ksi maximum

The 13.75 ksi maximum sample results indicate that there is a difference in each individual sample's change in compliance through the first 15,000 cycles of testing. However, after 15,000 cycles, the stitched samples and the woven samples tend to display nearly the same slightly non-linear shaped curve until measurements were ceased. One of the stitched samples encountered two sudden drops in displacement amplitude and the cause is unknown. It is possible that the extensometer slipped twice while measurements were being recorded.

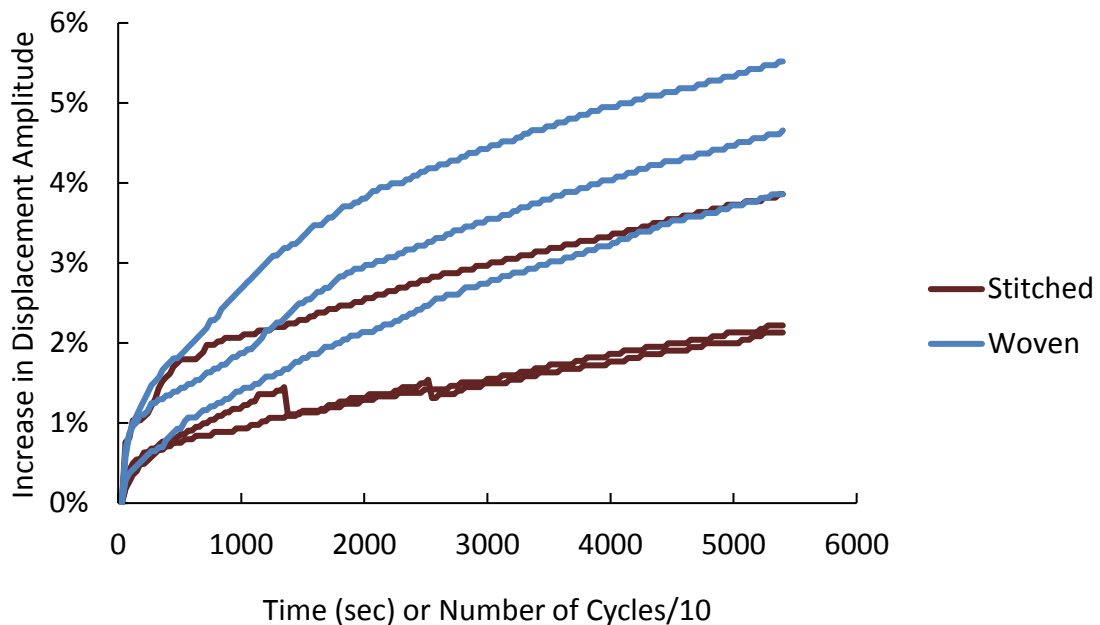


Figure 6-31. Initial increase in extensometer-measured displacement amplitude for RTA woven and stitched data at 13.75 ksi maximum fatigue load

In Figure 6-32, the 18 ksi maximum fatigue load specimens display a highly non-linear region in compliance change. For these specimens, many of the compliance curves were stopped prior to reaching 5,400 cycles because their targeted reduction in modulus before then. One of the stitched samples was recorded all the way until a 14% increase in displacement amplitude as this samples was supposed to undergo fatigue loading until a 16% loss in elastic modulus. Prior data

had shown a roughly 2% difference in change in displacement amplitude and reduction in elastic modulus, although this was not always accurate. The small “jagged edge” in that specimen’s data comes from an early stop when the specimen’s residual elastic modulus was recorded and then re-started due to the modulus loss being well under 16%. As is shown, the residual modulus measurements did not appear to drastically affect the displacement amplitude curve.

Figure 6-33 displays the much slower increase in compliance in the 13.75 ksi maximum samples when juxtaposed with the 18 ksi maximum samples.

*18 ksi maximum*

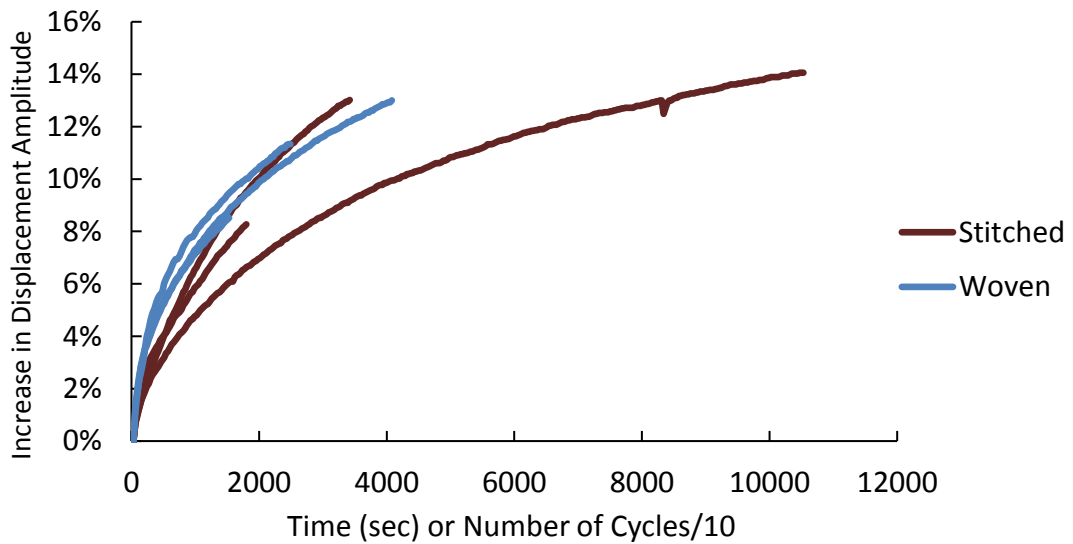


Figure 6-32. Initial increase in extensometer-measured displacement amplitude for RTA woven and stitched data at 18 ksi maximum fatigue load

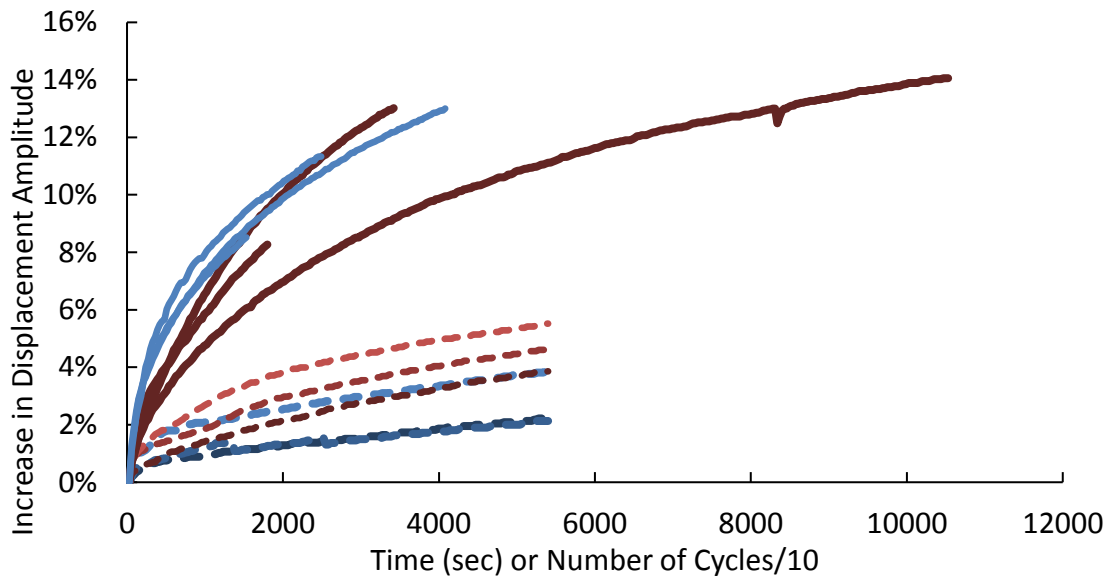


Figure 6-33. Comparison of increase in extensometer-measured displacement amplitude for RTA woven (blue) and stitched data (red) at 13.75 (dashed) and 18 ksi maximum fatigue stresses (solid)

## Forensic Microscopy Analysis

### RTA

#### *Woven – Virgin*

The woven samples showed undulated fibers with voids as described in the previous section. As shown in Figure 6-34, it is important to understand that damage to the composite samples may be caused during the sectioning and polishing process. The figure shows a severed piece from a virgin woven sample's edge that could not have been caused by loading. Several severed edges were noted in woven samples where the 0° fibers dipped downwards and 90° fiber dominated edge region.

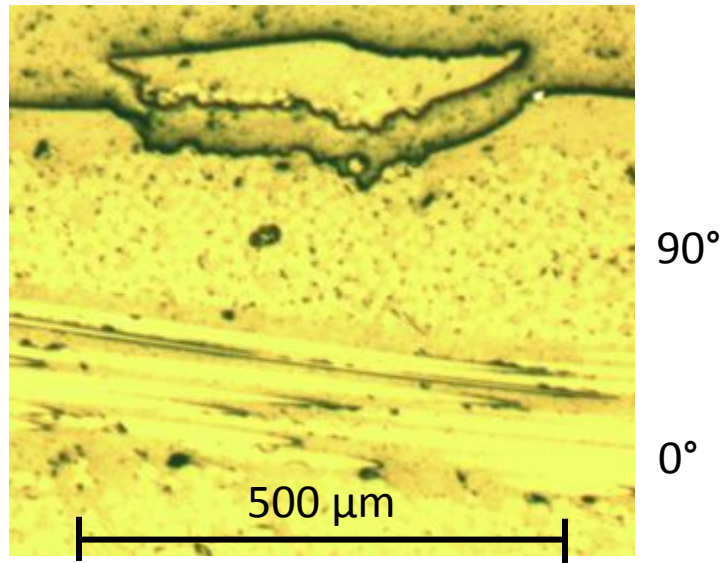


Figure 6-34. Damage to a virgin woven sample's composite edge caused by polishing

***Woven – 13.75 ksi maximum***

Scans shown in the next section will show evidence of tensile cracks as well as delaminations within woven samples tested at 13.75 ksi maximum. Delaminations, especially like those found in close-to-failure specimens, were not found in the damaged samples. However, long void-like shapes were found within several 0° tows, like the one shown in Figure 6-35.

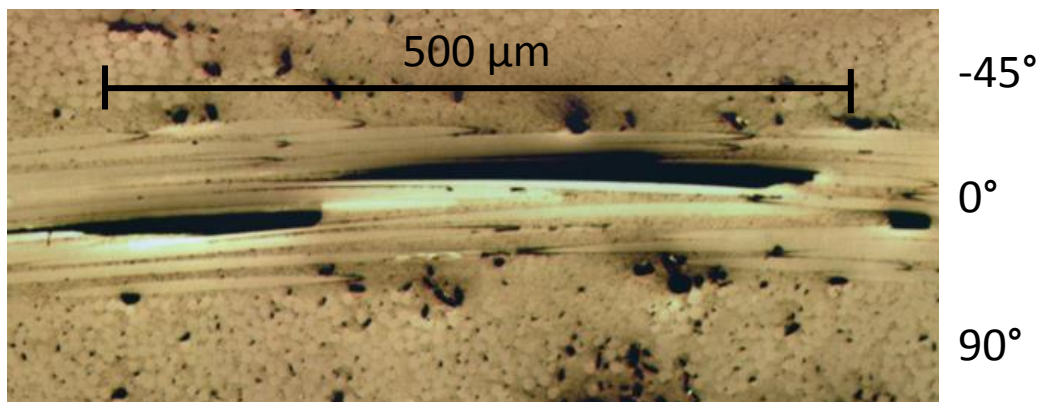


Figure 6-35. Interior void or extended flaw without axial fiber damage inside a 10% modulus reduction 13.75 ksi maximum woven sample

While similar void long black shapes can be found within woven virgin samples, these oblong shapes appear to grow as damage is increased. In the 16% modulus reduction sample shown in Figure 6-36, interlaminar delaminations were not found, but long oblong voids could be found, sometimes with axial fiber breakages near these shapes.

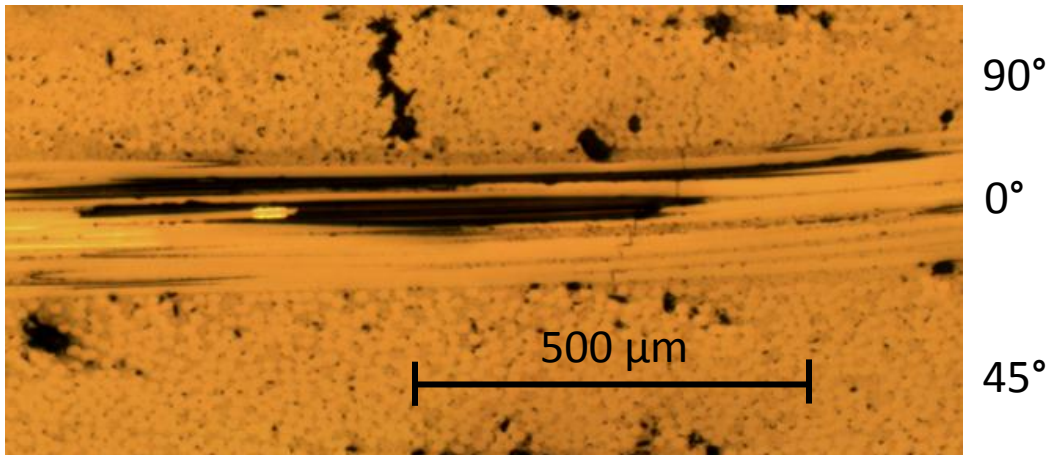


Figure 6-36. Interior void or extended flaw and axial fiber damage within 16% modulus reduction 13.75 ksi maximum woven sample

#### ***Woven – 18 ksi maximum***

Specimens that were loaded to 18 ksi maximum showed an initial development of intralaminar cracks through the thickness of the longitudinal cut. Figure 6-37 shows two of these intralaminar cracks within 90° and 45° plies.

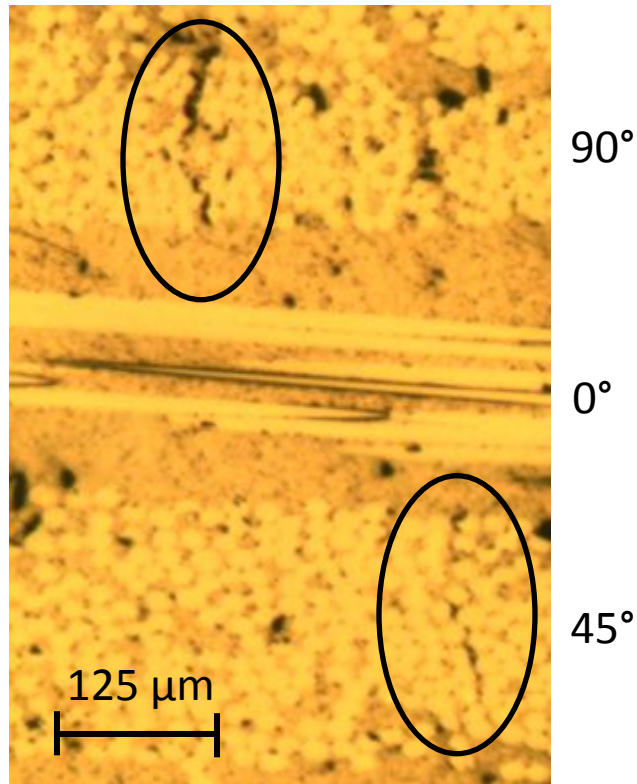


Figure 6-37. Intralaminar cracks (circled) within a woven laminate loaded to 18 ksi maximum fatigue stress with 10% reduction in elastic modulus

The specimen that was tested at 18 ksi maximum until 16% modulus reduction showed a higher density of intralaminar cracks, especially at the outer edges. In the microscopy results, only four or five of these edge cracks can be seen throughout the 1 in. length of the longitudinal section. One of these edge cracks can be viewed in Figure 6-38. While one may expect to see more cracks, the cracking pattern revealed in the woven specimen scans further explain the finding.

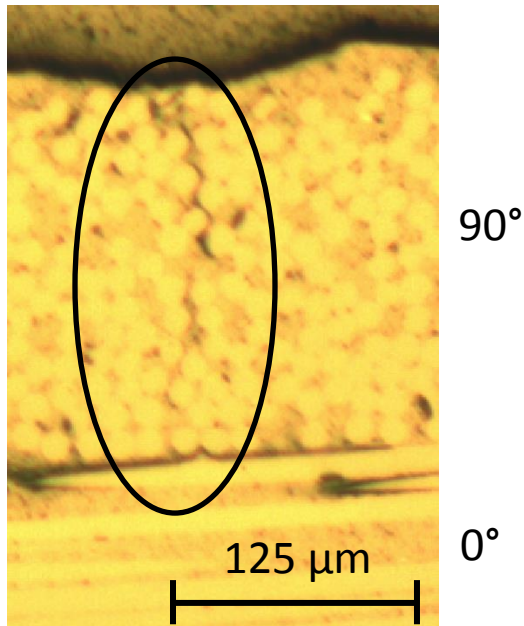


Figure 6-38. One of numerous edge cracks distributed within an 18 ksi maximum, 16% modulus reduction woven sample

One of the failed 18 ksi maximum woven samples was investigated by making a 1 in. longitudinal cut across the critical crack as well as an area a few inches away from the critical crack, but still within the gauge section of the dogbone. The latter micrographs, like the one shown in Figure 6-39, reveals long delaminations between plies connecting with intralaminar cracks to create a network of damage through the thickness of the sample. A similar result can be seen around the critical flaw, shown in Figure 6-40. The major difference between the two figures is that the critical crack micrograph shows fiber failures in the  $0^\circ$  plies, while the non-critical region mostly shows matrix damage with some failed fibers.

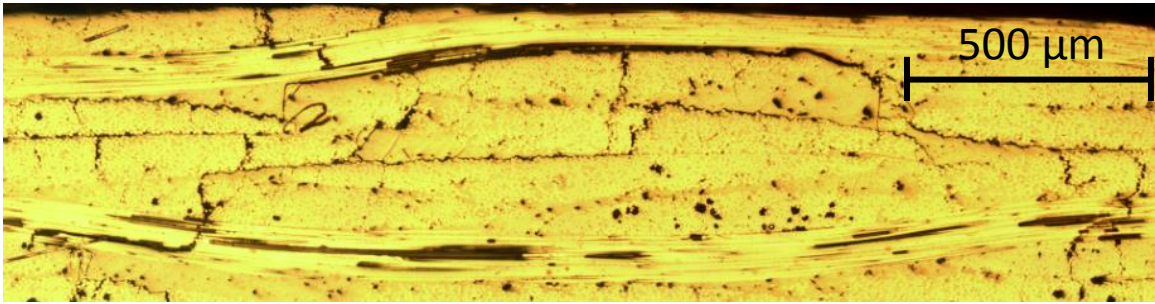


Figure 6-39. Longitudinal cut of 18 ksi maximum failed woven sample taken several inches away from the critical crack

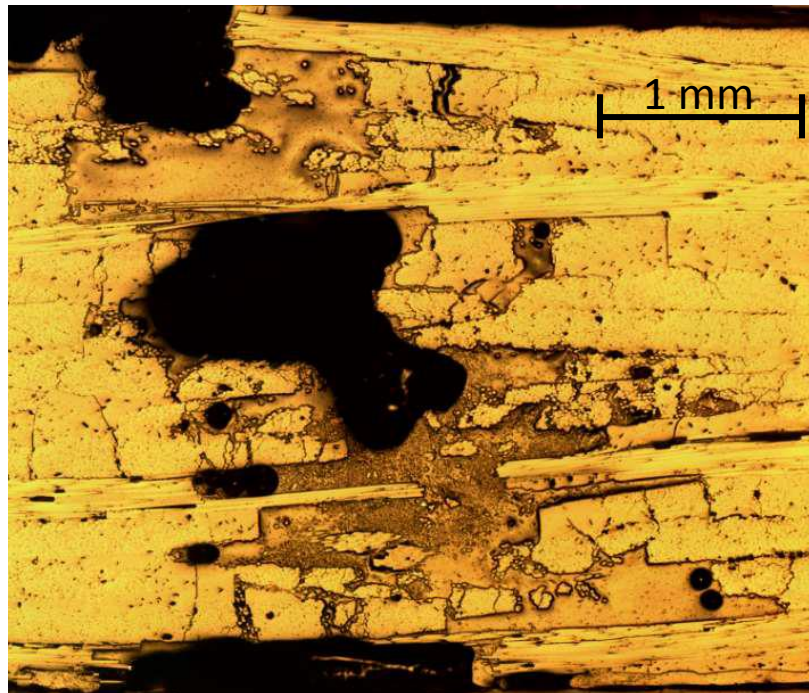


Figure 6-40. Critical flaw in failed 18 ksi maximum woven sample surrounded by intralaminar cracks and delaminations

#### *Woven – 24 ksi maximum*

Compared to the 18 ksi maximum samples, the 24 ksi maximum samples contain a higher number of intralaminar cracks, but fewer interlaminar cracks. Figure 6-41 shows that several intra laminar cracks can form within the same ply just a few fibers away from each other.

Figure 6-42 shows one of the few interlaminar cracks found within the 22 ksi maximum failed sample micrographs.

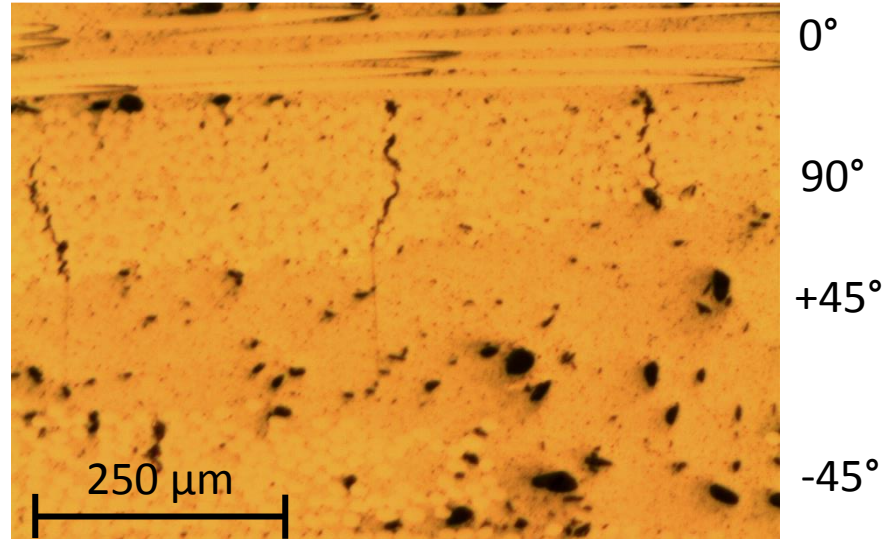


Figure 6-41. Relatively high density of intralaminar cracks found in non-critical flaw of 22 ksi maximum woven failed samples

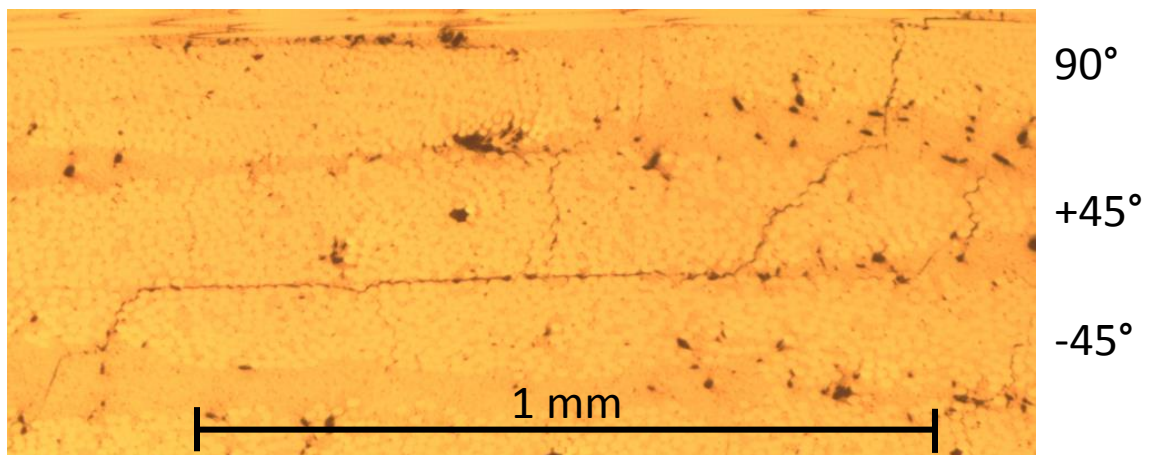


Figure 6-42. Evidence of long interlaminar cracks within non-critical flaw of 22 ksi maximum woven failed samples

### *Stitched – Virgin*

The virgin, unloaded stitched micrographs show the difference between the fibers and the polyester stitches within the material. The stitches are often present in the micrographs within areas of high resin content. Once loaded, these areas are prone to intralaminar-like cracks within the high-resin content region. As shown in Figure 6-43, the stitched material's virgin micrographs showed no evidence of cracks or flaws in resin surrounding the stitches.

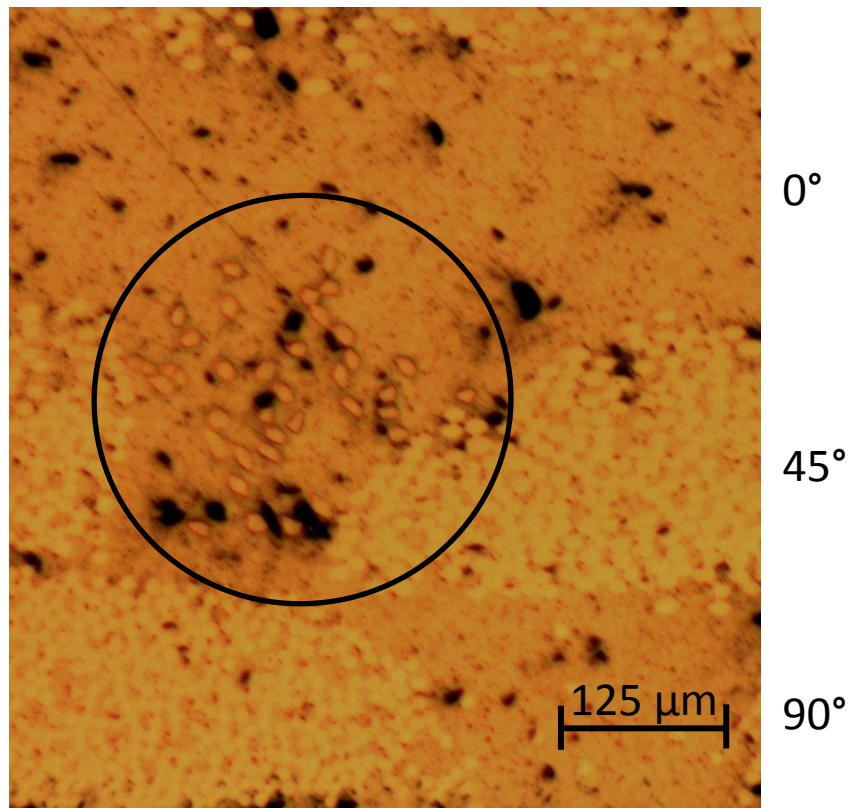


Figure 6-43. Virgin stitched RTA sample highlighting stitches found in micrograph without cracks

### *Stitched – 13.75 ksi maximum*

Figure 6-44 shows the first evidence of damage within the stitched samples. For samples loaded at 13.75 ksi maximum to 10% modulus reduction, dispersed intralaminar cracks can be

found throughout the longitudinal cross-section. Even though the cross-sections are the same size, there are more intralaminar cracks within these stitched samples than the woven samples tested at 13.75 ksi maximum to 10% modulus reduction. Once the stitched samples reach 16% modulus reduction, longer multi-laminar cracks can be found within the cross-section. While some form only through voids, many of these long multi-laminar cracks appear to either propagate to or from stitches, as shown in Figure 6-45. Additionally, evidence of interlaminar cracks is present within specimens tested at 13.75 ksi maximum to 16 % modulus reduction, as shown in Figure 6-46. The presence of interlaminar cracks does not show up in 18 ksi maximum samples until very late in fatigue life, thus the lower stress may allow adequate time for small interlaminar cracks to develop along with the dispersed intralaminar cracks.

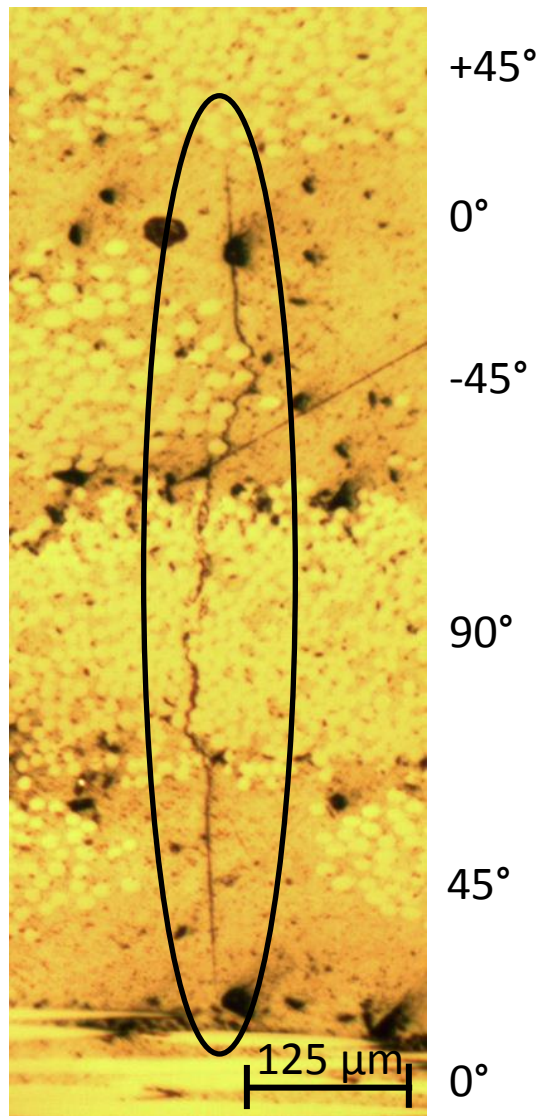


Figure 6-44. Stitched RTA sample loaded at 13.75 ksi maximum to 10% modulus reduction featuring an intralaminar crack in a 90° ply

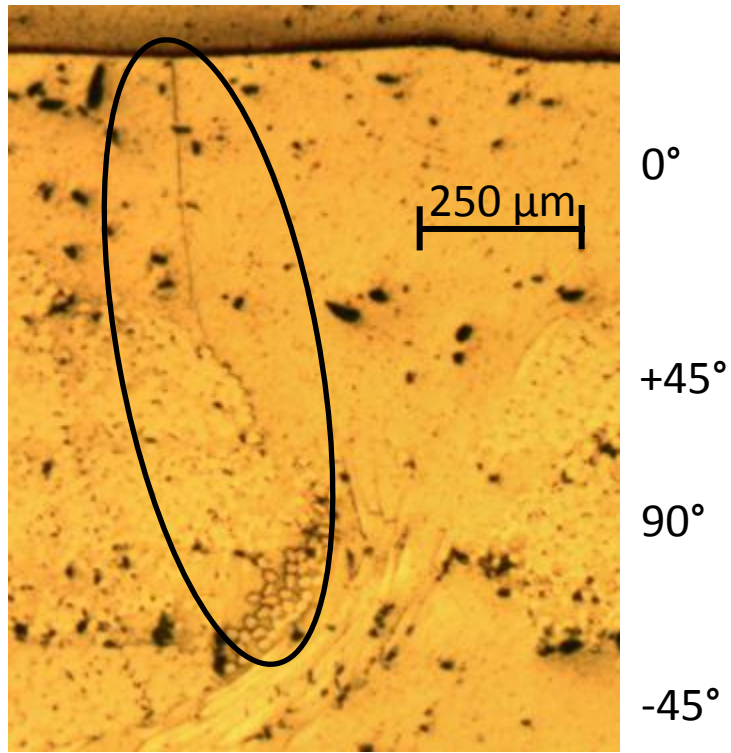


Figure 6-45. Multi-laminar crack involving the specimen edge and internal stitches in 13.75 ksi maximum 16% modulus reduction stitched sample

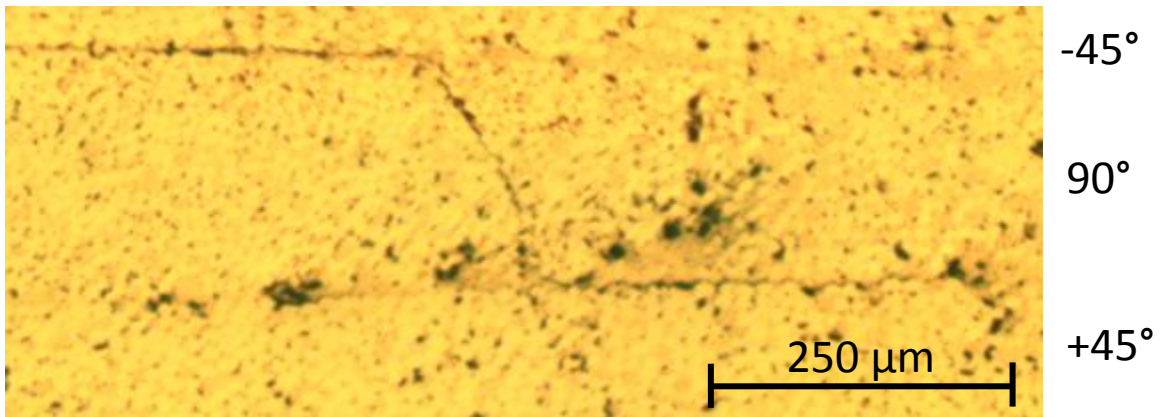


Figure 6-46. Intralaminar crack bridging interlaminar cracks between 90° and 45° plies in stitched sample loaded at 13.75 ksi maximum to 16 % modulus reduction

*Stitched – 18 ksi maximum*

Although interlaminar cracks were not noted to develop prior to 16% modulus reduction, a higher number of intralaminar cracks was noted for 18 ksi maximum stitched samples compared to 13.75 ksi maximum stitched samples. In 10% modulus reduction samples, such as the one shown in Figure 6-47, side-by-side intralaminar cracks were discovered in several locations. While these cracks were not necessarily causally related, the relatively short distance between cracks speaks to the higher density of cracks throughout the 18 ksi maximum samples. In addition, some of the intralaminar cracks, especially the ones found in the resin-rich areas around stitches, were much longer than those found in the 13.75 ksi maximum stitched samples. One of these long cracks is displayed in Figure 6-48.

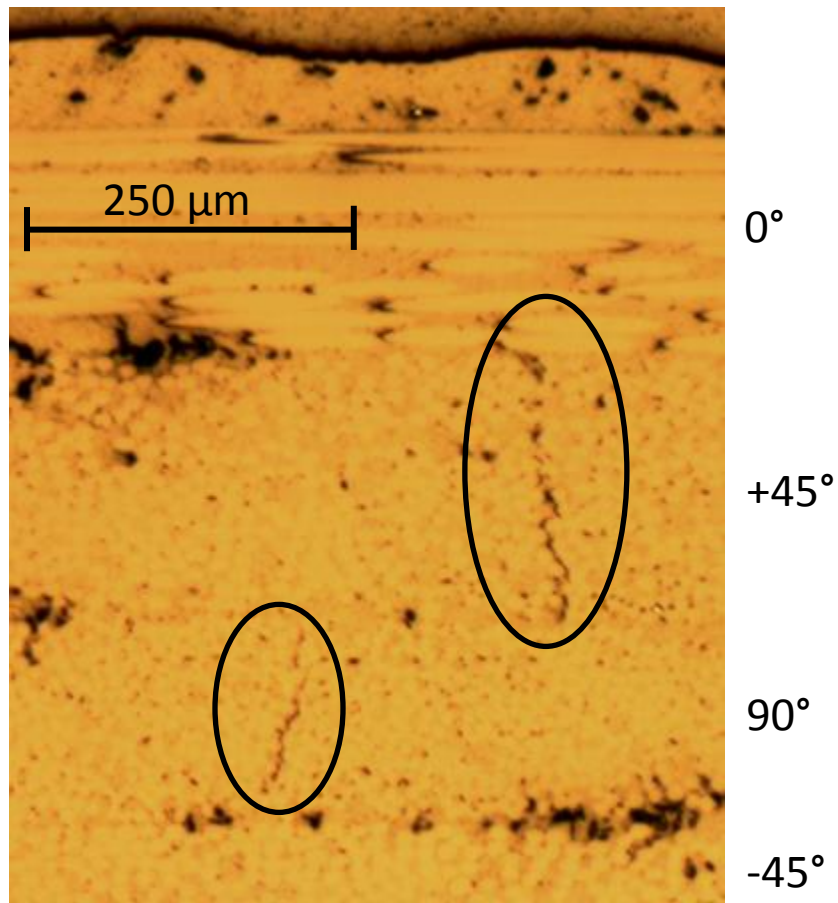


Figure 6-47. Stitched RTA sample loaded at 18 ksi maximum to 10% modulus reduction featuring intralaminar cracks in a 45 and 90° ply

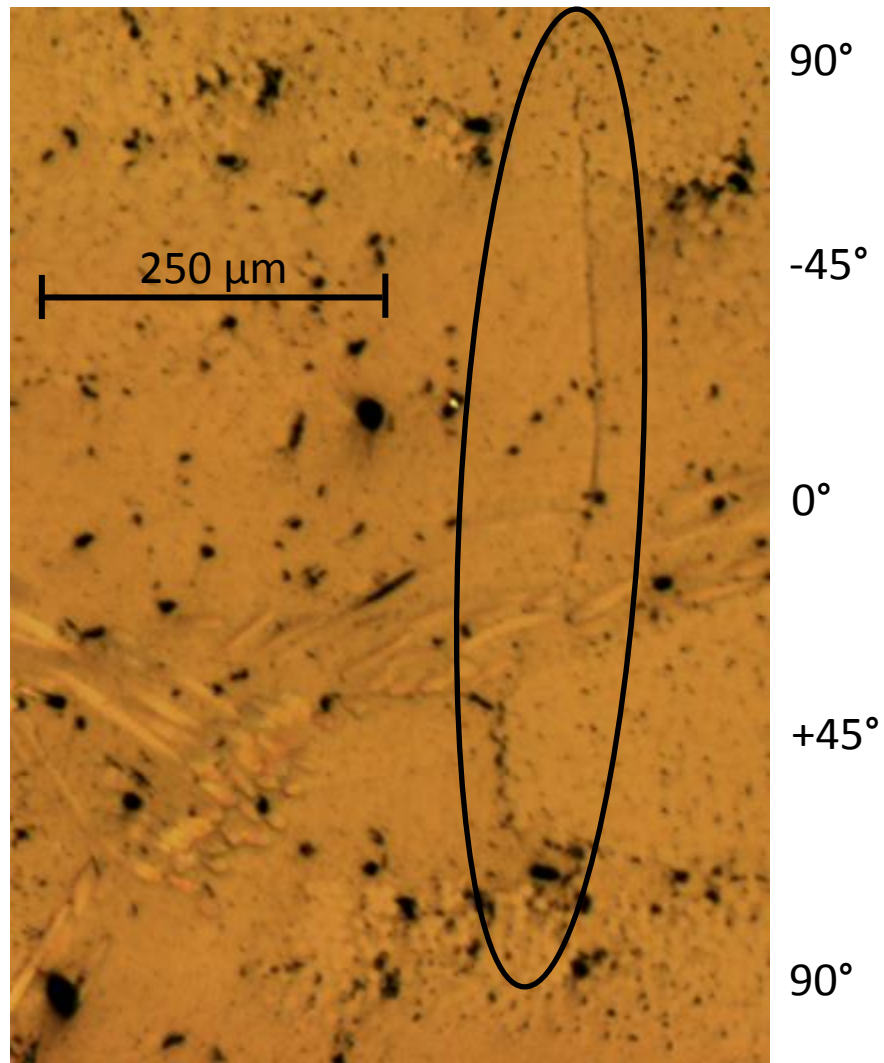


Figure 6-48. Long crack found in resin-rich area around stitches within an 18 ksi maximum stitched sample at 10% modulus reduction

The 18 ksi maximum samples loaded until 16% modulus reduction showed very high densities of intralaminar cracks, but little to no evidence of connecting interlaminar cracks. However, the intralaminar cracks are much wider than in any other reduced modulus specimen studied, as is shown in Figure 6-49. As loading continues past 16% modulus reduction and closer fatigue failure, the density of intralaminar cracks further increase until a critical crack density is reached.

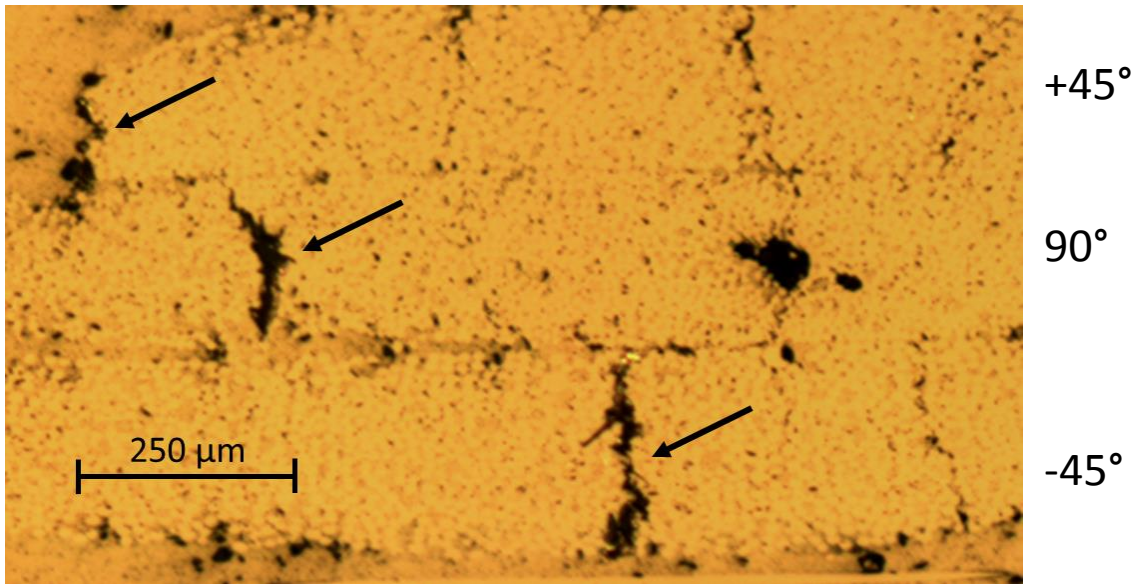


Figure 6-49. Copious wide intralaminar cracks within stitched 18 ksi maximum 16% modulus reduction specimen.

This critical crack density is most likely close to the density displayed in Figure 6-50, which was taken from a failed sample's cross-section several inches away from the critical flaw. In the other non-critical cross-section taken at the failed sample's edge, shown in Figure 6-51, delaminations become apparent. Furthermore, the delaminations appear to be affected by the stitches as a long interlaminar crack maneuvers around stitches. While the crack in the micrograph appears to go around the stitch within the plane of the micrograph, the crack may also penetrate into the plane of the image to go around the stitches as well. Figure 6-52 shows the final stage in fatigue life where the critical flaw is displayed. In the critical flaw, nearly every ply is delaminated from neighboring plies and numerous interlaminar cracks surround the critical flaw.

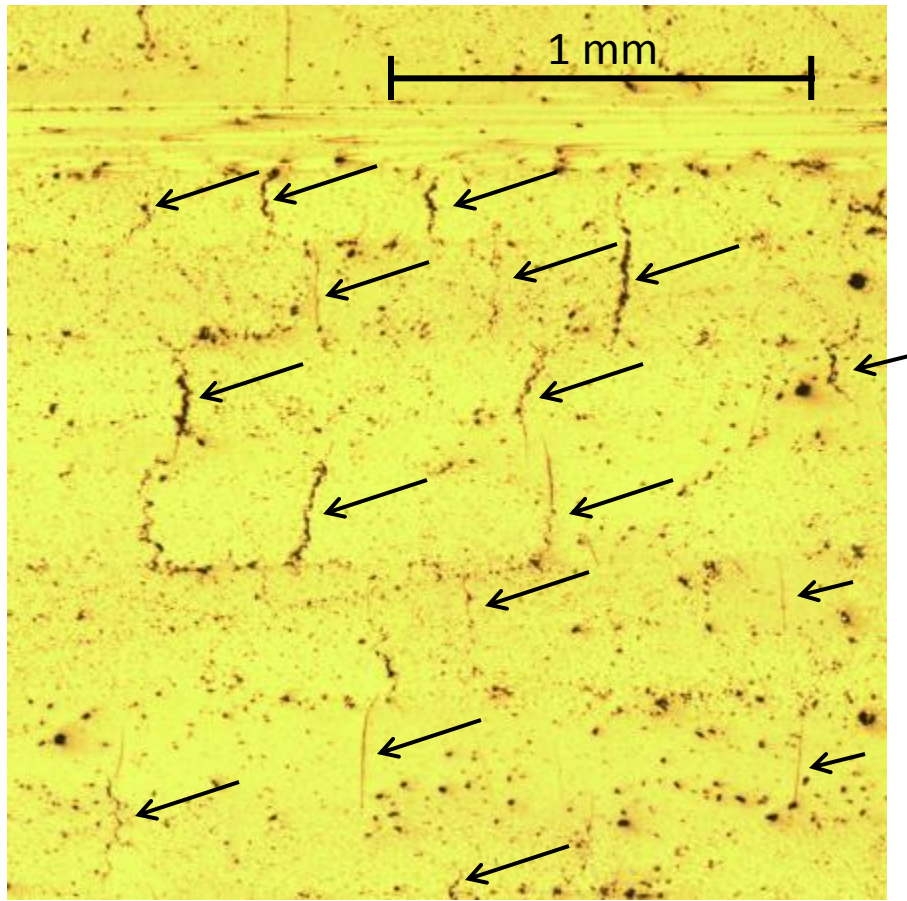
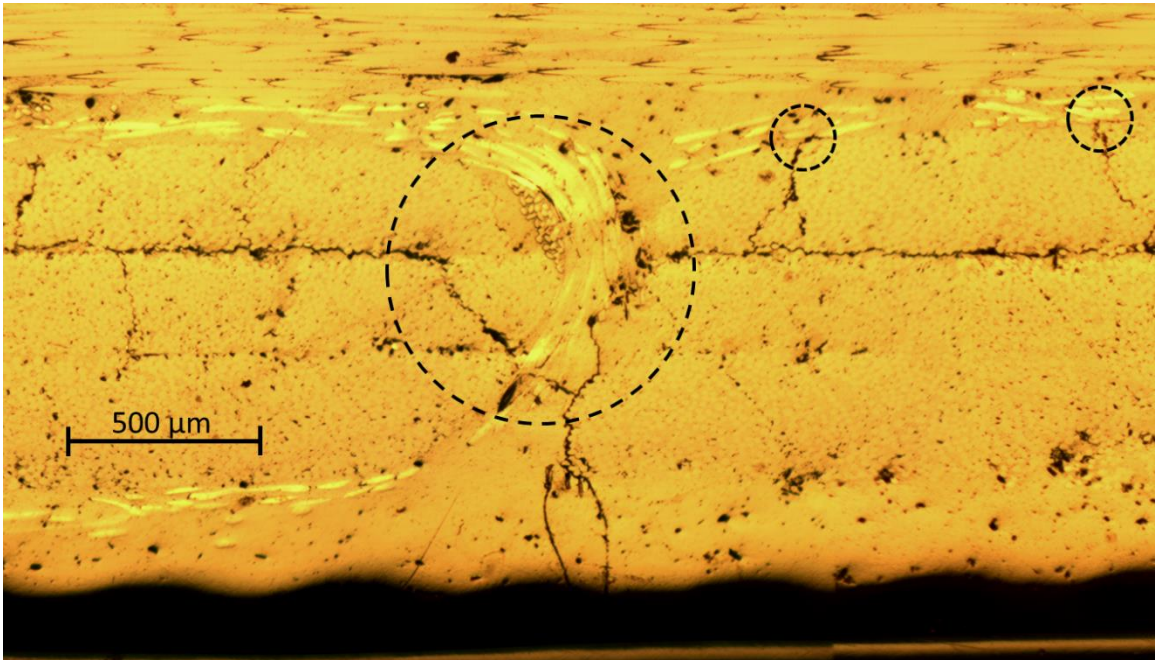


Figure 6-50. Numerous intralaminar cracks within 16 plies of a failed 18 ksi maximum stitched sample (non-critical cross-section)



Surface of Specimen

Figure 6-51. Long interlaminar cracks affected by stitches within 18 ksi maximum stitched sample (non-critical cross section)



Figure 6-52. Critical flaw within 18 ksi maximum failed sample complete with delaminations of nearly every ply and numerous interlaminar cracks

#### *Stitched – 24 ksi maximum*

As shown in Figure 6-53, relatively few intralaminar cracks can be found inside the 24 ksi maximum failed stitched specimen. In the longitudinal cuts taken near the critical flaw and inches away from the critical flaw, the lower plies are delaminated from the upper plies.

Apparently, the stitched specimens' delamination resistance is low at higher stress levels. Further analysis will be determined to conclude if this one specimen was an outlier, or if this is the true trend within the stitched material system.

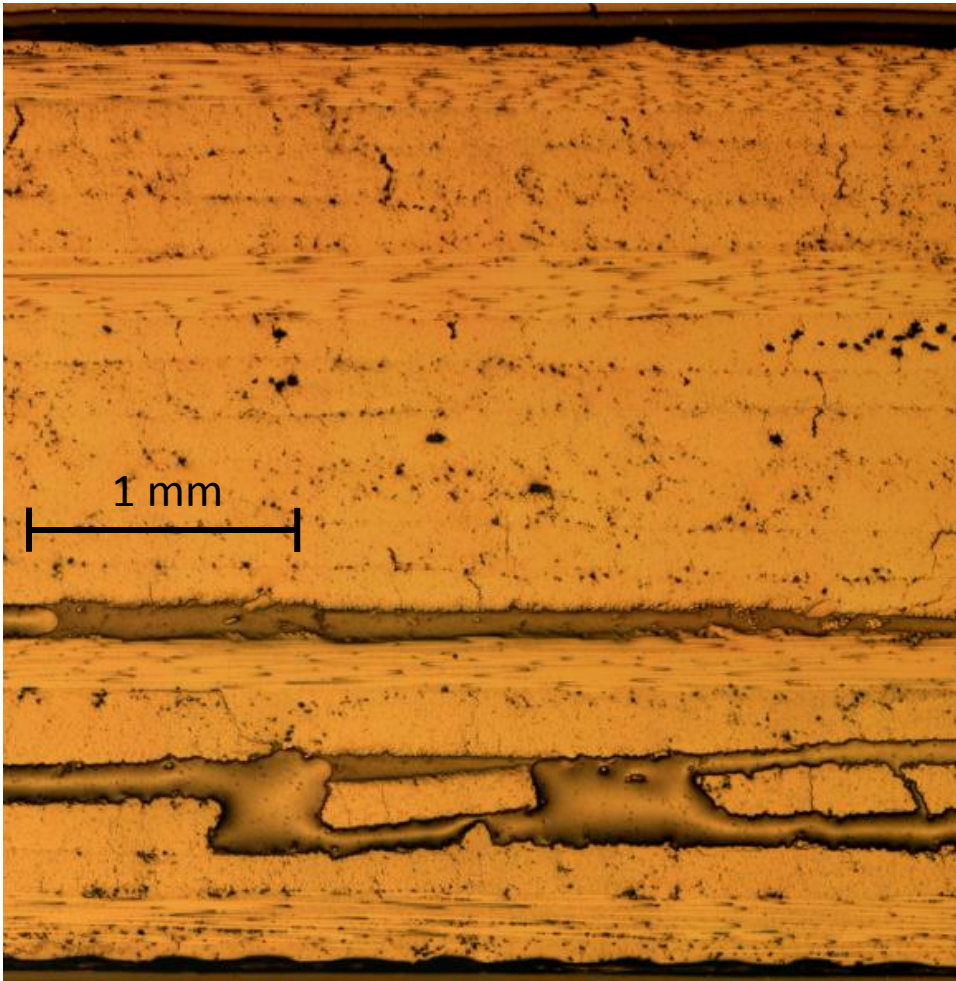


Figure 6-53. Few intralaminar cracks with predominantly interlaminar failure in failed 24 ksi maximum stitched sample

### **Sample Scans**

#### **RTA**

The following scans show macro-scale damage on the surface and within the dogbone samples. A film scanner was used to record images of the translucent specimens while illuminated with a backlight. As a reminder, the dogbones are placed bagged-side down against the scanner and a backlight shines through the tool-side of the sample. All scans of failed samples

showed critical cracks either entirely within the gauge-section, or spanning both the gauge and curved sections of the dogbone. No failures within a half inch of the grip were noted throughout testing. A scan of a larger portion of the dogbone specimen that indicates the orientation of these scans was shown previously in the procedures section. The scans have been enhanced by increasing the contrast and saturation of the images.

### ***Woven – Virgin***

As shown in Figure 6-54, the virgin woven sample does not really show much of anything. However, this figure is important to show in order to understand the extent of damage within the damaged samples as the baseline shows no evidence of macro-scale flaws due to manufacturing or curing.

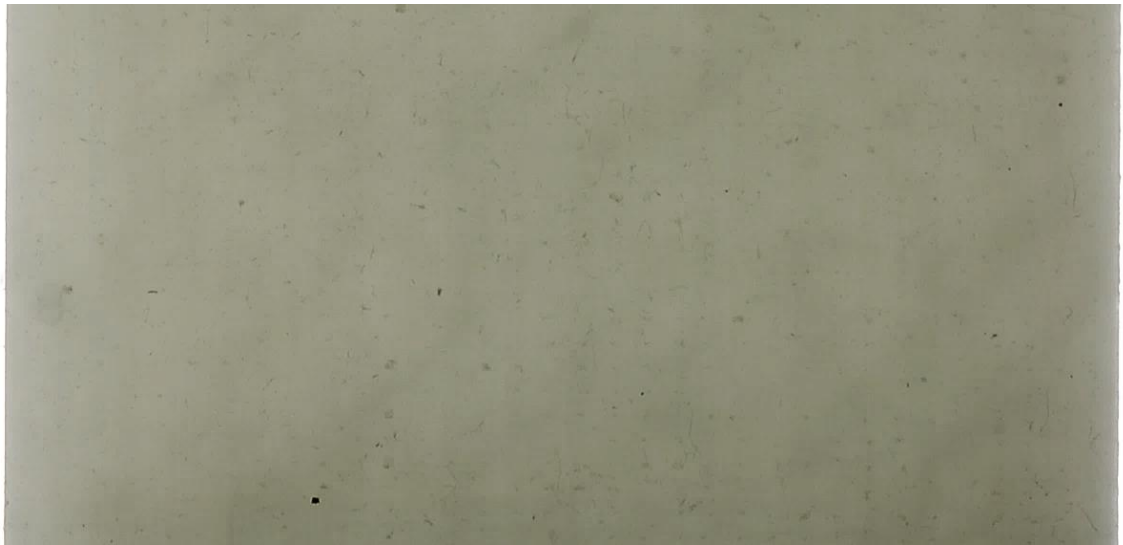


Figure 6-54. Scan of woven virgin sample showing a baseline for comparison with damaged samples.

***Woven – 13.75 ksi maximum***

Figure 6-55 through Figure 6-57 shows the progression of macro-scale damage within the woven specimens loaded at 13.75 ksi maximum. The red lines that appear in the scans are magic marker marks present from specimen manufacturing where the approximate middle of the specimen was marked to aid in the later attachment of the extensometer to the specimen. As is shown in the figures, the development of tensile cracks form in a 45° pattern on the specimen's surface. Additionally, the density of these tensile cracks increases with higher reductions in elastic modulus. Further, dark blotches around the tensile cracks, which are most likely areas of delamination, tend to grow in size with higher reductions in elastic modulus.

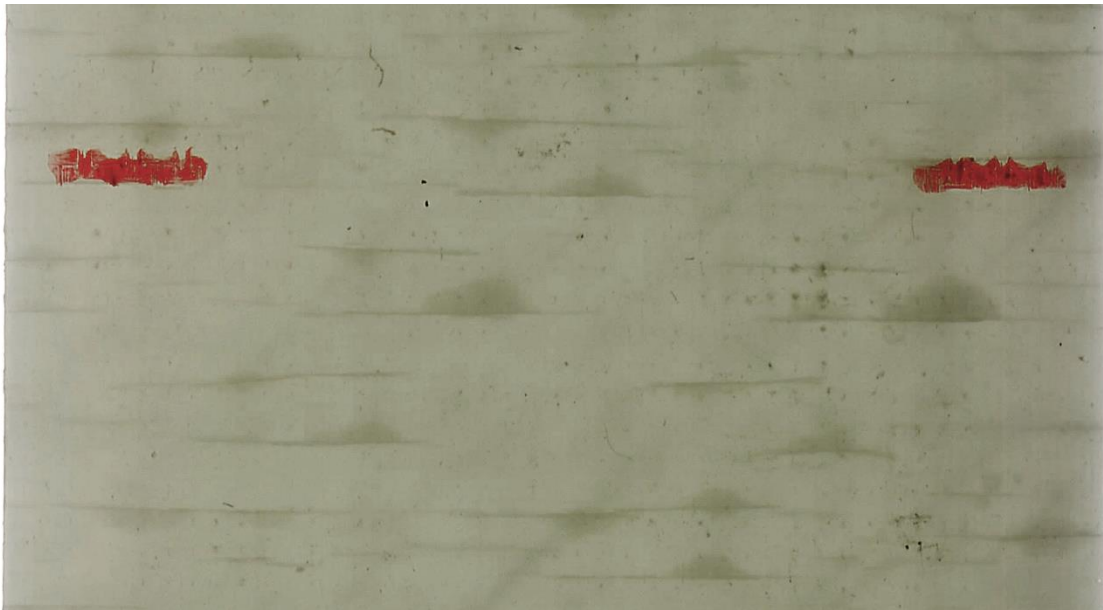


Figure 6-55. Scan of 13.75 ksi maximum woven sample at nearly 10% modulus reduction

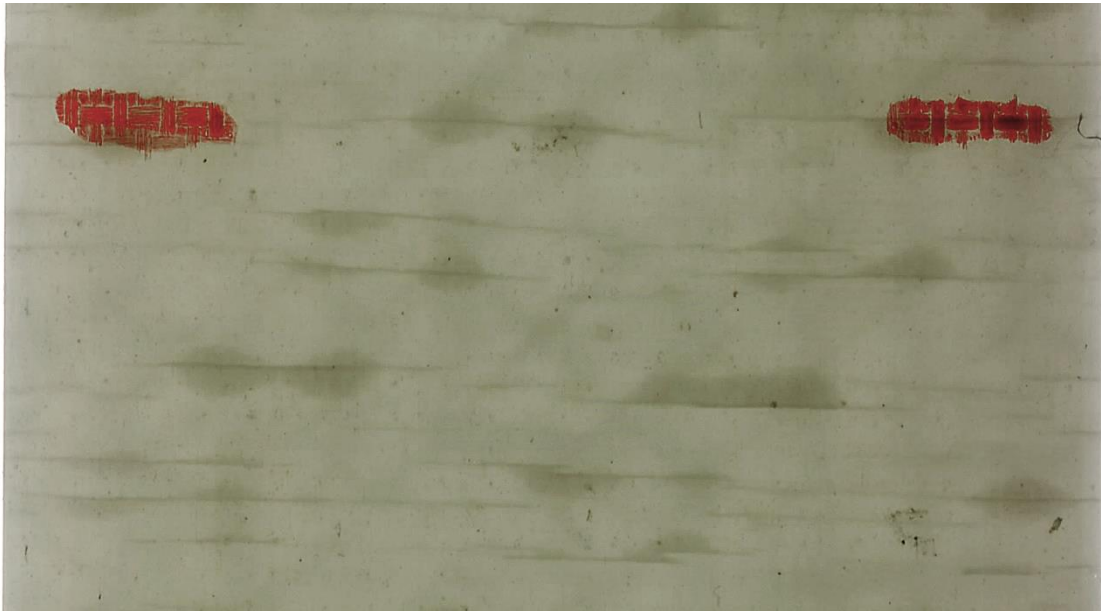


Figure 6-56. Scan of 13.75 ksi maximum woven sample at nearly 13% modulus reduction



Figure 6-57. Scan of 13.75 ksi maximum woven sample at nearly 16% modulus reduction

*Woven – 18 ksi maximum*

Unfortunately, due to a book-keeping error, only the 13% modulus reduction sample was scanned for the woven 18 ksi maximum samples. The one sample scanned shows less evidence of delamination compared to the 13% modulus reduction sample from the 13.75 maximum ksi woven scan. However, the crack density in the 13% modulus reduction sample from the 18 maximum ksi data woven scan is higher than the 13.75 ksi maximum sample. Again, this suggests that delaminations flourish under lower load scenarios, where time allows the delaminations to grow in the presence of less intralaminar cracks.



Figure 6-58. Scan of 18 ksi maximum woven sample at nearly 13% modulus reduction

16% Modulus Reduction

### *Failures*

For the 28.75 ksi, 22 ksi, and 18 ksi maximum failed samples, shown in Figure 6-59, Figure 6-60, and Figure 6-61, respectively, fiber failure in the 0° plies appears to occur around the presence of dense groupings of matrix tensile cracks. The density of these matrix cracks as well as delaminations are much higher than that measured in the 16% modulus reduction cases for either the 13.75 ksi maximum and 18 ksi maximum samples.



Figure 6-59. Scan of critical crack of woven sample failed at 28.75 ksi maximum fatigue stress



Figure 6-60. Scan of critical crack of woven sample failed at 24 ksi maximum fatigue stress



Figure 6-61. Scan of critical crack of woven sample failed at 18 ksi maximum fatigue stress

***Stitched – Virgin***



Figure 6-62. Virgin stitched sample for comparison to damaged samples

***Stitched – 13.75 ksi maximum***

Damaged stitched samples tested at 13.75 ksi maximum are shown in Figure 6-63 to Figure 6-65, which range from 10% to 16% modulus reduction. Delaminations do not appear in these samples. In damaged stitched samples, numerous faint tensile cracks as well as fainter 45° cracks behind the 90° tensile matrix cracks. The density of both types of cracks increase for higher reductions in elastic modulus and the density of tensile cracks in the stitched specimens is higher than the density of tensile cracks in the woven specimens. However, just as the microscopy samples showed, there is no evidence of delaminations in the stitched samples within the scans of the 13.75 ksi maximum samples.



Figure 6-63. Scan of 13.75 ksi maximum stitched sample at nearly 10% modulus reduction



Figure 6-64. Scan of 13.75 ksi maximum stitched sample at nearly 13% modulus reduction



Figure 6-65. Scan of 13.75 ksi maximum stitched sample at nearly 16% modulus reduction

***Stitched – 18 ksi maximum***

Like the woven samples, only the 13% modulus reduction sample was scanned from the stitched 18 ksi maximum group of specimens. This sample is shown in Figure 6-66. Again, similar to the woven samples, the 18 ksi maximum samples have a higher density of matrix cracks compared to the 13.75 ksi maximum stitched sample at the same reduction in elastic modulus. Still no evidence of delamination is present in the 18 ksi maximum stitched sample. The absence of delaminations may have to do with the difference in layup since there are only 45° offsets between adjacent plies, except at the midplane of the composite laminate, whereas there are numerous 90° offsets between adjacent plies in the woven laminate.



Figure 6-66. Scan of 18 ksi maximum stitched sample at nearly 13% modulus reduction

### *Failures*

In all three of the stress levels for stitched sample fatigue failure, shown in Figure 6-67 through Figure 6-69, evidence of a near  $45^\circ$  critical flaw is seen. While this does not necessarily imply a shear-dominated failure as it would in an isotropic material, the angle of the critical flaw does imply that the  $45^\circ$  cracks found in the damaged sample scans play a major role in the failure mechanism of the samples. However, as the load level is decreased, mixing of a  $90^\circ$  critical flaw and a  $45^\circ$  flaw increases. This mix implies that as load decreases, the tensile matrix cracks tend to contribute to the eventual failure of the specimen more so than at higher loads.

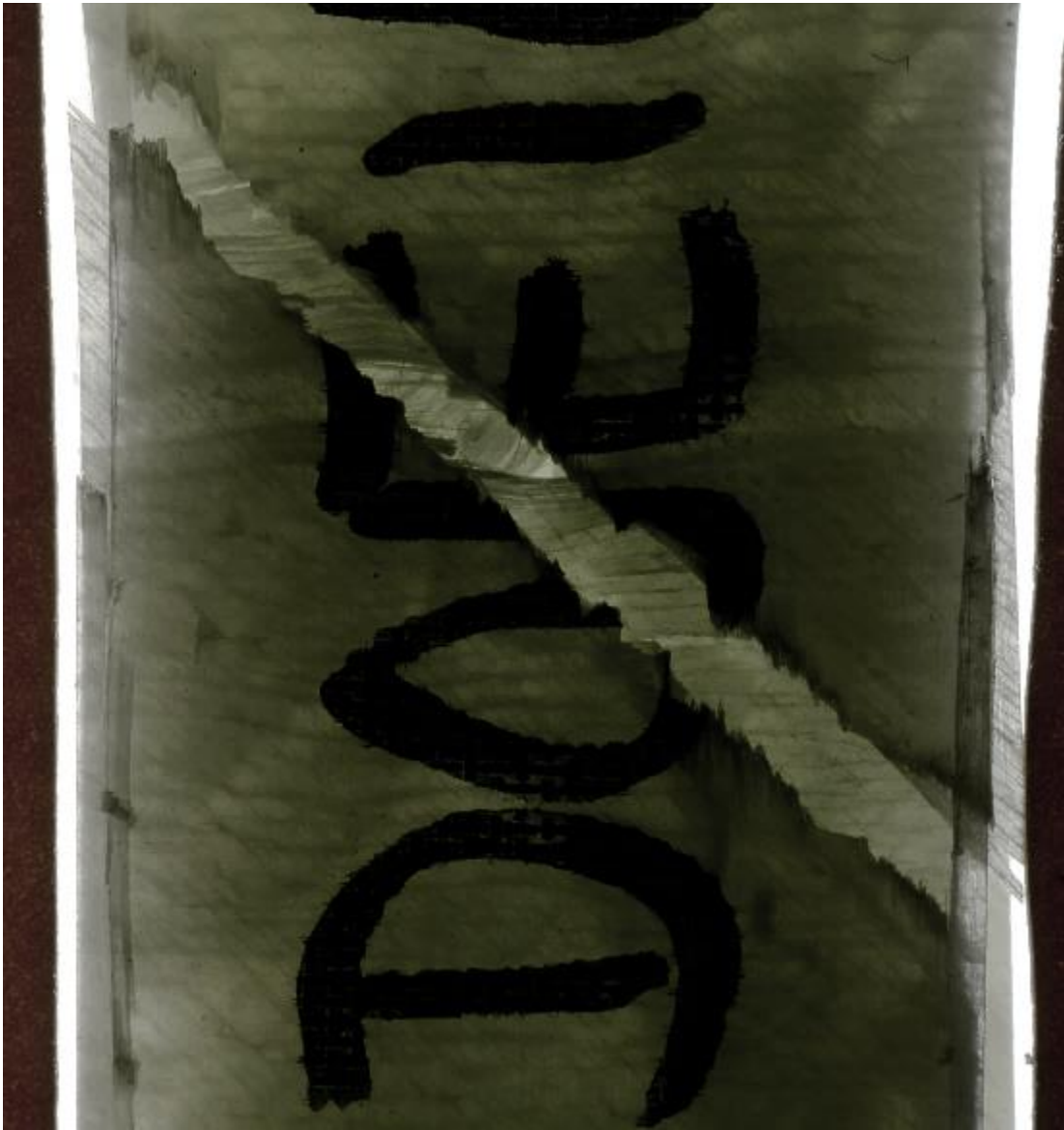


Figure 6-67. Scan of critical crack of stitched sample failed at 28.75 ksi maximum fatigue stress

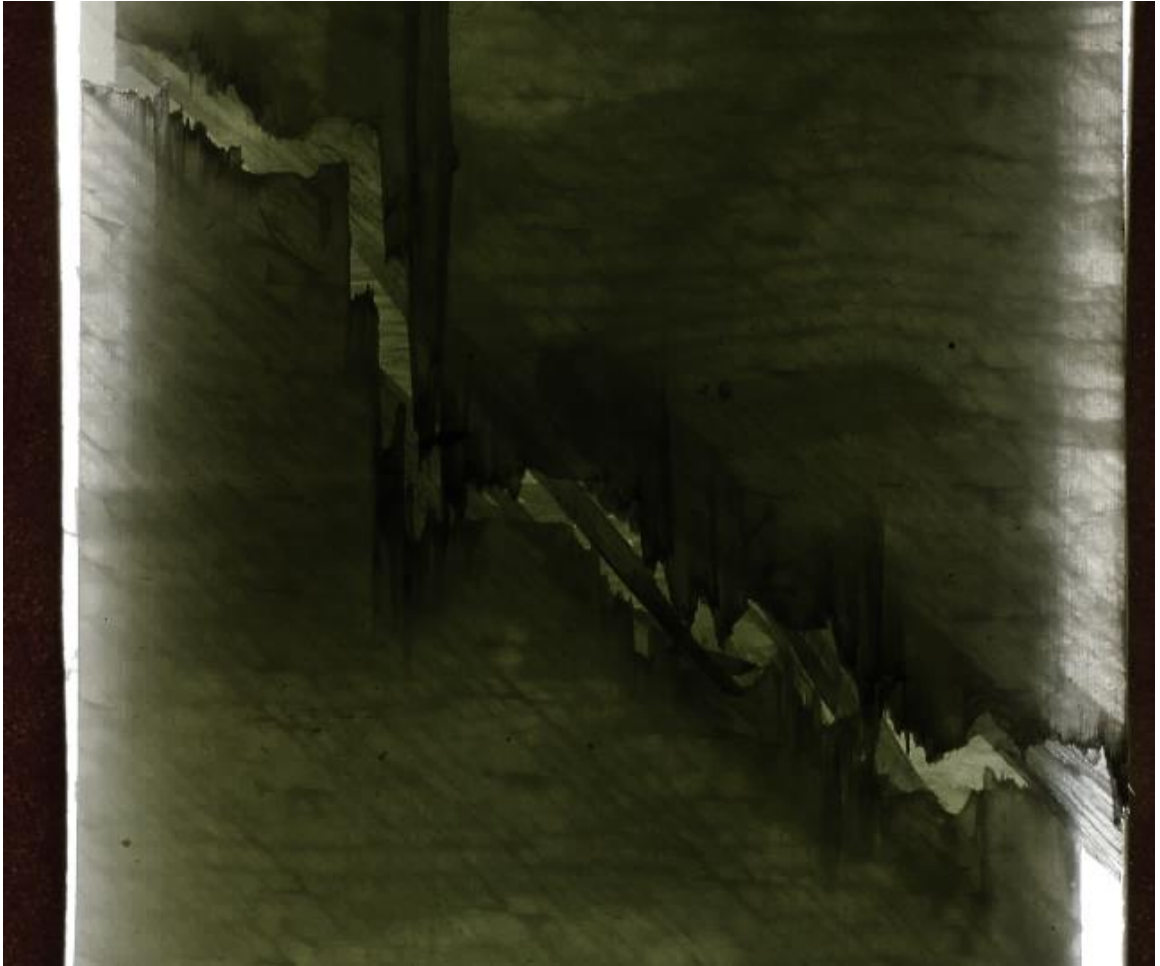


Figure 6-68. Scan of critical crack of stitched sample failed at 24 ksi maximum fatigue stress



Figure 6-69. Scan of critical crack of stitched sample failed at 18 ksi maximum fatigue stress

## **WET**

Contrary to the RTA stitched specimens, it is difficult to discern details about the WET specimens. A handful of WET specimen scans are shown below to demonstrate the lack of information that can be retrieved from these specimens through scanning.

### ***Stitched – WET Virgin***

A scan of a WET conditioned, but unloaded (hence, WET virgin) sample is shown in Figure 6-70. Besides the loss of magic marker during conditioning, not much can be said about the WET virgin sample from the scan alone.



Figure 6-70. Scan of WET conditioned, but unloaded stitched sample without polysulfide edge seals

***Stitched – 13.75 ksi maximum***

Images Figure 6-71 to Figure 6-73 show damage within the 13.75 ksi maximum WET samples tested to 10 to 16% modulus reduction. While faint 90° and 45° cracks are apparent, the polysulfide edge seal and the specimen's loss in transparency makes determining the state of damage within the composite difficult. Additionally, some 0° tows show through the surface, and without microscopy, it is difficult to note whether there is damage within the tow. The same description can be made for the 18 ksi maximum WET samples shown in Figure 6-74 and Figure 6-75. Microscopy could be performed on sectioned WET samples at a later time, but were not as part of this investigation.



Figure 6-71. Scan of WET stitched sample tested to 10% modulus reduction at 13.75 ksi maximum



Figure 6-72. Scan of WET stitched sample tested to 13% modulus reduction at 13.75 ksi maximum



Figure 6-73. Scan of WET stitched sample tested to 16% modulus reduction at 13.75 ksi maximum

*Stitched – 18 ksi maximum*



Figure 6-74. Scan of WET stitched sample tested to 10% modulus reduction at 18 ksi maximum



Figure 6-75. Scan of WET stitched sample tested to 16% modulus reduction at 13.75 ksi maximum

### *Failures*

Figure 6-76 through Figure 6-78 display the scans of the failed WET specimens from 28.75 ksi maximum to 18 ksi maximum fatigue stress. Like the RTA stitched specimens, the progression of decreasing stress levels appears to cause a 45° critical crack to mix with a 90° critical flaw. Although, both 18 ksi specimens failed within the curvature of the dogbone geometry so this observation may not be as clear-cut as the RTA samples. Future microscopy of the WET samples may reveal more information about damage progression and failure in WET stitched samples.



Figure 6-76. Scan of critical crack of WET stitched sample failed at 28.75 ksi maximum fatigue stress



Figure 6-77. Scan of critical crack of WET stitched sample failed at 24 ksi maximum fatigue stress



Figure 6-78. Scan of critical crack of WET stitched sample failed at 18 ksi maximum fatigue stress

## Chapter 7

### Conclusions & Future Work

The major finding from this study was the quantitative differences measured between the commonly used PAC, the QE1203/ST94 stitch-bonded, and the WRE581T/ST94 woven-roving material systems. Both ST94 systems out-performed PAC in terms of fatigue life at several maximum fatigue loads at  $R$  (stress ratio) = 0.1. Additionally, the stitch-bonded material system out-performed the woven roving system in terms of fatigue life at cycle ranges above 10,000 cycles. This trend of stitch-bonded specimens having superior mechanical properties only in longer fatigue tests was also found in the majority of residual modulus and residual strength data sets. Both woven and stitched samples survived ten million cycles at a maximum stress of +13.75 ksi, but failed between one million and seven million cycles at a maximum stress of +18 ksi.

In terms of quasi-static testing, predictions of longitudinal elastic modulus and tensile strength based on a combination of the Halpin-Tsai and Sun-Li models showed promising results. These results at least partially validate the quasi-laminar assumption made to model the in-plane mechanical properties of complex fiber architecture composites. That being said, modulus predictions were more accurate than strength predictions. More accurate predictions of strength require a model that does not rely on the quasi-laminar assumption since the complex architectures play a major role in failure mechanisms.

The fatigue damage and failure mechanisms were documented using film-scanning and panoramic microscopy techniques, which recorded macroscale and microscale damage within the stitch-bonded and woven roving material systems. The film scanning and panoramic

photomicrographs were developed and successfully implemented by modifying experimental ARL procedures used in past projects. These images showed the continual development of intralaminar and interlaminar cracks throughout fatigue life. Both stitched and woven specimens showed signs of interlaminar cracks developing at lower fatigue loads where cracks had more time to develop. However, specimens tested at higher loads were found to have a higher density of intralaminar cracks through the thickness and on the surface of the specimen than those tested at lower loads.

Future predictive models could correlate crack densities and delamination areas to modulus reduction and residual strengths in damaged, fatigue cycled samples. These models could also include material properties, such as void volume fraction and fiber volume fraction, found through methods described in this study. If similar damage mechanisms in specimens occur at different load levels, then extremely long-life fatigue testing (>10M cycles) could be modeled and/or predicted using data from shorter tests completed at an increased maximum load with the same stress ratio.

## Appendix A

### Halpin-Tsai and Sun-Li Model MATLAB Code

```
clear all
clc

%%%%%%%%%%%%%%%%%%%%%%%%%%%%%%%%%%%%%%%%%%%%%%%%%%%%%%%%%%%%%%%%%%%%%%%% Halpin-Tsai %%%%%%%%%
Vf=0.65;
E1f=73e9;
E2f=73e9;
G12f=30e9;
vf=0.28;
Em=3.4e9; %From DMA paper
vm=0.35;
Gm=Em/(2*(1+vm));

XIt=2; %Halpin-Tsai Shape Factors
XIs=1;
ETAt=(E2f-Em)/(E2f+XIt*Em);
ETAs=(G12f-Gm)/(G12f+XIs*Gm);

E1=Vf*E1f+(1-Vf)*Em;
E2=Em*(1+XIt*ETAt*Vf)/(1-ETAt*Vf);
G12=Gm*(1+XIs*ETAs*Vf)/(1-ETAs*Vf);
v12=vf*Vf+vm*(1-Vf);
%%%%%%%%%%%%%%%%%%%%%%%%%%%%%%%%%%%%%%%%%%%%%%%%%%%%%%%%%%%%%%%%%%%%%%%% Halpin-Tsai %%%%%%%%%

%%%%%%%%%%%%%%%%%%%%%%%%%%%%%%%%%%%%%%%%%%%%%%%%%%%%%%%%%%%%%%%%%%%%%%%% CT_Sun %%%%%%%%%
E11 = E1;
E22 = E2;
E33 = E22;
G13 = G12;
v23 = 0.4; %Assumed
v13 = v12;
G23 = E22/(2*(1+v23));

FiberAngle=[0 45 90 -45 -45 90 45 0];
PlyNum=length(FiberAngle);
Layer_Thickness=[1,1,1,1,1,1,1,1];
Total_Thickness=sum(Layer_Thickness);

V=(1+v23)*(1-v23-2*v12^2*E22/E11);
c11=(1-v23^2)*E11/V;
c12=v12*(1+v23)*E22/V;
c13=c12;
c23=(v23+v12^2*E22/E11)*E22/V;
c22=(1-v12^2*E22/E11)*E22/V;
c33=c22;
```

```

c44=G23;
c55=G12;
c66=c55;

C0=[c11,c12,c13,0,0,0;
c12,c22,c23,0,0,0;
c13,c23,c33,0,0,0;
0,0,0,c44,0,0;
0,0,0,0,c55,0;
0,0,0,0,0,c66];

a=0;b=0;c=0;

for k=1:PlyNum

    theta=FiberAngle(k)*pi/180;
    vk=Layer_Thickness(k)/Total_Thickness;

    m=cos(theta);
    n=sin(theta);

    T_s=[m^2, n^2, 0,0,0,2*m*n;
n^2,m^2,0,0,0,-2*m*n;
0,0,1,0,0,0;
0,0,0,m,-n,0;
0,0,0,n,m,0;
-m*n,m*n,0,0,0,(m^2-n^2)];
    T_e=[m^2,n^2,0,0,0,m*n; % w.r.t. engineering strain
n^2,m^2,0,0,0,-m*n;
0,0,1,0,0,0;
0,0,0,m,-n,0;
0,0,0,n,m,0;
-2*m*n,2*m*n,0,0,0,(m^2-n^2)];
    C=inv(T_s)*C0*T_e;

    delta_k=C(4,4)*C(5,5)-(C(4,5))^2;
    a=a+vk*C(4,4)/delta_k;
    b=b+vk*C(5,5)/delta_k;
    c=c+vk*C(4,5)/delta_k;

end %Just for calculation of delta

delta=a*b-c^2;

%The following is for the calculation of Cij

C_bar=[0,0,0,0,0,0;
0,0,0,0,0,0;
0,0,0,0,0,0;
0,0,0,0,0,0;
0,0,0,0,0,0;
0,0,0,0,0,0];

```

```

for k=1:PlyNum

    theta=FiberAngle(k)*pi/180;
    vk=Layer_Thickness(k)/Total_Thickness;

    m=cos(theta);
    n=sin(theta);

    T_s=[m^2, n^2, 0,0,0,2*m*n;
         n^2,m^2,0,0,0,-2*m*n;
         0,0,1,0,0,0;
         0,0,0,m,-n,0;
         0,0,0,n,m,0;
         -m*n,m*n,0,0,0,(m^2-n^2)];
    T_e=[m^2,n^2,0,0,0,m*n;
         n^2,m^2,0,0,0,-m*n;
         0,0,1,0,0,0;
         0,0,0,m,-n,0;
         0,0,0,n,m,0;
         -2*m*n,2*m*n,0,0,0,(m^2-n^2)];

    C=inv(T_s)*C0*T_e;

    delta_k=C(4,4)*C(5,5)-(C(4,5))^2;

    C_bar(1,1)=C_bar(1,1)+vk*C(1,1);
    C_bar(1,2)=C_bar(1,2)+vk*C(1,2);
    C_bar(1,3)=C_bar(1,3)+vk*C(1,3);
    C_bar(1,6)=C_bar(1,6)+vk*C(1,6);

    C_bar(2,1)=C_bar(1,2);
    C_bar(2,2)=C_bar(2,2)+vk*C(2,2);
    C_bar(2,3)=C_bar(2,3)+vk*C(2,3);
    C_bar(2,6)=C_bar(2,6)+vk*C(2,6);

    C_bar(3,1)=C_bar(1,3);
    C_bar(3,2)=C_bar(2,3);
    C_bar(3,3)=C_bar(3,3)+vk*C(3,3);
    C_bar(3,6)=C_bar(3,6)+vk*C(3,6);

    C_bar(6,1)=C_bar(1,6);
    C_bar(6,2)=C_bar(2,6);
    C_bar(6,3)=C_bar(3,6);
    C_bar(6,6)=C_bar(6,6)+vk*C(6,6);

    C_bar(4,4)=C_bar(4,4)+vk*C(4,4)/delta_k/delta;
    C_bar(4,5)=C_bar(4,5)+vk*C(4,5)/delta_k/delta;
    C_bar(5,4)=C_bar(4,5);
    C_bar(5,5)=C_bar(5,5)+vk*C(5,5)/delta_k/delta;

end

```

```

C_bar
S_bar=inv(C_bar)

E11c=1/S_bar(1,1);
E22c=1/S_bar(2,2);
E33c=1/S_bar(3,3);
G12c=1/S_bar(6,6);
G13c=1/S_bar(5,5);
G23c=1/S_bar(4,4);
v12c=-S_bar(2,1)*E11c;
v13c=-S_bar(3,1)*E11c;
v23c=-S_bar(3,2)*E22c;

format short g
nineprops=[E11c,E22c,E33c,G12c,G13c,G23c,v12c,v13c,v23c];

%%%%%%%%%%%%%%%%%%%%%%%%%%%%%%%%%%%%%%%%%%%%%%%%%%%%%%%%%%%%%%%%%%%%%%%% CT_Sun %%%%%%%%%%%%%%%%%%%%%%%%%%%%%%%%%%%%%%%%%%%%%%%%%%%%%%%%%%%%%%%%%%%%%%%%%

%%%%%%%%%%%%%%%%%%%%%%%%%%%%%%%%%%%%%%%%%%%%%%%%%%%%%%%%%%%%%%%%%%%%%%%% Table Formatting %%%%%%%%%%%%%%%%%%%%%%%%%%%%%%%%%%%%%%%%%%%%%%%%%%%%%%%%%%%%%%%%%%%%%%%%%

nineprops(1:6)=nineprops(1:6)/6894.76;
nineprops

predicted=[nineprops(1),nineprops(2),nineprops(4)];
measured=[2.75e6,2.74e6,1.28e6];
for q=1:3
error(1,q)=(predicted(q)-measured(q))/measured(q);
end

E11c=[nineprops(1);measured(1);error(1)];
E22c=[nineprops(2);measured(2);error(2)];
G12c=[nineprops(4);measured(3);error(3)];

titles = {'Predicted';'Measured';'Error'};
StitchedTable = table(E11c,E22c,G12c,'RowNames',titles)

%%%%%%%%%%%%%%%%%%%%%%%%%%%%%%%%%%%%%%%%%%%%%%%%%%%%%%%%%%%%%%%%%%%%%%%% Table Formatting %%%%%%%%%%%%%%%%%%%%%%%%%%%%%%%%%%%%%%%%%%%%%%%%%%%%%%%%%%%%%%%%%%%%%%%%%

```

## Appendix B

### Ply Discount Strength Prediction MATLAB Code

```

clear all
clc
format shortE

%Input Material Properties from File
filename = 'inputpropertiesARLW16';
delimiterIn = ' ';
headerlinesIn = 1;
a = importdata(filename,delimiterIn,headerlinesIn);
A=a.data;

%Input Ply Details
filename = 'inputpliesARLW16';
delimiterIn = ' ';
headerlinesIn = 1;
b = importdata(filename,delimiterIn,headerlinesIn);
B=b.data; %Ply Details as numbers (1 for CF, 2 for GF)

%External Effects Input
filename = 'inputexternalARL';
delimiterIn = ' ';
headerlinesIn = 1;
c = importdata(filename,delimiterIn,headerlinesIn);
C=c.data;

%Set 7 Properties in order for each ply
NPLY = size(B,1);
for k=1:NPLY
    j=B(k,2); %Material Check
    v21(1,k)=A(j,2)*A(j,3)/A(j,1);
    sevenprop(k,:)=
[B(k,1),B(k,3),A(j,1),A(j,2),A(j,3),v21(1,k),A(j,4),B(k,4)];

    ALPHA12(k,:)= [A(j,5),A(j,6),0];
    BETA12(k,:)= [A(j,7),A(j,8),0];
end

format shorte

X = array2table(sevenprop,'VariableNames',{'Ply' 'Angle' 'E1' 'E2'
'V12' 'V21' 'G12' 'thck'})

%Part B - Z Values
format shortg
z0=sum(sevenprop(:,8))/2;

```

```

thck = sevenprop(:,8);
thckcount = 0;
z0=sum(thck)/2;
z(1)=-1*z0;
for (i=1:NPLY)
    thckcount=thckcount+thck(i,1);
    z(i+1,1)=-z0+thckcount;
end

for(w=1:NPLY+1)
    fprintf('Z(%d) = %e\n',[[w'],[z(w)']])
end

%Beginning of Hw2,
fprintf(' \n');
fprintf('Homework 2\n');
fprintf(' \n');

S=zeros(3,3,NPLY);

for (kk=1:NPLY)
    S(1,1,kk)=1/sevenprop(kk,3);
    S(2,2,kk)=1/sevenprop(kk,4);
    S(2,1,kk)=-sevenprop(kk,5)/sevenprop(kk,3);
    S(1,2,kk)=-sevenprop(kk,6)/sevenprop(kk,4);
    S(3,3,kk)=1/sevenprop(kk,7);
end

R=[1 0 0;0 1 0;0 0 2]; %Create Reuter's matrix
Rinv=inv(R); %Create inverse Reuter's matrix

Tsig=(zeros(3,3,NPLY)); %Create Tsig matrix
for (jj=1:NPLY)
    m=cosd(sevenprop(jj,2));
    n=sind(sevenprop(jj,2));
    Tsig(1,1,jj)=(m^2);
    Tsig(2,2,jj)=(m^2);
    Tsig(3,3,jj)=(m^2)-(n^2);
    Tsig(1,2,jj)=(n^2);
    Tsig(2,1,jj)=(n^2);
    Tsig(1,3,jj)=(2*m*n);
    Tsig(3,1,jj)=(-m*n);
    Tsig(2,3,jj)=(-2*m*n);
    Tsig(3,2,jj)=(m*n);

    Tsiginv(:, :, jj)=inv(Tsig(:, :, jj)); %Create Tsig inverse matrix
end

for (ii=1:NPLY) %Create Sbar, Qbar, and Q from S matrix
    Sbar(:, :, ii)=R*Tsiginv(:, :, ii)*Rinv*S(:, :, ii)*Tsig(:, :, ii);
    Qbar(:, :, ii)=inv(Sbar(:, :, ii));

```

```

        Q(:, :, ii)=inv(S(:, :, ii));
end

for (mm=1:NPLY)
    fprintf('Q Matrix for Lamina %d',[mm'])
        Q(:, :, mm)
    fprintf('Qbar Matrix for Lamina %d (%d)
Degrees',[mm';sevenprop(mm,2)'])
        Qbar(:, :, mm)
    fprintf('S Matrix for Lamina %d',[mm'])
        S(:, :, mm)
    fprintf('Sbar Matrix for Lamina %d (%d)
Degrees',[mm';sevenprop(mm,2)'])
        Sbar(:, :, mm)
end

disp('Homework 3')
format short e

%Form A matrix
Amatrix=zeros(3);
for (aa=1:3) %Fill Row of A Matrix
    for (aaa=1:3) %Fill Columns of A Matrix
        for (aaaa=1:NPLY) %Sum Counter
            Amatrix(aa, aaa)= Amatrix(aa, aaa)+
(Qbar(aa, aaa, aaaa)*(z(aaaa+1)-z(aaaa)));
        end
    end
end
Amatrix

%Form B matrix
Bmatrix=zeros(3);
for (bb=1:3) %Fill Row of B Matrix
    for (bbb=1:3) %Fill Columns of B Matrix
        for (bbbb=1:NPLY) %Sum Counter
            Bmatrix(bb, bbb)= Bmatrix(bb, bbb)+
0.5*(Qbar(bb, bbb, bbbb)*( (z(bbbb+1) )^2-(z(bbbb) )^2));
        end
    end
end
Bmatrix

%Form D matrix
Dmatrix=zeros(3);
for (dd=1:3) %Fill Row of D Matrix
    for (ddd=1:3) %Fill Columns of D Matrix
        for (dddd=1:NPLY) %Sum Counter
            Dmatrix(dd, ddd)=
Dmatrix(dd, ddd)+(1/3)*(Qbar(dd, ddd, dddd)*( (z(dddd+1) )^3-
(z(dddd) )^3));

```

```

        end
    end
end
Dmatrix

ABDmatrix(1:3,1:3) = Amatrix;
ABDmatrix(4:6,1:3) = Bmatrix;
ABDmatrix(1:3,4:6) = Bmatrix;
ABDmatrix(4:6,4:6) = Dmatrix;
ABDmatrix
abcd_matrix = inv(ABDmatrix)

disp('Problem 2')
D11=ABDmatrix(4,4)
D22=ABDmatrix(5,5)

disp('Problem 3')
amatrix=abcd_matrix(1:3,1:3);

nineprop(1)=1/(amatrix(1,1)*(z(NPLY+1)-z(1)));
nineprop(2)=1/(amatrix(2,2)*(z(NPLY+1)-z(1)));
nineprop(3)=1/(amatrix(3,3)*(z(NPLY+1)-z(1)));
nineprop(4)=-amatrix(2,1)/amatrix(1,1);
nineprop(5)=-amatrix(1,2)/amatrix(2,2);
nineprop(6)=amatrix(1,3)/amatrix(3,3);
nineprop(7)=amatrix(2,3)/amatrix(3,3);
nineprop(8)=amatrix(3,1)/amatrix(1,1);
nineprop(9)=amatrix(3,2)/amatrix(2,2);

XX = array2table(nineprop,'VariableNames',{'Ex' 'Ey' 'Gxy' 'vxy'
'vyx' 'nxy_x' 'nxy_y' 'nx_xy' 'ny_xy'})
nineprop(3)
nineprop(1)/2/(1+nineprop(4))
%Problem 4
for (iii=1:NPLY)
    ALPHA_XY(iii,:)=R*Tsiginv(:, :, iii)*Rinv*ALPHA12(iii, :);
    BETA_XY(iii,:)=R*Tsiginv(:, :, iii)*Rinv*BETA12(iii, :);
end
thermprops(:,1)=sevenprop(:,1);
thermprops(1:NPLY,2:4) = ALPHA_XY;
thermprops(1:NPLY,5:7) = ALPHA12;
thermprops(:,8)=sevenprop(:,2);

disp('Problem 4')
ThermProps = array2table(thermprops,'VariableNames',{'PLY' 'alphax'
'alphay' 'alphaxy' 'alpha1' 'alpha2' 'alpha12' 'Angle'})

hygroprops(:,1)=thermprops(:,1);
hygroprops(1:NPLY,2:4) = BETA_XY;
hygroprops(1:NPLY,5:7) = BETA12;
hygroprops(:,8)=sevenprop(:,2);

```

```

HygroProps = array2table(hygroprops,'VariableNames',{'PLY' 'betax'
'betay' 'betaxy' 'beta1' 'beta2' 'beta12' 'Angle'})

disp('Problem 5')
delta_t=C(1);
delta_c=C(2);
mechNM=C(3:8);
mechNM=mechNM';

N_T=0; %Initialize therm/hyrgo force & moment resultants
N_H=0;
M_T=0;
M_H=0;
for(jjj=1:NPLY) %Calculate therm/hyrgo force & moment resultants
    N_T=N_T+(Qbar(:, :, jjj)*ALPHA_XY(jjj, :)' .* delta_t * (z(jjj+1)-
z(jjj)));
    N_H=N_H+(Qbar(:, :, jjj)*BETA_XY(jjj, :)' .*delta_c*(z(jjj+1)-
z(jjj)));

M_T=M_T+0.5*(Qbar(:, :, jjj)*ALPHA_XY(jjj, :)' .*delta_t*((z(jjj+1))^2-
(z(jjj))^2));

M_H=M_H+0.5*(Qbar(:, :, jjj)*BETA_XY(jjj, :)' .*delta_c*((z(jjj+1))^2-
(z(jjj))^2));
end

NBAR=mechNM(1:3)+N_T+N_H;
MBAR=mechNM(4:6)+M_T+M_H;
resultants(1:3)=NBAR;
resultants(4:6)=MBAR;
disp('Loading Summary: (N units are N/m, M units are N*m/m)')
YY = array2table(resultants,'VariableNames',{'Nx' 'Ny' 'Nxy' 'Mx'
'My' 'Mxy'})

disp('Problem 6')
NM_BAR(1:3)=NBAR;
NM_BAR(4:6)=MBAR;
NM_BAR=NM_BAR';
eps0kap_matrix = inv(ABDmatrix)*NM_BAR;

disp('Midplane Ply Strains (m/m) & Curvatures (1/m)')
Z = array2table(eps0kap_matrix,'VariableNames',{'eps0x' 'eps0y'
'eps0xy' 'kx' 'ky' 'kxy'})

for(l11=1:NPLY)

plystrainXY(l11, :)=eps0kap_matrix(1:3)+((z(l11+1)+z(l11))/2)*eps0kap
_matrix(4:6);
    plystrain12(l11, :)=R*Tsig(:, :, l11)*Rinv*plystrainXY(l11, :);

```

```

    plystressXY(l11,:) = Qbar(:,:,l11)*(plystrainXY(l11,:)'-
ALPHA_XY(l11,:) '*delta_t - BETA_XY(l11,:) '*delta_c);
    plystress12(l11,:) = Tsig(:,:,l11)*plystressXY(l11,:)';
end

plystrain(:,1) = sevenprop(:,1);
plystrain(:,2:4) = plystrainXY;
plystrain(:,5:7) = plystrain12;
plystrain(:,8) = sevenprop(:,2);

plystress(:,1) = sevenprop(:,1);
plystress(:,2:4) = plystressXY;
plystress(:,5:7) = plystress12;
plystress(:,8) = sevenprop(:,2);

disp('Stresses due to Residual & Mechanical Loads (Pa)')
ZZ = array2table(plystress, 'VariableNames', {'Ply' 'sigX' 'sigY'
'tauXY' 'sig1' 'sig2' 'tau12' 'Angle'})
disp('Sum of Residual Strains (m/m)')
ZZZ = array2table(plystrain, 'VariableNames', {'Ply' 'epsX' 'epsY'
'gamXY' 'eps1' 'eps2' 'gam12' 'Angle'})

%%%%%%%%%%%%%%%%%%%%%%%%%%%%%%%%%%%%%%%%%%%%%%%%%%%%%%%%%%%%%%%%%%%%%%%% Homework 4 %%%%%%%%%%%%%%%%%%%%%%%%%%%%%%%%%%%%%%%%%%%%%%%%%%%%%%%%%%%%%%%%%%%%%%%%%
%Tsai Wu

%For E-Glass:
F1t = 367e6;
F2t = 367e6;
F1c = 549e6;
F2c = 549e6;
F6 = 97.1e6;

Farray = [F1t, F2t, F1c, F2c, F6]

f1 = (1/F1t - 1/F1c);
f2 = (1/F2t - 1/F2c);
f11 = 1/(F1t*F1c);
f22 = 1/(F2t*F2c);
f12 = (-1/2)*sqrt(f11*f22);
f66 = 1/((F6)^2);

for (qq=1:NPLY)
    TWnumber(qq) = f1*plystress(qq,5) + f2*plystress(qq,6) + f11*(plystress(qq
,5))^2 + f22*(plystress(qq,6))^2 + ...
    2*f12*plystress(qq,5)*plystress(qq,6) + f66*plystress(qq,7)^2;
    format short g
    TWarray(qq,:) = [plystress(qq,1), TWnumber(qq), plystress(qq,5),
plystress(qq,6), plystress(qq,7), plystress(qq,8)];
end

```

```
ZZ = array2table(TWarray, 'VariableNames', {'Ply' 'TW' 'sig1' 'sig2'  
'tau12' 'Angle'})  
  
ZZ = array2table(Farray, 'VariableNames', {'F1t' 'F2t' 'F1c', 'F2c',  
'F6'})
```

## Appendix C

### Non-Technical Abstract

New forms of renewable energy are gaining popularity as the global trend towards sustainability grows. One such form is called hydrokinetic energy, which involves harvesting energy from natural water currents. Hydrokinetic turbines are similar to wind turbines, except water currents cause the blades to spin as opposed to air currents. Unfortunately, high maintenance costs stifle the growth hydrokinetic energy because the turbine blades breakdown relatively often. If seriously damaged, the underwater turbine must be retrieved in order to make repairs and inspect for other damage. Therefore, improving the service life of the hydrokinetic turbine blades will greatly benefit the up-and-coming energy technology.

Hydrokinetic turbine blades are made out of a fiber-reinforced polymer composite material. This material is sturdy because of the strong and stiff glass fibers, which serve as the backbone of the material. The surrounding epoxy-based polymer holds the fibers together and does not corrode (like metal structures) in the presence of seawater. However, the polymer does absorb water, which causes structural degradation through physical and chemical means. Thus, testing the material with and without absorbed water by applying stress can aid in quantifying these degradations to gauge the expected lifetime of the blades.

These tests were performed in this study for two different composite material systems and several trends were noted. The two material systems contained the same polymer and the same type of glass fiber, but the fibers were bundled using two different textile methods. The stitched material system tended to have superior properties than the woven material system only in long-duration tests at lower stress levels. Similarly, the stitched composite showed less damage in long-duration tests compared to the woven composite. Image scans and microscope pictures of

damaged and failed samples showed a difference in the damage mechanisms within the two composite material systems. While the stitched composite occasionally contained more cracks than the woven composite, the stitched composite still out-performed the woven roving samples in terms of strength retention. Finally, the stitched composite partially saturated with water tended to encounter failure and similar levels of damage ten times sooner than stitched samples with no absorbed water.